DISCOVERY AND CHARACTERIZATION OF A NOVEL HEME-IRON ACQUISITION PATHWAY FROM ENTEROHEMORRHAGIC *E. coli*

by

JOSEPH LAMATTINA

(Under the Direction of William N. Lanzilotta)

Abstract

Iron is an essential nutrient bacteria must acquire to survive within their niche, which can be a major barrier during colonization and pathogenesis. Therefore, pathogenic microorganisms have developed pathways to utilize heme as an iron source. Heme oxygenases are the canonical enzymes that degrade heme and require diatomic oxygen in the enzymatic mechanism. However, the hemolytic enteric bacteria *Escherichia coli* O157:H7 and *Vibrio cholerae* do not contain an equivalent enzyme and are subjected to low oxygen tensions during pathogenesis. In this work, we establish the function of ChuW and ChuY from *E. coli* O157:H7. Our data indicate ChuW is a radical S-adenosylmethionine methyltransferase that degrades heme to release the heme-iron and produce the novel tetrapyrrole ”anaerobilin”. ChuY is the downstream enzyme to ChuW that can reduce anaerobilin using NADPH as a cosubstrate. Thus, ChuW and ChuY represent a novel oxygen-independent heme degradation pathway.

DISCOVERY AND CHARACTERIZATION OF A NOVEL HEME-IRON ACQUISITION PATHWAY FROM ENTEROHEMORRHAGIC *E. coli*

by

JOSEPH WILLIAM LAMATTINA

B.S., University of Central Florida, 2010

A Dissertation Submitted to the Graduate Faculty

of The University of Georgia in Partial Fulfillment

of the

Requirements for the Degree

DOCTOR OF PHILOSOPHY

ATHENS, GEORGIA

2016

Joseph LaMattina

DISCOVERY AND CHARACTERIZATION OF A NOVEL HEME-IRON ACQUISITION PATHWAY FROM ENTEROHEMORRHAGIC *E. coli*

by

JOSEPH LAMATTINA

(Under the Direction of William N. Lanzilotta)

Approved:

Major Professor: William Lanzilotta

Committee: Harry Dailey
Michael Johnson
Zac Wood

Electronic Version Approved:

Suzanne Barbour
Dean of the Graduate School
The University of Georgia
August 2016

Dedication

To my best friend and loving wife, Mariah, for the love and support needed to pursue my dream. For staying with me during our time here, even when it was not easy. You are the reason this was possible.

To my parents for encouraging me to work hard and never give up.

Acknowledgements

"Thirst was made for water.

Inquiry for truth."

- C.S. Lewis

There are many people that helped with this work, whether it was ideas contributed or experiments done to further this project. I would like to thank my advisor, Bill Lanzilotta, for keeping me grounded and allowing me to investigate this question while providing insight when needed. I would like to thank each of my committee members, Harry Dailey, Michael Johnson, and Zac Wood, for their guidance not only with the project, but with future aspirations. Furthermore, I would like to thank Zac for allowing me open access to the equipment in his lab, as well as his lab personnel for their technical advice. Harry Dailey and his lab have also provided valuable insight and have allowed me to use chemicals and substrates when needed. Tammy Dailey has also dedicated significant time to proofing this document and has provided helpful tips for improving my writing. Mike Johnson and his lab (Brian and Bo) were very helpful with EPR spectra interpretation and instrument set up. Thank you to the Adams lab and Farris for allowing me to use many of their instruments and for providing their insight. I would like to thank David Nix and Nick Keul for their collaboration with mass spectrometry and analytical ultracentrifugation. I would like to thank the undergraduates that helped with this project, including Addison Wright, Anudeep Reedy, Kate Uy, and Michael DelRossi. Thank you to Jon Demick for training me during my first year as a graduate student. A special thanks to Kristen Miller and the Biology lab managers for putting up with me for so long. Finally, I would like to thank the faculty and

staff of the Biochemistry and Molecular Biology department for guiding me through my graduate career.

My friends and family have been instrumental in keeping me sane during this process. I would like to thank my long time friends Bryan, Daryl, Eric, Chris, and Jared for their committed friendship. There is no distance that can separate us and I love that we always pick up right where we left off when we get together. While in Athens, the Georgia ultimate program has been my escape from lab. Thank you to all the people I have had the pleasure of getting to know and compete with. Playing Ultimate with all of you really helped reduce the pressures of graduate school. Lastly, I would like to thank my wife, Mariah, and my family for their continued support while I pursue a career in science.

You all are the reason for my success.

Contents

List of Figures

List of Tables

List of Abbreviations

5’-dA - 5’-deoxyadenosine

aSDR - atypical short chain dehydrogenase

BLAST - basic local alignment search tool

BVR - biliverdin reductase

CO - carbon monoxide

CPO - coproporphyrinogen oxidase

CTD - carboxy terminal domain

DFT - density functional theory

DAB - deuteroanaerobilin

DAR - deuteroanaerorubin

DMSO - dimethylsulfoxide

ENDOR - electron nuclear double resonance

EPR - electron paramagnetic resonance

FAD - flavin adenine dinucleotide

FMN - flavin mononucleotide

GRE - glycyl radical enzyme

GRE-AE - glycyl radical activating enzyme

His - histidine

HO - heme oxygenase

HPLC - high pressure liquid chromatography

HS - high spin

KO - knockout

LS - low spin

mTrp - 2-methyltryptophan

NAD(P)H - nicotinamide adenenine dinucleotide (phosphate)

NMR - nuclear magnetic resonance

NSI-MS - nanospray ionization mass spectrometry

NO - nitric oxide

PLP - pyridoxal 5'-phosphate

PPIX - protoporphyrin IX

RSMT - radical SAM methyltransferase

rR - resonance Raman

SAH - S-adenosylhomocysteine

SAM - S-adenosyl-L-methionine

SFLD - structure function linkage database

Trp - tryptophan

UV - ultraviolet

CHAPTER 1

REVIEW OF THE LITERATURE

Iron is an essential micronutrient that all kingdoms of life must acquire to survive. However, as the earth has aged the bioavailability of iron has decreased, which is inversely proportional to the emergence of oxygen in the atmosphere[1]. The Great Oxygenation Event presumably caused an oxidation switch of iron from the reactive ferrous state, (Fe^{2+}), to the poorly soluble ferric state, (Fe^{3+}). Iron is acquired through diet for mammals, while microorganisms scavenge it from their surrounding environment. For the virulence of bacterial pathogens, iron must be acquired from their hosts and is well-studied in multiple organisms[2–4]. Thus, the need for this naturally abundant metal became a major barrier for bacteria to survive within their niche. In response, biology has evolved mechanisms to acquire iron and utilize its redox potential while limiting its cytotoxicity.

Heme can be used as an iron source and knockouts of the heme uptake pathway in enteric pathogens result in the inability for the organism to compete in a mouse model[5,6]. Despite extensive studies to characterize the pathways to get heme into the cytoplasm (Figure 1.1), the processing/degradation of the small molecule once inside is not understood. The canonical pathway to degrade heme in some prokaryotes is by the enzyme known as heme oxygenase (HO), but not all organisms appear to encode an identifiable homologue. HOs also require two equivalents of diatomic oxygen to achieve one catalytic cycle, but not all bacteria grow in the presence of oxygen. In fact, the hemolytic enteric pathogens *Escherichia coli* O157:H7 and *Vibrio cholerae* are known to colonize within the

small and large intestines where the composition of the microbiota are largely anaerobic[7].

A heme uptake/utilization operon is present in the enteric pathogens described above. Although the proteins associated with this operon that are involved in bringing heme into the cytoplasm have been characterized, the consensus for the function of the three genes *chuWXY(Z)* were not established prior to the work described herein. One model for the degradation of heme in *E. coli* is by the heme-binding protein ChuS[8], but these observations are not fully accepted in the field[9,10]. ChuW was annotated as a radical SAM enzyme, and our hypothesis was that this enzyme was involved in the anaerobic degradation of heme. We predicted ChuY acted similarly to biliverdin reductase and could reduce the tetrapyrrole catabolite of the reaction catalyzed by ChuW. This system would provide the first evidence for the existence of an anaerobic heme degradation pathway in biology. The following sections will review the background of heme acquisition and degradation, before further discussing the complexity of this heme utilization operon.

1.1 Bacterial Heme Acquisition and Degradation

Although mammals transport and store iron with the use of transferrin and ferritins, the most abundant source of iron is bound within a prophyrin ring known as Fe-protoporphyrin IX (Fe-PPIX). Formerly, the Fe^{2+} reduced form of Fe-PPIX is referred to as heme and the Fe^{3+} oxidized form as hemin. Due to the toxicity of Fe-PPIX at high levels, the mammalian intracellular heme pool is tightly regulated by heme biosynthesis and catabolism[11]. Mammalian pathogens have developed pathways to utilize heme as an iron source since it can be supplied by circulating red blood cells. This section will briefly discuss the mechanisms for heme acquisition with the primary focus on heme degradation within the bacteria domain.

Exploited Heme Sources

Nearly every known mechanism for heme transport and storage can be exploited for bacterial use. Some sources include hemoglobin, hemoglobin-haptoglobin, and even the extremely high heme affinity protein, hemopexin. Mechanisms for acquisition have been characterized in both gram-negative and gram-positive bacteria and it would appear as if these prokaryotes developed mechanisms to acquire heme based on the organism's preferential localization of infection[12].

Hemoglobin, migrating from intravascular hemolysis of red blood cells, is the most abundant source of heme in human serum and can exist in three forms; deoxyHb, which coordinates heme with no sixth ligand; the oxyHb that coordinates diatomic oxygen as the sixth ligand; and metHb, or methemoglobin, which binds 5-coordinate hemin. Hemoglobin can be proteolytically degraded to release heme, as observed in *Porphyromonas gingivalis* with the lysine-specific cysteine protease Kgp[13] and by *E. coli* EB1 with Hbp[14]. These proteases can bind directly to the bacterial heme receptors, such as ChuA from *E. coli* and HmbR from *Neisseria meningitidis* to allow for heme uptake. Table 1.1 shows a representative subset of heme receptors and their target heme sources. Although it is the largest heme source, hemoglobin is rarely found in serum without its partnering protein haptoglobin, a heterotetrameric glycoprotein with sub picomolar affinity for Hb, and is present at a concentration of 1.2 mg mL^{-1} [15]. However, a receptor for this complex was described in *N. meningitidis*[16].

One of the most unexpected sources of heme is from hemopexin, which is present in serum at micromolar concentrations. This glycoprotein has an unusually high affinity for heme with an association constant of 10^{13} M^{-1} [17], and is one of the highest heme-affinity proteins known. The ability for *Hemophilus influenzae* to use hemopexin as an iron source was shown in 1991 by Hanson *et al.*[18]. The gene cluster was identified[19] following studies

showing the ability for a *H. influenzae* HxuA null mutant to grow on medium containing heme-hemopexin only when exogenous HxuA was present. Unexpectedly, HxuA bound hemopexin causing the release of heme to the outermembrane receptor HxuC before transporting it into the cell[20].

Another source of heme is human serum albumin (HSA), which makes up 60% of the total protein content in serum at 40 mg mL^{-1} [21]. With an affinity for heme 1000X greater than that of bovine serum albumin (BSA), HSA can bind heme at a heme to protein ratio of 10:1. Despite the ability to bind heme, HSA is one of the only heme sources not known to be targeted by bacteria.

The heme sources described are manipulated to release the heme to an outer-membrane receptor allowing for the active transport into the cytoplasm. Although these uptake pathways are well-characterized, the fate of heme once translocated into the cytoplasm is unclear.

Heme Degradation

Heme oxygenases (HOs) are the enzymes responsible for the degradation of heme to form biliverdin IX, a six electron process that requires oxygen to cleave the tetrapyrrole in order to release iron. In eukaryotes, this process occurs during the destruction of red blood cells, in which heme is sent to the liver, degraded to biliverdin, and reduced to bilirubin before being glucoronidated and eventually excreted through the intestines[22–24]. Bacterial pathogens also have similar enzymes that utilize oxygen to degrade heme. The structure, mechanism, and regulation of these heme degrading enzymes is discussed below.

Human Heme Oxygenase-1

It has been known that eukaryotic cells can convert heme to bilirubin in nearly stoichiometric quantities since the 1950's. However, the enzyme(s) responsible for this reaction was not

characterized until 1968[23]. This heme oxygenase was first characterized from rat liver microsomes[25], which converted heme to biliverdin IXα in the presence of both NADPH and diatomic oxygen. The enzyme required a 6:3:1 molar ratio for NADPH, diatomic oxygen, and heme to produce one biliverdin molecule with a specific activity of 0.1 μmoles min^{-1} mg^{-1} enzyme. However, the activity was dependent on pH and the specific buffer used. Nearly ten years after this initial characterization of the microsomal heme oxygenase, a study showed using Co-protoporphyrin IX as a substrate did not result in turnover of the enzyme[26]. Considering that the dimethylester of Co-heme and cobaltous myoglobin can react with molecular oxygen, the authors postulated the lack of turnover was due to a prerequisite for the enzyme to reduce the metal for the mechanism, which would not occur with the NADPH-cytochrome C reductase system based on the reduction potential of Co^{3+}-PPIX to Co^{2+}-PPIX[26].

The heme-iron binding site was initially characterized by mutagenesis studies and spectroscopic analyses due to the lack of any structural data of heme oxygenases[27,28]. Electron paramagnetic resonance (EPR) and resonance Raman (rR) spectroscopies determined the axial ligand as a neutral histidine[29]. Mutation of the His25 residue resulted in the change of the spectroscopic signals, and thus identified the specific histidine responsible for coordination of the heme-iron[30]. When in the oxidized state, the ferric iron coordinates a distal water molecule that can be base-titrated to a hydroxide as observed by UV-visible absorption spectroscopy[27]. Wilks *et al.* determined that a second conserved histidine residue within the active site effects heme binding while facilitating catalysis despite not being essential for turnover[31]. Using His132 mutants, rR spectroscopy supported the bound heme to be 5-coordinate. Since the Fe-N_{His} stretching was still present and therefore must correspond to the His25 axial ligand, it was proposed that His132 was involved in stabilization of the axial water to the iron. This was later challenged by Matera *et al.* by similar methods, in which acid-base titrations with identical mutants

resulted in a pK_α identical to wild-type enzyme[32]. These results indicated no essential role in distal water coordination to the heme-iron[32].

Corynebacterium diptheriae heme oxygenase, HmuO

Although human heme oxygenase isoform 1 (hHO-1) was studied nearly 30 years prior to the 1990's, the mechanism by which prokaryotes could use heme as an iron source was not known. The HO from *Corynebacterium diptheriae*, HmuO, was the first of the bacterial enzymes reported and had only a 33% sequence identity to hHO-1. HmuO is an essential cytoplasmic protein for heme-iron utilization, as supported by complementation studies of chemically derived mutants of *C. diptheriae* and *C. ulcerans*[33]. *HmuO* is regulated by DtxR, and allows expression of the enzyme during iron repletion[34]. Although HmuO converts heme to the α isomer of biliverdin IX, spectroscopic evidence of the heme environment suggested significant differences in the active site compared to hHO-1[35]. The proximal His20 ligand, though important for catalysis, was not essential for heme binding, nor was it necessary for proper heme seating in the active site[35,36].

The thermodynamic dissociation constant for O_2 by heme-bound HmuO was observed to be 22 μM[1 37]. Similar experiments resulted in a reduced affinity for carbon monoxide (CO), and suggested a preference for an angled geometry for the ligand bound to the heme-iron, as this would not occur with the C-O triple bond[37]. The structure of CO bound rat HO-1 and *N. meningitidis* HemO confirmed these results by comparing the structural overlay of water bound HO[38]. Due to the linearity and inflexibility of the CO bond, the distal helix and proximal histidine are forced away from each other on a lateral plane, causing significant changes to the active site and the reduced affinity observed for the gas. The structure of the ferrous oxy form of HmuO also supported these data, which showed steric interactions with two glycine residues on the distal helix. Mutational analyses determined the importance of the glycine residues for the mechanism of hHO-1, in which mutation of

either glycine resulted in either reduced or abolished activity[39].

Other canonical heme oxygenases that convert heme to α-biliverdin IX

Two other known heme oxygenases are HemO from *Neisseria meningitidis* and BphO from *Pseudomonas aeruginosa*. These HOs have similar activity to hHO-1 and HmuO, but differences lie within their physiological roles. HemO, like HmuO, is important for pathogenesis and is required by the organism for survival during iron duress. Despite the similarities of HemO to other previously characterized HOs, this is the least studied of the α-biliverdin IX producing HOs. However, the structure was solved in complex with heme to a resolution of 1.5 Å. The structures of CO-bound and NO-bound enzyme helped uncover the hydrogen bonding network needed for the proton shuttling to the peroxy intermediate, as well as the gas binding specificity.

In contrast, BphO is a constitutively expressed protein from *P. aeruginosa* and follows the canonical HO mechanism to form biliverdin IXα. This heme oxygenase is not involved in pathogenesis, but rather, the verdin produced is the precursor for the chromophore used by the phytochrome *Pa*BphP, a light-regulated sensor kinase in a two-component signaling system[40]. *Pa*BphP can preferentially use biliverdin IXα to form a photoconvertable holo-phytochrome and upon red light (650 nm) absorption causes the 15Z/15E isomerization at the 15/16C double bond.

Enzymatic mechanism for heme oxidation

Heme oxygenation requires six electrons and three equivalents of diatomic oxygen to convert heme to biliverdin (Figure 1.3). The initial catalytic steps for heme oxygenases are initially similar to P450 enzyme reactions. The first reduction event prompted by the NADPH-dependent cytochrome P450 reductase causes the reduction of ferric to ferrous iron, allowing for diatomic oxygen to bind to the heme-iron. The second reduction allows for

the formation of the active oxygen species to cause hydroxylation at the α-meso position to form α-mesohydroxyheme[41]. This transition causes the enzyme to tighten the binding pocket, bringing the Gly139 carbonyl in hHO1 closer to the distal water ligand[37,42]. The water molecule normally bound to the iron is displaced by O_2. This displacement is due to two conserved distal glycine residues by directing the oxygen toward the α-meso carbon. Continuous wave Q-band proton ENDOR based examination of cryoreduced HO was used to characterize the environment for the oxy-heme intermediate compared to hemoglobin[43]. In this study, hemoglobin provided a hydrogen bond that stabilized the peroxo form when reduced, but cryoreduction of HO caused conversion to a hydroperoxy species even when at temperatures as low as 4K. When using ^2H_2O (D_2O) the ENDOR signal for the proton was diminished[43]. This indicated the ability for proton shuttling to the ferrous-oxy intermediate without the need for active site rearrangement.

The major difference between P450s and HOs is the target for hydroxylation from hydroperoxy intermediate. In P450s the hydroperoxy intermediate hydroxylates the substrate, whereas HOs facilitate hydroxylation of the heme cofactor. HOs also require a second electron to release the second oxygen as water and oxidize the heme-iron, rather than retaining the oxygen and transiently forming compound I, as in the P450s. This was observed when annealing the cryoreduced HO sample to 200 K where the EPR signal for a high-spin ferric hydroxyheme was predominant[43].

The intermediate following the formation of α-mesohydroxyheme is verdoheme. Although this catalytic step is oxygen-dependent, it is still unclear whether the conversion requires an exogenous electron. This is primarily due to the fact the kinetic rate of ferric α-mesohydroxyheme conversion to ferric-verdoheme was faster than the reduction of ferric α-mesohydroxyheme to the ferrous species[44]. The crystal structure of the verdoheme-HO-1 complex was refined to 2.2 Å and resulted in a five coordinate iron absent of the distal water[45], which was inconsistent with previous spectroscopic studies[46]. Either diatomic

oxygen or a peroxide can bind at the ferrous iron of verdoheme[47], but the activity with peroxide is 50x faster than that with oxygen and can be inhibited by the competitive binding of small molecules like azide or carbon monoxide. Depending on the use of oxygen or peroxide, the progression to biliverdin will result via two different intermediates that have not been characterized. When oxygen is used in the mechanism, a subsequent 3 electron reduction is needed for the conversion to biliverdin, thus requiring a total of six electrons as oxygen is the assumed physiological substrate. Upon reduction of the heme-iron to the ferrous state, the products are released from the active site to allow for the binding of a new heme molecule.

Pseudomonas aeruginosa heme oxygenase

Shortly after the initial characterization of *N. meningitdis* HemO and *C. diptheriae* HmuO, Ratliff and co-workers showed evidence for an iron regulated heme oxygenase from *P. aeruginosa*[48]. This enzyme produced different isoforms of biliverdin IX and was differentially regulated from BphO. Formerly known as PigA, *Pa*HO converts heme to the β and δ isomers of biliverdin IX at a 30:70 ratio[48]. The crystal structure of heme-bound *P. aeruginosa* HO was solved by molecular replacement and refined to 1.6 Å[49]. Structural overlays with *N. meningitidis* HO revealed that heme was rotated nearly 100° in the *P. aeruginosa* HO, putting the δ-meso carbon in the same position as the α-meso carbon in the *Neisseria* ortholog. This was the first example of two distinct heme oxygenases within one organism that fulfill different physiological needs.

Despite the differences in heme seating within the active site, similar themes are present in the *P. aeruginosa* HO, including the overall α helical fold. Additionally, the steric strain created by the distal helix is present that directs the O-O bond in the direction of the δ-meso carbon preventing hydroxylation at the other positions[49]. Considering the similarity in environments between the δ-meso side of heme and the β-meso side, it is

likely the heme will be positioned as to have the δ position exposed to hydroxylation, or if flipped 180° along the α-γ axis, will have the β position exposed. This alternate heme seating was confirmed by NMR in hHO-1[50]. Another simililarity is the extensive hydrogen bonding network with solvent in the active site promoting proton delivery. Water molecules positioned within 4 Å from the distal water suggested similar proton shuttling in the active site[49].

Staphylococcus aureus IsdG and IsdI

Although alternative biliverdin IX products were characterized in some microorganisms, the heme oxygenases described reflected the HO characterized from eukaryotes in structure. IsdG and IsdI from *Staphylococcus aureus* were the first atypical heme degrading enzymes that differed in structure and mechanism[51]. These enzymes are differentially regulated based on heme and iron levels with the the cell[52]. The reaction catalyzed by IsdG and IsdI results in the opening of the porphyrin ring at either the β or δ positions with an additional oxidation occuring at the methine bridging carbon across from the ring opening and the formation of the unique verdin termed "staphylobilin"[53] (Figure 1.2). Unlike other HOs, carbon monoxide (CO) is not a byproduct of IsdG, but rather formaldehyde is released during the reaction[54]. This alternative byproduct is presumed to play a role in prevention of bactericidal effects of CO[55].

The structures are similar to the monooxygenase ActVA with a ferredoxin fold that forms a β-barrel at the dimeric interface[51]. The structure of holo-IsdG gave structural evidence for heme ruffling, a porphyrin ring distortion not observed in previously described heme oxygenases[56]. Spectroscopic and density functional theory (DFT) analyses revealed the importance of an active-site arginine that directs the hydroperoxo-intermediate to the β-meso carbon by direct hydrogen bonding. Thus, these analyses supported the site-specific hydroxylation at the β-methine bridge[57].

Mycobacterium tuberculosis MhuD

The most recent non-canonical HO characterized, MhuD, was isolated from *Mycobacterium tuberculosis*[58]. The crystal structure of MhuD supported the predicted homology to IsdG and IsdI, however, the structure revealed a unique di-heme conformation of the enzyme that was inactive[58]. When a single heme molecule is bound, MhuD could degrade heme with the supply of oxygen and an electron source[59]. The products of the reaction, mycobilin a and b, are distinguished by the retention of the α-meso carbon upon ring opening as an aldehyde on either C4 or C6 of the porphyrin ring. This retention was proposed to prevent the transition to dormancy for *M. tuberculosis*[60], which is induced by sensing the increase of host carbon monoxide[61]. Similar to the Isd enzymes, MhuD oxidizes another carbon, which occurs at the adjacent methine bridging carbon proximal to the aldehyde. A follow-up study from Graves *et al.* showed electronic and structural evidence for the regioselectivity of MhuD[62]. This analysis also supported the unique porphyrin distortion, albeit to a lesser extent than IsdG.

HemS, HemS-like homologues, and non enzymatic coupled oxidation

HemS was originally proposed to act as a heme degrader based on the observation that genetic knockouts of *hemS* in *Yersinia enterocolitica* resulted in the inability of the organism to grow on heme as the sole iron source[63]. However, further characterization of HemS was never performed. The genetic knockouts of other cytoplasmic heme transporters result in similar phenotypes[9]. HutS from *Pseudomonas aeruginosa*[*] was first identified as an intracellular heme trafficking protein responsible for transporting extracellularly acquired heme to the δ-regioselective HO[64]. It was later shown that heme binding to *Pa* HutS drives its interaction with the HO[65], and that, ultimately, *Pa* HutS acts as a ”controllable valve”

[*] *P. aeruginosa* HutS is equivalent to *P. aeruginosa* PhuS.

to regulate heme flux to *P. aeruginosa* HO[66]. In contrast, others reported *P. aeruginosa* HutS acts as a heme oxygenase. However, they demonstrated activity only by UV-visible spectroscopy and CO detection[67]. It should be noted that non-enzymatic coupled oxidation can occur when electrons are present with molecular oxygen bound to ferrous heme[10]. It is for this reason catalase is often used in the HO assay to prevent non-enzymatic heme degradation. To this end, identifying bonafide HOs can be difficult *in vitro* due to a false positive activity. In fact, Wilks *et al.* suggested the initial mechanism for heme oxygenation is likely facile due to the fact many heme proteins can undergo non-enzymatic conversion of heme to verdoheme[10].

Other homologues of HutS have been identified in *Shigella dysenteriae*[†] and *E. coli*[‡]. Due to the differences in genetic background and lack of a canonical HO, it is difficult to determine the functional role of these genes. *E. coli* HutS was proposed to act as a heme degrader based on spectral observations upon addition of ascorbic acid[68]. However, catalase was never explicitly used in the assay and later reports showed catalase severely retarded the HO activity by *Ec* HutS[67]. A follow up report suggested the loss of hematinic acid and a tripyrrole, but the HPLC traces of activity suggested non-specific cleavage of the porphyrin ring[69]. Additionally, increasing catalase inhibited *Ec* HutS when using H_2O_2 in the reaction, which is indicative of non-enzymatic coupled oxidation of heme to verdoheme[10]. Taken together, this suggests HutS is not likely to be a genuine HO, thus leaving unanswered the question of how *E. coli* and similar organisms degrade heme.

[†] *S. dysenteriae* HutS is equivalent to *S. dysenteriae* ShuS.
[‡] *E. coli* HutS is equivalent to *E. coli* ChuS.

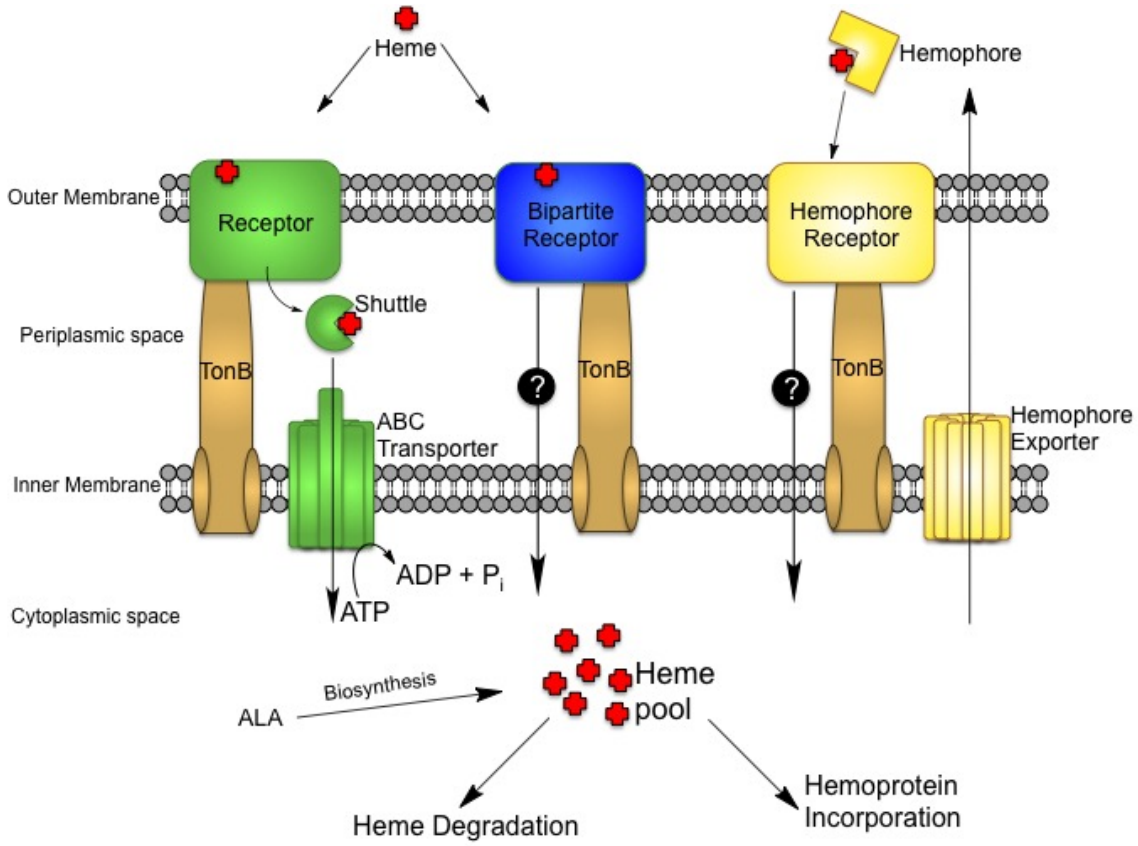

Figure 1.1: Heme uptake pathways characterized in gram-negative bacteria.

Table 1.1: Bacterial receptors for heme acquisition

Microorganism	Protein	Target	Reference(s)
C. diptheriae	HtaA	Hm and Hb	[70]
E. coli	ChuA	Hm and Hb	[71]
	Hma	Hm	[72]
H. influenzae	HgpA/B/C	Hb/Hp	[73, 74]
	HxuA	Hm and Hpx	[75]
N. meningitidis	HpuAB	Hb/Hp	[76, 16]
	HmbR	Hb	[77]
P. gingivalis	HmuR	Hm and Hb	[78]
	HemR	Unknown	[79]
P. aeruginosa	PhuR	Hm and Hb	[80, 81]
	HasR	Hm and Hb	[80, 81]
S. dysenteriae	ShuA	Hm	[82]
S. marcescens	HasR	Hm and Hb	[83]
V. cholerae	HutA	Hm	[84]
	HasR		[85]
	HemR		[85]
Y. pestis	HmuR	Hm and Hb	[86]
Y. enterocolitica	HemR	Hm	[87]

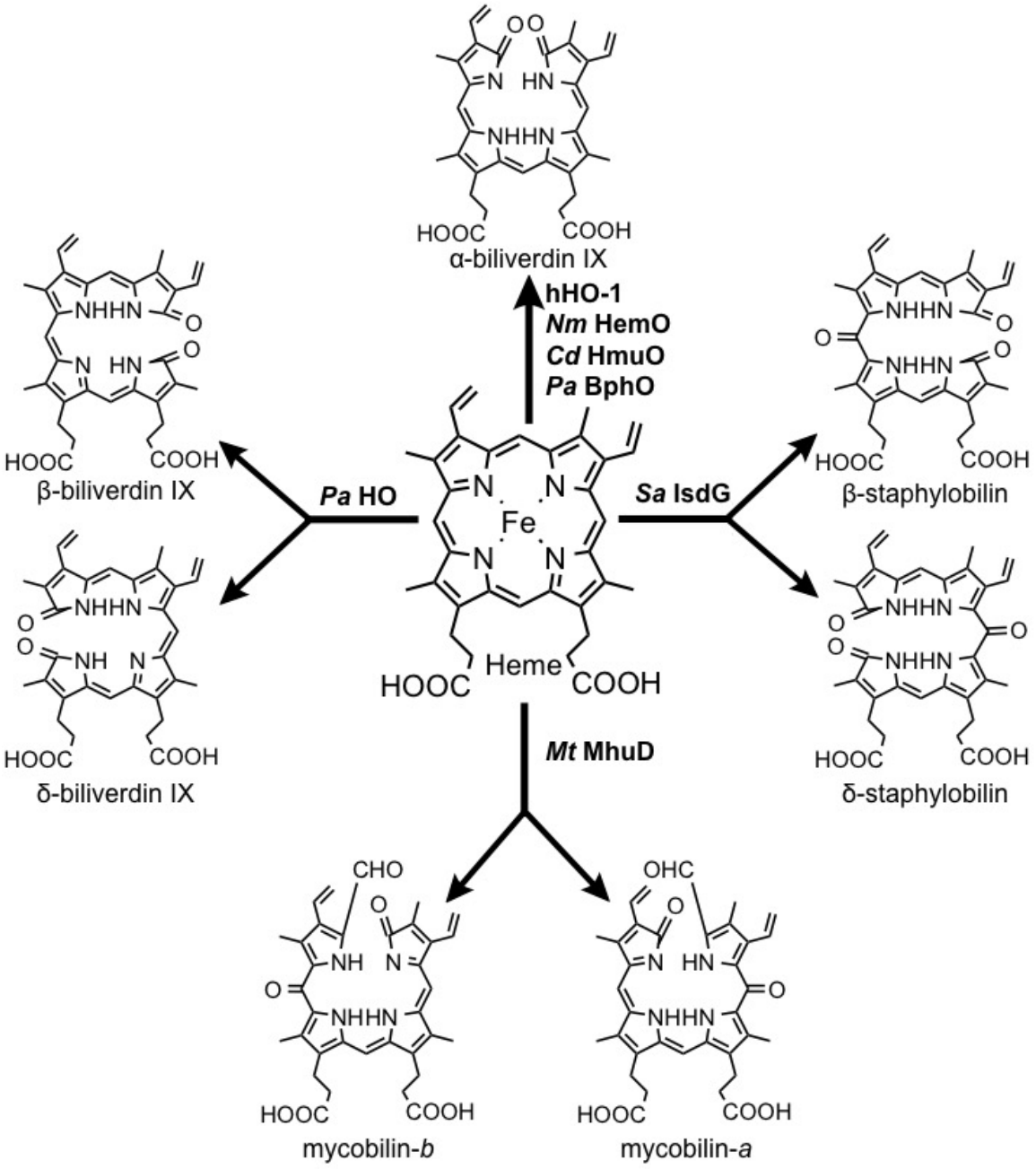

Figure 1.2: Schematic representation of the four types of oxygen-dependent heme degrading enzymes characterized.

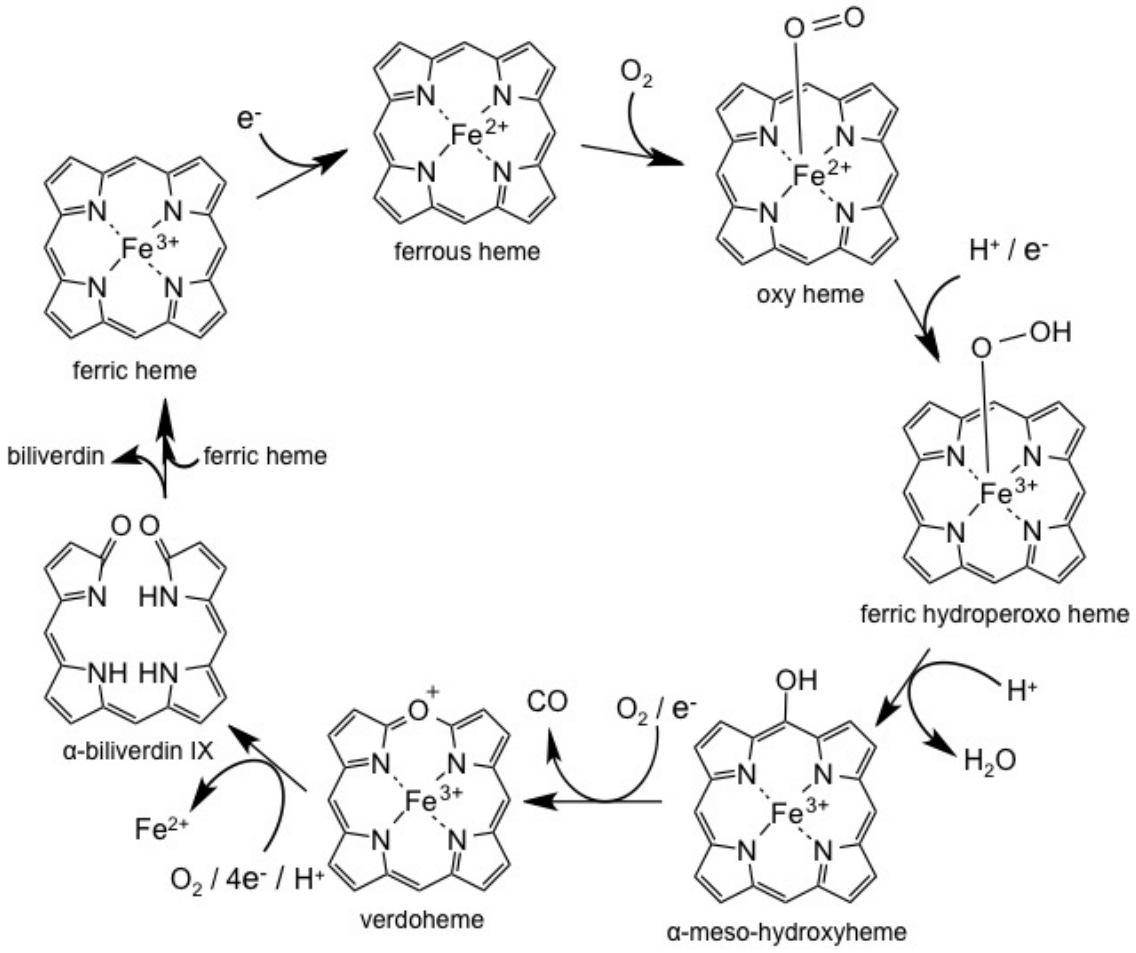

Figure 1.3: Proposed mechanism of heme oxygenase adapted from Unno, M *et al.*[37]

1.2 The Radical S-Adenosylmethionine Enzyme Superfamily

The ability for enzymes to harness the energy from an organic radical was a novel idea in the 1960's. Until then, it was thought that all biological processes used paired electron species to perform any chemical reaction needed within an organism. The study of cytochrome P450s[88,89], heme-dependent peroxidases[90,91], and adenosylcobalamin (B_{12}) enzymes[92] changed this paradigm, as it was shown that organic radicals can be used to perform unique chemical transformations that would be otherwise impossible. Moreover, these transformations are involved in essential metabolic pathways, and, thus have gained much attention.

The discovery and definition of the radical SAM superfamily can be traced to the 1970's. From 1970 to 2000, only six distinct enzymes were characterized, all within the prokarya domain. It wasn't until 2001 when the term "radical SAM enzyme" was coined and over 600 sequences were identified by computational analyses of common primary structure features[93]. To date, there are more than 113,000 sequences belonging to the superfamily, with approximately half of the sequences have been assigned with known function[94]. Within this superfamily are 51 subgroups and 92 different families, creating a unique structural, sequential, and mechanistic diversity to comprise the 66 different reactions known with more to be characterized.

This section will give a brief history of radical enzymes with a focus on the early history and common themes in the radical SAM superfamily before investigating the radical SAM methyltransferases and the uncharacterized HemN-like proteins.

Early History of Radical SAM Enzymes

Lysine-2,3-aminomutase: The First Radical SAM Enzyme Characterized

With the increasing attention on the B_{12}-dependent enzymes came the discovery of lysine-2,3-aminomutase (LAM), which is responsible for the interconversion of L-lysine to L-β-lysine in *Clostridium subterminale*[95,96] (Table 1.2). LAM was initially purified on the benchtop under a stream of argon; the activity was stimulated by excess ferrous iron and pyridoxal 5'-phosphate (PLP) while being absolutely dependent on SAM and a chemical reductant with a low reducing potential. Similar to the mechanism of other B_{12}-dependent enzymes, LAM catalyzes the cross migration of the α-amino functional group and the β-carbon pro-R hydrogen without solvent exchange of protons and in the absence of adenosylcobalamin[95,97]. Instead, the reaction was dependent on SAM, generating the hypothesis this enzyme uses the 5'- deoxyadenosyl moiety similar to the B_{12} enzymes. Furthermore, it was then proposed the use of SAM as an evolutionary predecessor to adenosylcobalamin. The use of a simple molecule involved in free-radical generation allows for the evolutionary production of adenosylcobalamin in progressive increments[98] and provides a plausible mechanism for early evolution biological processes.

It wasn't until 1987, when tritium labeled 5'-deoxyadenosyl hydrogen was shown to be responsible for hydrogen transfer in the reaction catalyzed by LAM[99]. Unexpectedly, LAM used S-adenosylmethionine as a coenzyme, whereas the other SAM-dependent methyltransferases known used the molecule as a co-substrate. The use of SAM in this reaction was labeled as "a poor man's adenosylcobalamin" by Perry Frey[98]. However, it would not become apparent until later that radical SAM enzymes represent a major share of the radical-based enzymes.

Glycyl Radical Enzymes and the Partnering Activating Enzyme

Glycyl radical enzymes (GRE) are a family of enzymes that, once activated, utilize a stable glycyl radical intermediate to perform the corresponding reaction. These enzymes are involved in some essential, anaerobic metabolic pathways in microorganisms[100]. The glycyl radical is generated with the help of a partnering activating enzyme (GRE-AE), which are radical SAM enzymes that generate the 5'-deoxyadenosyl radical (5'-dA•) to abstract a specific hydrogen atom from a glycine residue on the GRE. This glycyl radical is shared with a nearby cysteine and forms a cysteinyl radical to provide a powerful oxidant with considerable catalytic power.

The most studied of these systems is pyruvate formate lyase (PFL) and its activating enzyme, PFL-AE. These are responsible for the cleavage of pyruvate to formate and acetyl-CoA and were first described in the 1940's[101]. It was another 40 years before Knappe and co-workers provided evidence for the activation of PFL by the activating enzyme to generate an organic radical on a PFL glycine residue[102]. Other GRE and GRE-AE systems characterized thus far are those of anaerobic ribonucleotide reductase (aRNR) and aRNR-AE[103], glycerol dehydratase (GD) and GD-AE[104], hydroxyphenylacetate decarboxylase (HPD) and HPD-AE[105], and benzylsuccinate synthase (BSS) with the partnering activating enzyme BSS-AE[106]. These GREs have common structural and mechanistic features within the catalytic core domain with variable domains associated with the enzyme as a whole.

Common Classification Themes of Radical SAM Enzymes

Radical SAM enzymes have the ability to generate a highly oxidizing and unstable organic radical similar to B_{12}-dependent enzymes but with a more extensive diversity[107]. The defining feature of these enzymes are the ability to coordinate a [4Fe-4S]$^{+/2+}$ with a conserved $CX_3CX\psi C$ motif (ψ = phenylalanine, histidine, tyrosine, or tryptophan). In this

feature, three of the four iron atoms are coordinated by cysteine residues, and the fourth iron, often called the unique iron, coordinates the carboxy and amino ends of the methionine in S-adenosylmethionine. Upon introducing an electron into the system, the active [4Fe-4S]$^{+}$ reductively cleaves the SAM molecule to generate a 5'-deoxyadenosyl radical[108,109]. Although this radical has never been directly observed, the use of radiolabeled SAM, and allylic SAM analogs has given substantial evidence for a radical intermediate at the 5'-carbon[99,110]. Another common feature within the superfamily is a glycine-rich motif involved in binding and positioning SAM in the active site, thereby allowing for the coordination to the unique iron and correct positioning of the methionine moiety within the active site[93,111].

With these common characteristic features, radical SAM enzymes can be classified into three categories based on the fate of the 5'-deoxyadenosyl radical[112]. The first class uses SAM as a coenzyme by regenerating the 5'-dA• at the end of the catalytic cycle. Generally, the proteins in this class are capable of thousands of turnovers *in vitro*, thus allowing for in depth kinetic analyses. Class II are known better as glycyl radical enzyme activating enzymes. These radical SAM enzymes generate the 5'-dA radical to abstract a hydrogen atom from a glycine residue on the partnering glycyl radical enzyme. This event will initiate catalysis by abstracting a hydrogen atom from the substrate, and then will reform the protein radical at the end of the catalytic cycle. Finally, class III enzymes use SAM as a co-substrate, and cannot regenerate the radical at the end of the catalytic turnover, resulting in few turnovers *in vitro*. This is primarily due to the buildup of SAM cleavage products, which can have a potent inhibitory effect[113,114].

Radical SAM Core Fold

Most radical SAM enzymes share a common fold consisting of six α/β motifs arranged similar to a TIM barrel with the helicies on the outside of the inner parallel sheets. Historically, the TIM barrel fold consists of eight antiparallel α/β motifs creating a full 360 barrel.

The radical SAM core fold is often described as a ”partial TIM barrel” or ”$^3/_4$ TIM barrel”, resulting in less curvature and a more outspread display. Although, these partial TIM barrels seem to be more common within the radical SAM enzymes that have been crystallized, a full barrel can be observed in the structures of BioB[115], ThiC[116], and HydE[117]. Exposure of one β sheet is a result of the partial barrel fold and can be ”plugged” with other non-core protein elements. Since the active site lies within this opening, the plug creates an isolated environment for the harboring of a radical intermediate to prevent side reactions with solvent. A superimposition of the radical SAM core has been shown by Drennan *et al.*, aligning PFL-AE, HemN, BioB, MoaA, LAM, phTYW1, and HydE starting from the N terminus of the strand that leads into the cluster binding loop and ending with the C terminus of the sixth strand results in a highly conserved structural overlay (Figure 1.4). Notably, the structures diverge at the cluster-binding loop and at strand β_6, for the accommodation of substrates. Despite the conservation in the catalytic core, the wide range of substrates an activities suggest a modulative platform for catalysis.

HemN and HemN-like Enzymes

HemN: The Oxygen-Independent Copropophryinogen III Oxidase

HemN is a radical SAM enzyme responsible for the anaerobic conversion of coproporphyrinogen III to protoporphyrinogen IX in the protoporphyrin-dependent branch of heme biosynthesis. This branch is identified in the majority of gram-negative bacteria and is largely absent from the gram-positives, which synthesize heme via formation of coproporphyrin rather than protoporphyrin[118]. In the oxygen-independent protoporphyrin-dependent branch of heme biosynthesis, HemN decarboxylates the propionate side chains located on the A and B pyrrolic rings to form corresponding vinyl substituents. This activity was first observed by Tait *et al.*[119,120]. However, the characterization of the enzyme was reported 30 years later[121]. In this report, activity of purified HemN from *E. coli* required NAD(P)H,

flavodoxin, flavodoxin oxidoreductase, acquired from cytoplasmic extract, SAM, and an unidentified factor, presumably an electron acceptor with a molecular weight above 10 kDa, to decarboxylate coproporphyrinogen III[121].

The mechanism by which HemN decarboxylates the two propionate groups was addressed in two follow-up studies. The first addressed the question of the substrate radical and the specific hydrogen abstracted from the substituents[122]. In short, the pro-S-hydrogen at the β-position is specifically abstracted and in the absence of the unidentified electron acceptor, produces a stable substrate radical. Based on the use of deuterated substrate, electron paramagnetic resonance spectroscopy strongly supported the formation of a resonance stabilized radical and included carbons 3', 3, and 4 based on g values[122]. The second study addressed the order of decarboxylation and whether or not the propionate on the A or B ring is decarboxylated first[123]. Interestingly, an intermediate was identified by HPLC and mass spectrometry as a monovinyltripropionic acid porphyrin, and only the proposed intermediate, harderoporphyrin, could be converted to protoporphyrinogen IX when used as the substrate in the activity assay[123].

The structure of HemN from *E. coli* was solved to 2.07 Å resolution with a final R-factor of 0.154 (R_{free} = 0.187)[124]. Phases were solved using multiple anomalous difference (MAD) techniques by diffraction data collected near the K-edge for iron. HemN adopts an $(\alpha\beta)_6$ partial TIM barrel as described above. The structure of HemN provided evidence for the binding of two SAM molecules at two distinct sites adjacent to one another. The first SAM molecule, termed SAM1, coordinates to the 4Fe-4S similar to other radical SAM enzymes, while SAM2 binds adjacent to SAM1. Though partially disordered, the electron density shows a defined ribose moiety and the anomalous difference map supports the presence of the sulfonium atom.

The catalytic function of the SAM2 was addressed in a follow-up study that used site directed mutagenesis of Y56A(L), E145A(I), F310A(L), Q311A, and I329A amino acids,

which were the residues responsible for SAM2 coordination[125]. Although all mutants coordinated an iron-sulfur cluster, albeit to a lower degree than wild type, only F310A still had residual CPO Activity (1.5%). Strikingly, only the mutants of F310A(L), Q311A, and I329A could still cleave SAM to produce methionine. These data suggested the SAM2 site was not just an artifact in the crystal structure, but indeed has a catalytic role. It also would suggest that the 5'-deoxyadenosyl radical is generated before decarboxylation of the first propionate. Considering the effects of these mutations, it would be interesting to test HemN catalytic viability on harderoporphyrin to further probe the enzyme mechanism.

HemN-like enzymes

The development of annotation tools by computational bioinformatics has provided insight for predicting the function of large families of enzymes. However, due to the lack of biochemical confirmation of these assignments and the error these analyses are prone to, high levels of missannotation in superfamilies are commonly observed[126]. For example, the broad classification of HemN has presented difficulties in identifying an alternative pathway for heme biosynthesis[118]. A detailed analysis of the *hemN* gene cluster compared the genomic context and sequence alignment of the broadly classified HemN domain, which revealed four groups within the protein family[118]. Group A comprise of the bona fide anaerobic coproporphyrinogen oxidases (CpdH) based on the conserved motifs essential for activity[124]. Group B consist of *hutW* from *V. cholerae* and *E. coli*, which is found associated with the genes involved in heme uptake[9]. Group C is the least understood, and is often associated with nucleoside metabolism genes. The final group to be identified in this analysis, Group D, consists of *hemNs* and *hemZs* from many gram-positive bacteria.

Another subset of genes within the HemN-like classification is *hemW* or *yggW*, which has some similarities to Group B HemNs[118], and are void of CpdH activity[127,128]. HemW was characterized from *Lactococcus lactis*, an organism that cannot synthesize heme but

can utilize exogenous protoporphyrin IX or heme in the medium to allow for respiratory growth. The protein was purified with an iron-sulfur cluster after over-expression in *E. coli*. Although the protein was a dimer in solution, upon loss of the cluster, HemW became monomeric. Unexpectedly, heme bound to each form of the protein with an affinity of 8 μM. Since HemW did not have *in vitro* or *in vivo* CPO activity but could bind heme, the authors hypothesized the enzyme functions as a heme trafficking protein[128].

Radical SAM Methyltransferases

The biological importance for methylation reactions have been established. Not only are there a variety of substrates methylated, but also new mechanisms are becoming known. The classical methyltransferases use S_N2 mechanisms for the methylation reactions, where a strong nucleophile is used for the attack of the electrophilic methyl group of SAM. However, these new mechanisms for methyl transfer observed utilize a radical SAM domain, and in some cases other cofactors for the methylation of inert carbon and even phosphorous atoms. These radical SAM methyltransferases (RSMTs) comprise of almost 10% of the enzymes within the recognized radical SAM sequences, all with substantial diversity within the mechanistic features of the enzymes. The RS methyltransferases were first assigned by Zhang *et al.* in 2012, into three classes (class A, B, and C) and separated them by cofactor requirement, reaction mechanism, and even protein domains[129]. Recently, a new class was established (Class D), which is involved in for the biosynthesis of methanopterin, an important cofactor used in C1 metabolism during methanogenesis. The following below will highlight the literature on the RSMTs known to date.

Class A Radical SAM Methyltransferases

These enzymes, represented by Cfr and RlmN, are responsible for the methylation of adenosine 2503 (A2503) in 23S rRNA at the C8 and C2 position, respectively. RlmN,

although nonessential in *E. coli*, enhances translation fidelity and fitness of the bacterium[130]. Additionally, Cfr confers antibiotic resistance to a minimum of 5 classes of currently prescribed antibiotics targeting the 50S subunit of the bacterial ribosome[131]. These proteins contain only a RS domain and are the best understood of the RSMTs.

The most recent mechanism proposed by the Booker lab is shown in Figure 1.5[132]. During the initiation of the reaction for RlmN, the first SAM molecule coordinated to the unique iron within the Fe-S center undergoes a nucleophilic attack by a conserved cysteine residue (C355) using an S_N2 mechanism to form a methyl-cysteine (mCys)[133]. S-adenosylhomocysteine is replaced with a second SAM molecule in the same position as SAM1, as observed in the crystal structure[134]. Upon reductive cleavage of the newly coordinated SAM molecule, the 5'-dA radical abstracts the hydrogen from the newly transferred methyl group to produce a methylene radical[135,136]. The radical then adds to the C2 of the adenosine to form a cross-linked protein-RNA radical intermediate via radical addition[137]. This adduct was further substantiated with the structure of $RlmN_{C118A}$ crosslinked to a tRNA molecule[132]. The latter steps of the mechanism remain uncharacterized. The original mechanism supported two adjacent cysteine residues involved in forming a disulfide bond, and loss of an electron to allow for product release following tautomerization of the enamine[138]. However, the most recent report suggested thiyl radical formation on C355 which could protected by crosslinking with a nearby methionine to form a thiosulfuranyl radical. This is not unprecedented, as it is observed in the *E. coli* class III ribonucleotide reductase[139]. To resolve the thiyl radical, an additional electron would be needed to restart the catalytic cycle.

Class B Radical SAM Methyltransferases

Unlike the class A enzymes, class B are able to methylate either sp^2-hybridized or sp^3-hybridized carbon atoms or phosphinate phosphorous atoms. It also represents the largest

and most diverse class of the RSMTs, and is identified by an N-terminal cobalamin binding domain (CBD) and a core radical SAM domain. Due to the difficulty associated with the heterologous overexpression of a soluble form, the progression of characterizing the class B methyltransferases is lacking. In fact, of the four enzymes that have been studied *in vitro* (TsrM, PhpK, Fom3, and GenK), only TsrM was not purified from insoluble inclusion bodies[140,141].

PhpK is a p-methyltransferase that catalyzes the methylation of the phosphinate group of 2-acetylamino-4-hydroxyphosphinylbutanoate (NAcDMPT) to produce 2-acetylamino-4-hydroxymethylphosphinylbutanoate (NAcPT). This product, commonly known as glufosinate, is used as a herbicide as it inhibits the plant and bacterial glutamate biosynthetic pathway[142]. The use of NMR and radiolabeled NAcDMPT substrate supported the activity of this enzyme as a methyltransferase[143]. However, the reaction lacking sodium dithionite abolished this activity suggesting a radical-type reaction[143]. Finally, performing the assay in the presence of [methyl-^{13}C]-methylcobalamin indicated the methyl group transferred to the phosphinate group originates from methylcobalamin[143].

The class B radical SAM methyltransferases known to methylate *sp*^{3}-hybridized carbon centers consist of Fom3 and GenK. Fom3 converts 2-hydroxyethylphosphonate (HEP) to S-2-hydroxypropylphosphonate (HPP) by stereospecific methylation[144]. HPP is a metabolic intermediate in the fosomycin biosynthetic pathway, a broad-spectrum antibiotic. Similarly to PhpK, the activity by Fom3 was assessed *in vitro* by using isotopic labeledsubstrates and NMR[144]. Feeding studies with [methyl-^{14}C]-cobalamin indicated the methyl group originating from methylcobalamin[145].

GenK methylates the *sp*^{3}-hybridized C-6 carbon of gentamicin X_2 (GenX_2), an intermediate in the biosynthetic pathway of gentamicin C1. Similar to the other Class B RSMTs described above, GenK was purified from insoluble inclusion bodies before refolding and reconstituting the Fe-S center[140]. Most notably from the characterization of the activity of

GenK, when using [methyl-$^{13}CH_3$]-SAM, the isotopic labelwas observed on both methylcobalamin and the product G418 indicating the transfer of the methyl group to cobalamin initially before the GenX_2 substrate.

The last class B enzyme characterized, TsrM, is responsible for the methylation of tryptophan on the *sp*^{2}-hybridized C-2 carbon center of the indole ring to produce methyltryptophan (mTrp). This mTrp is used as an intermediate in the thiostrepton A biosynthetic pathway, a thiopeptide natural product with antibacterial and antitumor activity[146]. TsrM was purified with affinity chromatography, unlike the other cobalamin-dependent radical SAM methyltransferases[147]. Interestingly, although the production of *S*-adenosylhomocysteine (SAH) was observed, 5'-dA was not despite the considerable levels of mTrp produced. Turnover occurred in the absence of a strong reductant, which suggest TsrM evolved a radical SAM domain but does not utilize a radical mechanism. Consistent with this observation, a study published by Blaszczyk *et al.* did not observe S-adenosylmethionine coordination to the [4Fe-4S] cluster using ENDOR and HYSCORE spectroscopies[141].

Class C RS Methyltransferases

Class C RSMTs are the least understood of the RS methyltransferases. According to the Structure-Function Linkage Database (SFLD)[94] there are only 17 members that belong to this subgroup of the radical SAM methyltransferases, however, many of these enzymes have similar sequences to HemN. In fact, some are even mis-annotated as a HemN or "HemN-like" protein and likely results in the lower than estimated value of these class C enzymes. These enzymes are only known to methylate *sp*^{2}-hybridized carbon atoms. However, unlike the class A radical SAM methyltransferases, there are no conserved cysteines outside of the CX_3CX_2C motif. Thus, these enzymes are likely to utilize a novel mechanism for methylation, presumably via radical abstraction from the hydrogen on the S-methyl group of SAM with subsequent radical addition on the *sp*^{2}-hybridized

carbon center[148]. Considering the relative homology to HemN, this class of the radical SAM methyltransferases may bind two SAM molecules, one for the generation of the 5'-dA radical (SAM1) and the other as the methyl donor (SAM2). This was addressed by Zhang *et al.* when compiling the sequences between HemN and the Class C RS methyltransferases to show the conservation of the residues involved in binding SAM2. In addition to the two conserved SAM binding sites, the class C enzymes also have a C-terminal domain (CTD) with homology to the CTD of HemN. This CTD was presumed to be involved in substrate recognition by HemN based on the structure[124].

To date, the class C radical SAM methyltransferases identified have only been shown to be involved in the biosynthesis of secondary metabolites and antibiotics. In depth analyses of these enzymes within the biosynthetic pathways have been limited due to the inability to obtain physiological substrates. This difficulty to overproduce the metabolites within an organism is primarily due to the lack of knowledge of the sequence of steps within each pathway. Only one of the class C enzymes have been studied *in vitro*, YtkT, which in involved in the biosynthesis yatakemycin. The presumed [4Fe-4S] cluster was chemically reconstituted and activity described. Using HPLC and mass spectrometry it was shown that under assay conditions YTM-T (substrate) was converted to MeYTM-T, however, the mechanism by which this conversion occurs is still unknown.

The lack of analysis for these enzymes is the primary reason the majority of the class C enzymes have relied heavily on feeding studies to characterize their function. Examples are that of NosN and NocN, which are involved in the biosynthesis of the heavily modified thiopeptide antibiotics Nosiheptide and Nocathiacin. These antibiotics are known to exhibit an effective lethal dose on medically relevant opportunistic pathogens, such as *S. aureus*[149], making these natural products an attractive target for pharmaceuticals. One unique moiety associated to these thiopeptide antibiotics are the indole ring modification that originates from tryptophan. NosN and NocN are responsible for the methylation at

the C4 position, which is a *sp*^{2}*-hybridized* carbon atom[150,151]. This modified indole ring is ligated to the amino acid framework of the thiopeptide downstream of the methylation.

Lastly, the biosynthetic gene cluster for the antifungal agent jawsomycin was identified from *Streptoverticillium ferven* HP-891. Jawsomycin is a cyclopropanated fatty acid, derived from polyketide biosynthesis, linked to 5'-amino-5'-deoxy-5,6-dihydrouridine. Isotopic labeling studies suggested the methylene groups of the cyclopropane rings originated from L-methionine[152]. Additionally, *jaw5* was noticed to encode a protein sequence with a CX_7CX_2C motif and significant homology to HemN. With the assumption that Jaw5 is a radical SAM enzyme, two mechanisms by which this reaction could occur were proposed[148].

Class D RS Methyltransferases

The Class D RSMTs are the most recent addition to the radical SAM methyltransferase subfamily, however, only one enzyme has been reported. The enzyme MJ0619 was shown to be involved in methanopterin biosynthesis by catalyzing the transfer of a methyl group from methylenetetrahydrofolate to the 7 and 9 positions on the pterin ring[153]. This was the first radical SAM methyltransferase that was shown to transfer a methyl group of which does not originate from S-adenosylmethionine. Upon growing *E. coli* with deuterium-labeled acetate in the media and expressing the enzyme, the resulting methyl group contained 3 deuterium atoms. A mechanism was proposed involving hydrogen abstraction of the C7 hydrogen atom from the 5'-dA radical. The intermediate is predicted to form a covalent bond to the N5-methylene carbon atom by radical addition followed by collapse of the radical species with the addition of an electron and proton. The product is release following a series of acid-base chemistry reactions. The methylenetetrahydrofolate cofactor is regenerated with three NADPH molecules, which would result in a total of a 5 electron process. This is the first radical SAM methyltransferase that transfers a methyl group that

does not originate from SAM, but rather uses SAM to generate a radical on the cofactor.

Table 1.2: Radical SAM Enzymes characterized before 2001

Name	Reaction	Reference(s)
	S-adenosylmethionine: cofactor	
LAM		95
	S-adenosylmethionine: cosubstrate	
GRE-AEs		102
HemN	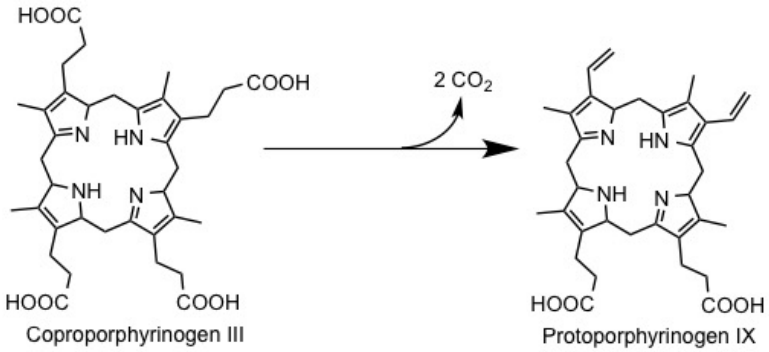	154
LipA		155

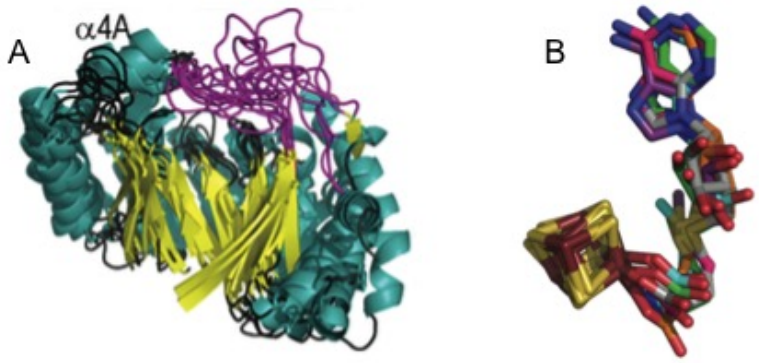

Figure 1.4: This figure was adapted from Vey *et al.*[156]. (Panel A) The superimposition of the catalytic core domain for PFL-AE, HemN, BioB, MoaA, LAM, TYW1, and HydE from a frontal view. (Panel B) An overlay of the 4Fe-S center coordinated to S-adenosylmethionine shows the structural homology of the active site cofactors within the enzymes listed.

Table 1.3: Radical SAM Methyltransferases

Class	Name	Function	Reference	Substrate
A	Cfr	rRNA modification	157	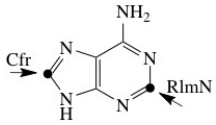
	RlmN	rRNA modification	158	
B	Fom3	Fosfomycin biosynthesis	159	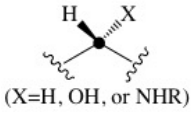
	Fms7	Fortimicin A biosynthesis	160	
	GenE and K	Gentamicin biosynthesis	140	
	ThnK, L, and P	Thienamycin biosynthesis	161	
	PacJ, N, and O	Pacidamycin biosynthesis	162	
	CndI	Chondrochlorens biosynthesis	163	
	Swb9	Quinomycin biosynthesis	164	
	BchQ and R	Chlorophyll biosynthesis	165	
	CapT	A-500359 A biosynthesis	166	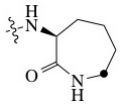
	Clon6	Chlorobiocin biosynthesis	167	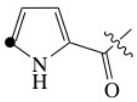
	CouN6	Coumermycin biosynthesis	168	
	TsrT (TsrM)	Thiostrepton biosynthesis	146,169	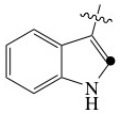
	SioT	Siomycin biosynthesis	169	
	PhpK	Bialaphos biosynthesis	170	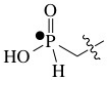

C	NosN	Nosiheptide biosynthesis	150	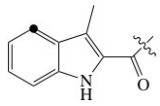
	NocN	Nocathiacin biosynthesis	151	
	TpdI	Thiomuracin biosynthesis	171	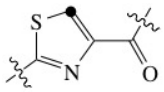
	TpdU and L	GE 2270 biosynthesis	171	
	Blm-Orf8	Bleomycin biosynthesis	172	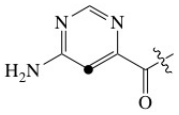
	Tlm-Orf11	Tallysomycin biosynthesis	173	
	Zbm-Orf26	Zorbamycin biosynthesis	174	
	YtkT	Yaktemycin biosynthesis	175	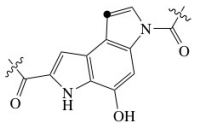
D	MJ0619	Methanopterin biosynthesis	153	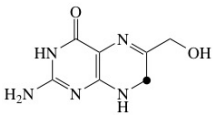

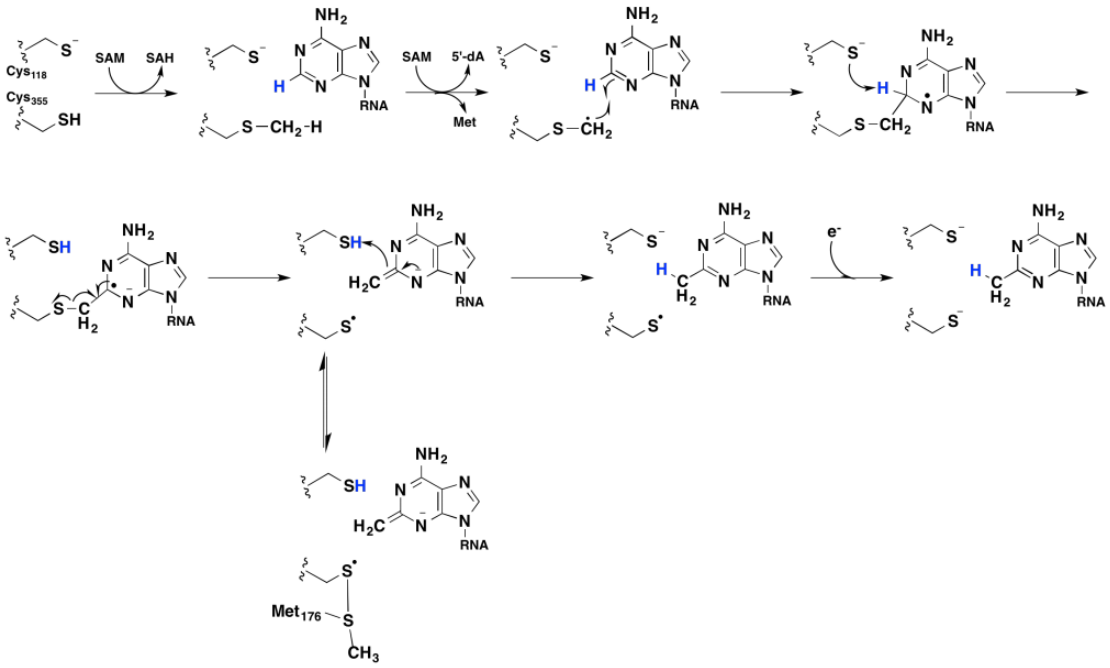

Figure 1.5: Proposed mechanism of RlmN proposed by Schwalm *et al.*[132]

1.3 HutW and the Heme Utilization Operon

For nearly 50 years, Heme oxygenases (HO) were presumed to be the only enzymes to degrade heme. The discovery and characterization of the HO-like enzymes IsdG, IsdI, and MhuD was a paradigm shift by demonstrating various mechanisms to acquire heme-iron existed based on the pathophysiology of the organism. Considering the differences in the verdin product, these organisms presumably metabolize the corresponding tetrapyrrole differently. However, despite the identification of the HO and HO-like genes within a variety of bacteria, homologues are not identified in many proteobacteria. Interestingly, many genera that do not harness a similar heme degrading enzyme encode the genes *hutWX(Y)Z*, which can be adjacent to or associated with the well-characterized heme uptake machinery. These genes are negatively regulated by the ferric uptake repressor and are only expressed during iron duress.

The difficulty with the classification of this operon lies in the variability of the gene names. For instance, some organisms have the genes *hutWXY*, whereas others will encode *hutWXZ*. Despite the high homology of the W's and X's, Z and Y genes have no sequential homology. Moreover, it is unclear if these two gene products can functionally replace one another. Although the genes in this operon are homologous between organisms, the names of the genes are dependent on the species it came from, making discussion difficult. For simplicity, each operon will be represented as "Hut", for Heme utilization, followed by the specific gene(s) identifier in an attempt to standardize the naming scheme. For instance, ChuW from *E. coli* will be referred to as *E. coli* HutW.

HutW

HutW is an annotated radical SAM enzyme with similar domain sequences to HemN, of which it was originally annotated. In some respect, this mis-annotation persists for many

bacteria, including *E. coli* O157:H7. To this end, BLAST searches of the HutW sequence will often result in positive hits with HemN due to the high sequence similarity. Thus, the search must be modified to reject sequences with E-values greater than at least 10^{-30}. One way the sequence can be confirmed as a bonafide HutW is by searching the adjacent genes in that genome, as *hutX* and *hutZ(Y)* seem to follow *hutW*. The sequence can also be searched on the Structure-Function Linkage Database (SFLD)[94], which provides a small uncharacterized protein family with the HemN sequences. Though it is unlikely this is a completed list, up to 43 genera are identified to encode *hutW*, all of which are adjacent to genes that supposedly encode the heme uptake machinery (Table 1.4).

Little is known about the function of HutW. Genetic analysis on the Hut operon has been performed with *V. cholerae* and *Plesiomonas shigelloides*[9,176]. Knockout studies of HutW resulted in no observable growth phenotype[9]. These results suggested *V. cholerae* HutW is not essential for the growth of the organism during iron duress, albeit under non-pathophysiological conditions. These observations further complicate the ability to study the function of this gene without using an animal model.

HutX

The adjacent gene to *hutW* in the heme utilization operon is *HutX* and is the second least characterized gene of the three. It belongs in the Duf399 protein family, and has been proposed to be a heme binding protein in *E. coli* O157:H7[177]. *E. coli* HutX has a similar structural fold to the hemoproteins *E. coli* HutS and *E. coli* HemS. Based on rR spectroscopy and mutational analysis *E. coli* HutX binds heme in a mixture of coordination states; 5-coordinate HS, as well as, 6-coordinate HS and LS with either 1 or 2 Histidine ligands, respectively. Despite the ability to bind heme, mutation of *V. cholerae* HutX results in no observable growth phenotype. The homologue from *V. cholerae* was also shown to donate the heme bound to *V. cholerae* HutZ, however, this interaction observed had 750

μM dissociation constant that did not change using holo-HutX[178]. Considering the relatively low affinity this protein-protein interaction, it may not be physiological and suggests heme transfer may be due to a higher affinity for heme by *V. cholerae* HutZ.

HutZ and HutY

The last gene in the operon can be either *hutZ* or *hutY* depending on the genus. HutY is predominately found in the enterobacteriaciae family, whereas HutZ is primarily found in the Vibrionaciae families. To date, no reports regarding the function of HutY have been published, and therefore it is the least characterized. It is annotated as an NAD(P)H oxidoreductase, specifically, an atypical short-chain dehydrogenase (aSDR), which belongs to the same subfamily as biliverdin reductase. This annotation is due to the non-canonical sequences for the NAD(P)H dehydrogenase motif making it difficult to identify the function using bioinformatics[179].

The most well-characterized gene within the operon, *hutZ*, have contradicting reports that have created confusion as to the function. Genetic analysis of a *hutZ* knockout from *V. cholerae* and *Plesiomonas shigelloides* resulted in a loss of viability on iron-depleted medium[9,180]. Interestingly, to restore growth to wild type conditions, *V. cholerae* HutZ and *V. cholerae* HutW must be present, and neither alone can fully restore growth individually[9]. However, *V. cholerae* and *P. shigelloides* HutZ alone can rescue the organism to a moderate level by what was proposed via a heme buffering ability[9,180]. When purified, *Vc* and *P. shigelloides* HutZ could be reconstituted with heme, however, neither enzyme possessed any observable heme oxygenase activity[9,180].

These genetic analyses are in contrast to the HutZ homologue from *Helicobacter pylori* and *Campylobacter jejuni*, which were observed to have heme oxygenase activity[181,182]. Interestingly, the UV-visible activity assay of the *H. pylori* HutZ appears to only produce verdoheme, suggesting that the conversion from verdoheme to biliverdin IXδ is not dependent

on the enzyme[182]. Thus, it is unclear if *H. pylori* HutZ is a bonafide heme oxygenase.

It is important to note the differences of *H. pylori* HutZ from other homologues characterized. First, the *H. pylori* genome does not encode the HutW or HutX homologues, making *H. pylori* HutZ unlikely to contain an identical function to other HutZ homologues with the respective upstream genes. Secondly, *H. pylori* HutZ has an additional domain not observed in the *V. cholerae* or *P. shigelloides* HutZ, which may result in the difference of activity[183]. The structural scaffolding of *V. cholerae* HutZ is described as an FMN-binding split barrel fold, thus, it overlays well with pyridoxal 5'-phosphate oxidase[184]. Taken together, these two proteins may, in fact, have different functions. However, the assigned function of these proteins as non-canonical heme oxygenases are not unanimously accepted in the field[10].

hutWXY vs hutWXZ

Other notable observational differences within these operons lie in the subtle divergence between HutW homolgues. HutW from operons containing *hutY* seem to have slightly different sequences than HutW containing a *hutZ* downstream, albeit with E-value cutoffs of 10^{-80}. Whether or not this divergence results in a difference in activity is unclear. Additionally, whether or not one of the HutW homologues can replace the diverged HutW homologue is also unclear.

Finally, it is interesting to point out that organisms that do not express HutZ contain HutS, the protein shown to be involved in heme trafficking in *S. dysenteriae* and *P. aeruginosa*[64,185]. A HutS homologue is not present in organisms that contain a HutZ within the heme utilization operon, and based on the observation that HutZ provides an increased buffering capacity for cytoplasmic heme[9], it is also possible HutZ can functionally replace HutS. These predictions leave many questions to be addressed. Nevertheless, it is clear these organisms do not acquire or utilize heme identically, which provide highly specific

targetable mechanisms for many pathogenic bacteria to aid in treatment of infection.

Concluding Remarks

Considering the bioinformatics of the heme utilization operon presented, it is evident these three genes are involved in acquiring heme-iron. Based on the absence of any bona fide heme oxygenase as well as the lack of HutZ HO activity from from *V. cholerae* and *P. shigelloides*, these organisms likely contain another enzyme that is responsible for the degradation of heme. It is well established that radical SAM enzymes perform essential oxygen-independent chemical reactions and are often found in operons where they are absolutely needed due to the lack of a functionally equivalent enzyme. Considering the expression of an iron-sulfur protein during iron duress provides circumstantial evidence for the importance of this enzyme. We propose that the *Escherichia coli* O157:H7 HutW is an oxygen-independent heme degrading enzyme that harnesses the energy from a radical mechanism to modify the tetrapyrrole ring to release the essential metal iron. As a means to further process the tetrapyrrole, we also propose *Ec* HutY, when present, serves as an analogous enzyme to biliverdin reductase and reduces the product of the *Ec* HutW reaction. This is the first anaerobic heme degradation pathway of its kind and the following chapters will support this claim.

Table 1.4: Identification of ChuW Homologues

Genus	Species	Serotype	Gene Identifier (GI)
Actinobacillus	*pleuropneumoniae*		307248565
Aeromonas	*hydrophila*		117617608
	salmonicida		209695230
Allochromatium	*vinosum*		288941408
Bacillus	*cereus*		28900282
Bilophila	*wadsworthia*		317487039
Burkholderiales	*bacterium*		303257941
Citrobacter	*koseri*		157146881
Denitrovibrio	*acetiphilus*		291286743
Desulfurispirillum	*indicum*		317052185
Edwardsiella	*tarda*		387867751
Eikenella	*corrodens*		225024396
Escherichia	*coli*	O1:K1	386606098
		O127:H6	312968176
		O157:H7	15833637
Ferrimonas	*balearica*		308048714
Grimontia	*hollisae*		262274017
Haemophilus	*ducreyi*		33151310
Halorhodopira	*halophila*		121997193
Hypomicrobium	*dentrificans*		300022130
Klebsiella	*pneumonia*		153838952
Laribacter	*hongkongensis*		226940122
Manheimia	*haemolytica*		261494665
Pectobacterium	*atrosepticum*		50121932
Phascolarctobacterium	*succinatutens*		323141788
Photobacterium	*damselae*		269102794
Plesiomonas	*shigelloides*		13774061
Rhodobacter	*capsulatus*		294675708
Rhodopseudomonas	*palustris*		86747291
Rhodospirillum	*centenum*		209967082
Shewanella	*halifaxensis*		167625322
Selenomonas	*artemidis*		320530554
Sutterella	*wadsworthens*		319940966
Veillonella	*atypical*		303230274
	parvula		269798395
Vibrio	*albensis*		229526534
	cholerae		298499688
Vibrionales	*bacterium*	SWAT-3	148973948
Yersinia	*enterocolitica*		386311018
	pestis		22124461

CHAPTER 2

A RADICAL NEW PARADIGM FOR HEME DEGRADATION IN *ESCHERICHIA COLI* O157:H7[1]

[1] **Joseph W. LaMattina**, David B. Nix, and William N. Lanzilotta. Submitted to *Proceedings of National Academy of Sciences*, February 24th, 2016.

Abstract

All of the heme-degrading enzymes that have been characterized to date require molecular oxygen as a co-substrate. *Escherichia coli* O157:H7 has been shown to express heme uptake and transport proteins as well as utilize heme as an iron source. This enteric pathogen colonizes the anaerobic space of the lower intestine in mammals, yet no mechanism for anaerobic heme degradation has been reported. Herein we provide evidence for an oxygen-independent heme-degradation pathway. Specifically, we demonstrate that ChuW is a radical SAM methyltransferase that catalyzes a radical-mediated mechanism facilitating iron liberation and the production of the novel tetrapyrrole product we have termed ”anaerobilin”. We further demonstrate that anaerobilin can be used as a substrate by ChuY, an enzyme that is co-expressed *in vivo* with ChuW and putative heme uptake machinery. Our findings are discussed in terms of the competitive advantage this system provides for enteric bacteria, particularly those that inhabit the anaerobic niche of the intestine.

2.1 Introduction

Iron acquisition is essential to the survival of all cellular organisms and is a major barrier for a microorganism during pathogenesis of a mammalian host[186]. For example, an enteric pathogen entering through the digestive tract must compete with the host as well as other intestinal microflora for the acquisition of iron. However, the most abundant source of dietary iron for humans is found in heme[187], a cofactor that is also responsible for essential cellular processes by serving as a cofactor in a variety of enzymes[188]. The degradation of heme also plays an important role in iron homeostasis and cell signaling in cyanobacteria, plants, and mammals[186,189]. Considering the bioavailability of dietary heme and the importance of iron as a nutrient, it is not surprising that pathways have evolved in pathogenic bacteria to transport and degrade heme for the sole purpose of iron acquisition[190]. Furthermore, the ability to accomplish the liberation of iron from heme under strictly anaerobic conditions would be advantageous to the enteric bacteria that can inhabit certain niches of the intestine.

Enzymes that catalyze the opening of the porphyrin ring have been well characterized and are collectively referred to as heme oxygenases[191]. This classification is based on the common mechanistic property of activating molecular oxygen by a ”P450-like” mechanism in order to catalyze the oxidative degradation of the heme cofactor[49,192,193]. Recently, two heme oxygenases have been characterized in the organisms *Staphylococcus aureus* and *Mycobacterium tuberculosis* that degrade heme to the unique chromophores

staphylobilin[53] and mycobilin[59], respectively. Although molecular oxygen is still required, neither of these degradation mechanisms result in carbon monoxide production, presumably due to the pathophysiology of these organisms[54]. These observations advanced the hypothesis that organisms evolved a variety of heme degradation mechanisms in order to satisfy their own physiological needs[10]. Thus raising the question: how do hemolytic organisms utilize heme as an iron source during infection or colonization in an anaerobic environment?

Vibrio cholerae and *Escherichia coli* O157:H7 are hemolytic enteric pathogens that colonize the non-sterile region of the lower intestines. Despite their ability to use heme as an iron source, a bona fide heme oxygenase has not been identified for either organism. However, both organisms contain a heme uptake operon that is upregulated during iron duress[9,194]. The operon encodes for the heme uptake and transport machinery as well as three additional genes, *chuW*, *chuX*, and *chuY*, of unknown function (Figure 2.1, Panel A)[71]. ChuW is annotated as a member of the radical S-adenosylmethionine (SAM) superfamily, which share common cofactor requirements and mechanistic features. These features include coordination of a redox active [4Fe-4S] cluster ligated by three protein-derived cysteine residues, often located within a CX_3CX_2C motif. This coordination environment facilitates the interaction of S-adenosyl-L-methionine (SAM) at the unique iron site of the cluster. In the reduced state (formally 1+), the [4Fe-4S] cluster reductively cleaves SAM, forming a highly oxidative 5'-deoxyadenosyl-5'-radical (5'-dA•) that is subsequently utilized for catalysis. ChuW was originally annotated as the radical SAM enzyme, HemN, or an anaerobic coproporphyrinogen oxidase. HemN is involved in the anaerobic biosynthesis of heme, performing two subsequent decarboxylation reactions to produce protoporphyrinogen IX[121]. However, previous work has shown that ChuW homologues do not retain the essential functional motifs, nor do they rescue a HemN knockout in *S. enterolitica*, and thus likely catalyze a different reaction[9,118]. A role in heme biosynthesis is also inconsistent with the location of the *chuW* gene in an iron-regulated operon and adjacent to genes that are required for heme uptake (Figure 2.1).

Sequence alignments indicate ChuW has homology to the radical SAM methyltransferases (RSMTs). RSMTs are a subfamily of radical SAM enzymes that function in the transfer of methyl groups to unreactive carbon atoms and, in some cases, promote significant chemical rearrangements[129,175]. However, they are the least understood of the four distinct classes[148] making it difficult to determine function or mechanism using only a bioinformatics approach. In order to address the precise function of ChuW from the enterohemorrhagic serotype of *E. coli* O157:H7, we isolated and characterized the recombinant enzyme. Our data provide *in vitro* evidence that ChuW functions as an anaerobic heme-degrading enzyme utilizing a mechanism similar

to what has been reported for another RSMTs.

2.2 Results

Isolation of ChuW with an intact [4Fe-4S] cluster. Similar to what has been reported for other radical SAM enzymes, the most stable form of ChuW was obtained when we co-expressed the *A. vinelandii* iron sulfur cluster (Isc) biosynthesis genes (pDB1282 vector, a generous gift from Dennis Dean) and the *chuW* gene in *E. coli* using minimal media that was supplemented with exogenous iron and cysteine during expression. Isolation of ChuW via this approach yielded a protein with 3.8 $\pm$ 0.2 irons per monomer, following the reconstitution and purification procedure described in the "Supplemental Materials and Methods" section. We investigated the spectroscopic characteristics of the reconstituted enzyme using UV-visible spectroscopy. The purified enzyme exhibited a broad absorption feature with a maximum near 400 nm, consistent with the presence of a [4Fe-4S] cluster (Figure 2.1, Panel B). Injecting incremental aliquots of Ti^{3+}-citrate into the sample resulted in a bleaching of color and decreased the absorption feature around 400 nm. The relative percentage of oxidized ChuW was plotted with respect to the concentration of Ti^{3+}-citrate injected (Figure 2.1, Panel B, inset) and suggests a single electron reduction of the cluster. The oxidation state of the [4Fe-4S] cluster was further investigated by electron paramagnetic resonance (EPR) (Figure 2.1, Panel C). In the presence of sodium dithionite, we observed an axial EPR spectrum ($g_{||}$= 2.04, $g_{\perp}$ = 1.92) (Figure 2.1, Panel C, spectra ii.) that is typical for radical SAM enzymes that contain only the catalytic [4Fe-4S] cluster[125,195]. Similar to other radical SAM enzymes, the [4Fe-4S] cluster of ChuW is oxygen sensitive and enzyme activity is lost if exposed to molecular oxygen.

Flavodoxin is the electron source for the radical SAM enzyme ChuW. Protein sequence analysis indicates that ChuW is distinct from HemN and more similar to the class C radical SAM methyltransferases (RSMTs) (Figure 2.2). Therefore, we looked for both 5'-deoxyadenosine (5'-dA) and S-adenosylhomocysteine (SAH) production during ChuW turnover by high-performance liquid chromatography (HPLC). In our assays, we used the heme analog deuteroheme as the substrate because it has greater solubility in aqueous solution than hemin. Consistent with what others have reported[114,196], we observed "abortive cleavage" of SAM to 5'-dA in the absence of deuteroheme when using the chemical reductant sodium dithionite (Figure 2.3, Panel A). SAH production is also minimal when deuteroheme is absent and the chemical reductant is employed (Figure 2.3, compare Panels A and B). However, when using the *E. coli* flavodoxin (FldA)/ferredoxin (flavodoxin):NADP+ oxidoreductase (Fpr)/NADPH system[196], both 5'-dA and SAH were produced at 1:1

stoichiometries when substrate was present (Figure 2.3, Panel C, trace ii.). Quantitation of iron that was subject to chelation (labile iron) was also performed. Measurements of the total labile iron were performed at the start of the reaction and after 30 minutes. Specifically, we measured 227 $\pm$ 20 μM labile iron at the start of the assay and 302 $\pm$ 27 μM after a 30 minute reaction (Figure 2.3, Panel D).

Heme, mesoheme, and deuteroheme are substrates for ChuW. We monitored the absorption spectrum of either deuteroheme or heme between 350 and 900 nm during a 30-minute reaction using UV-visible spectroscopy (Figure 2.4, Panels A and B, respectively). Turnover of mesoheme was also monitored by UV-visible spectroscopy and the products were analyzed by mass spectroscopy (Figure 2.5, Panel A). Under our assay conditions, deuteroheme was soluble and could be used as a substrate by ChuW, although similar results were found for heme and mesoheme. For deuteroheme, turnover resulted in a decrease in the Soret band at 407 nm with a corresponding increase in absorbance at 439 and 780 nm (Figure 2.4, Panel A). Based on the isosbestic point observed at 418 nm and the initial concentration of deuteroheme, we calculated the extinction coefficient for the product(s) absorbing at 780 nm to be 31.5 mM^{-1} cm^{-1}. Similar results were obtained when the physiological substrate, heme, is used in the assay; albeit, with red-shifted spectral features (Figure 2.4, Panel B). The extinction coefficients for the product allowed for the determination of specific activities by plotting the initial rate of product formation with respect to the concentration of ChuW (Figure 2.4 inset Panels A and B). From this analysis the specific activities were calculated to be 5.5 and 8.4 nmoles min^{-1} mg^{-1} for deuteroheme and heme, respectively. This activity is considerably less than what is observed for hHO-1, roughly 100 nmoles min^{-1} mg^{-1}, when hHO-1 was activity was monitored in a coupled assay with biliverdin reductase[197].

The UV-visible spectrum of the deuteroheme-derived product, hereafter referred to as ”deuteroanaerobilin” (DAB) is altered significantly upon exposure to sunlight for 5 minutes (Figure 2.4, Panel C, dashed spectrum). In contrast, if the isolation procedure was performed while avoiding light exposure of the sample, then the isolated tetrapyrrole had a spectra that was identical to what we observed at the end of the assay (Figure 2.4, Panel C, solid spectrum). HPLC analysis of deuteroanaerobilin was performed to determine if ChuW catalyzes the formation of a single product. Deuteroheme elutes at 15 min, while a single peak for DAB eluted at 5 minutes (Figure 2.4, Panel D, traces i and ii, respectively).

ChuW is a radical SAM methyltransferase that catalyzes the anaerobic liberation of iron and formation of a novel tetrapyrrole. We employed nanospray ionization mass spectrometry (NSI-MS) to address the structure of DAB by direct infusion of the isolated product. When unlabeled SAM was used in the ChuW assay, we observed a dominant peak of 527.8 m/z $[M+H]^+$ (Figure 2.6, Panel A, Spectra i.).

The natural abundance of heavy isotopes is represented by the [A+1] peak in the mass spectrum. In this case, the [A+1] is predominately determined by the number of carbon atoms in that molecule. For DAB, the 528 m/z [A+1] peak is 34% of the parent ion consistent with a molecule containing 31 carbon atoms. This observation was further substantiated by analysis of the MS data for the product of mesoheme turnover, "mesoanaerobilin". Mesoanaerobilin has a $[M+H]^+$ of 583 m/z (Figure 2.5, Panel B), which corresponds to the difference in ethyl groups on the 3 and 8 positions of the porphyrin ring compared to deuteroheme. The [A+1] peak for mesoanaerobilin was approximately 38% of the parent ion and is consistent with a 35-carbon molecule.

When [^{13}C-methyl]-SAM was utilized in the assay and the isolated product exhibited an enrichment of ^{13}C with a dominant $[M+H]^+$ of 528 m/z (Figure 2.6, Panel A, Spectra ii.). This observation provides evidence that ChuW transfers a methyl group to the product from the SAM moiety. To further assess the mechanism of methyl transfer, we utilized [d_3-methyl]-SAM in the ChuW assay. The use of the deuterium-labeled SAM molecule resulted in a DAB mass shifted by two units yielding a primary peak of 529.28 m/z (Figure 2.6, Panel A, Spectra iii.), thereby confirming the transfer of only two deuterium atoms from the SAM-derived methyl group. The use of [d_3-methyl]-SAM in the assay resulted in a kinetic isotope effect (KIE) of 2.3 based on specific activities.

To investigate the state of the pyrrolic ring system of the product, we acquired the fragmentation pattern of DAB (Figure 2.6, Panel B). The MS/MS revealed multiple fragments consistent with the cleavage of the macrocycle. Upon fragmentation of ^{13}C-methylated DAB, some of these fragments also shift by one mass unit, indicating the retention of the isotopic label (Figure 2.6, Panel C). This fragmentation profile was observed when performing a similar MS analysis of the product from mesoheme turnover, "mesoanaerobilin" (Figure 2.5, Panel C). These data are in stark contrast to fragmentation typically observed for closed porphyrin ring systems, which only result in the cleavage of substituents surrounding the ring and suggested opening of the porphyrin ring. This conclusion is also supported by the increase in labile iron (Figure 2.3). A proposed fragmentation pathway was constructed based on the predicted structure of DAB (Figure 2.7).

We further probed the mechanism by which ChuW transfers the SAM-methyl group using NSI-MS to analyze HPLC-isolated 5'-dA when employing [d_3-methyl]-SAM in the assay (Figure 2.8). The [A+1] peak increased for 5'-dA from 11% to 60% (Figure 2.8, compare trace i and ii, respectively). This is consistent with what has been reported for other RSMTs and indicates the 5'-dA•, generated on one SAM molecule, abstracts a hydrogen atom from the methyl group originating from another SAM molecule. In addition to the ChuW sequence similarities between HemN and other class C RSMTs, these data suggest the presence of

two distinct SAM binding sites. This is consistent with the proposed HemN mechanism and what has already been confirmed for some RSMTs.

Since lyase reactions may require proton transfer or incorporation, we performed the assay in buffered $^{2}H_2O$ (70%) using deuteroheme as the substrate in order to determine if a solvent-derived proton is incorporated into DAB. Upon purification in methanol, NSI-MS of DAB resulted in a 43% increase in the [A+1] peak to the parent ion (Figure 2.9, compare traces i and ii). This signal was retained after incubation with methanol for 24 hours suggesting that a deuteron is incorporated during the reaction and originates from solvent. Similarly, the number of exchangeable hydrogens that are present on the product was determined by analyzing isolated DAB in d_4-methanol. NSI-MS analysis resulted in a Gaussian distributed signal centered at 531 m/z (Figure 2.9, Trace iii).

ChuY uses anaerobilin as a substrate. In order to further examine the putative role of ChuW in an anaerobic heme degradation pathway, we characterized ChuY, the protein that is expressed downstream from ChuW in the heme uptake operon. The current function for ChuY is annotated as an NAD(P)H oxidoreductase, so we performed activity assays of ChuY in the presence of NADPH and isolated DAB. Upon addition of enzyme into the assay mixture, we observe the decrease in the UV-visible features of DAB with respect to time (Supplemental Figure 2.10). Increasing the amount of ChuY present in the assay resulted in the linear increase of activity, indicating an enzyme-catalyzed reaction.

2.3 Discussion

In this investigation, we present evidence for oxygen-independent heme degradation using isotope labeling, activity assays, and mass spectrometry in order to gain insight into the reaction catalyzed by recombinant ChuW from enterohemorrhagic *E. coli* (Figure 2.11). Our data suggests ChuW belongs in the class C radical SAM methyltransferase (RSMT) enzyme family based on the domain structure, sequence analysis, and similar mechanisms for methylation that have been reported for these enzymes[148]. These enzymes share similiarites with HemN of having two predicted SAM binding sites within the active site, which has caused missannotations of these genes. However, distinction between genes is coming to light[118]. Bioinformatic analyses have identified over 300 similar sequences across 36 genera within the Structure-Function Linkage Database (SFLD)[94], all from organisms which do not encode a HO. Some ”primitive” purple non-sulfur bacteria that thrive in anaerobic environments also contain a *chuW*, such as *Denitrovibrio* and *Desulfurispirillum*. Evolutionarily speaking, it is interesting that two distinct enzymes, HemN and ChuW

(HutW in *V. cholerae*), contain a similar functional domain yet one enzyme is responsible for the anaerobic formation of heme while the other enzyme can catalyze the degradation.

The current mechanistic paradigm for all heme oxygenases reported to date involves activation of molecular oxygen. In stark contrast, the data presented herein suggests ChuW utilizes the oxidizing power of the 5'-dA radical in order to catalyze methyl transfer and rearrangement of the porphyrin ring, resulting in the liberation of iron. Clues to the ChuW mechanism come from what has been recently observed for other class C RSMTs. Indeed, all known class C RSMTs catalyze methylation of sp^2-hybridized carbon atoms that, in some cases, leads to considerable structural rearrangement[148,150,175,198]. While ChuW/HutWs appear to be evolutionarily distinct (Figure 2.2 and 2.12) when compared to other RSMTs or HemN, all of these enzymes have been shown to utilize the reductive cleavage of SAM as the starting point in their catalytic cycle. In addition, activation of the substrate or the methyl group of one SAM moiety by reductive cleavage of another SAM molecule has already been postulated for several RSMTs[148]. Building upon our observations and these postulated mechanisms, Figure 2.11 depicts the proposed reaction scheme for the ChuW-dependent decyclization of deuteroheme. Although the complete mechanism is unclear, our data indicate that after generation of the 5'-dA•, this radical abstracts a hydrogen atom from the methyl group that originated from a second SAM molecule. This methylene radical likely attacks the substrate by radical addition directly before causing a rearrangement of the porphyrin ring. However, we recognize that there are other possible structures that could satisfy this goal and our MS data (Figure 2.13) and is under further investigation.

Several intermediates can be considered that are based on the for other class C RSMTs. Of particular interest are the products of some class C RSMTs that have been shown to contain other "high energy" C1-derived moieties, such as cyclopropane rings[175,198]. Such a moiety would be unstable if placed across the 4-5 or 5-6 carbon-carbon bond of deuteroheme, or heme, and would provide structural reasoning for any of the products presented depending on resolution of the cyclopropane ring cleavage (Figures 2.11 and 2.13). Similar to what has been described for the class C RSMTs YtkT and Jaw5[175], whether or not such a mechanism involves radical addition or nucleophilic attack by the methylene radical or ylide, respectively, is also not clear. Either mechanism for methyl transfer and ring opening requires an additional electron, a problem discussed in a recent review[148], but that is still unresolved for these class C RSMTs.

The fragmentation pattern that we observe for DAB is particularly useful in that cleavage at the central bridging methine carbon produces a pyrrolium ion $[M+H]^+$ at 271 and a pyrrolic ion $[M^+]$ at 257 m/z (Figure 2.7), which is similar to what has been observed in the mass spectral analysis of biliverdin[199]. To this end, we

compared structures that coincided with ring cleavage at either the α or γ methine bridge while accounting for the addition of a methyl group at or near the cleavage site. The resulting even mass fragments suggest a loss of one nitrogen atom and are best explained by fragmentation at either the β or δ methine bridges. It is unclear if there is a preference for which methine bridging carbon-carbon bond is ultimately broken (C4-C5 or C5-C6) during catalysis. In the case of the proposed structure for DAB, both outcomes are possible (Figure 2.11). Although our observations for MS/MS analysis of deuteroanaerobilin are explained by the proposed structure (Figures 2.9 and 2.11), other feasible isomers are described in Figure 2.13 that cannot be ruled out at this time. Due to the photolability and oxygen sensitivity of deuteroanaerobilin, efforts to isolate these compounds to a purity sufficient for NMR analysis has proven challenging.

Heme has limited solublility in aqueous solution, therefore the standard protocol for assaying HOs is to load the enzyme with 1:1 equivalents of heme:protein followed by initiating turnover with cytochrome P450 reductase and near stoichiometric amounts NADPH. This amounts to what is essentially a single turnover reaction that is often slow, and that can be the result of non-enzymatic coupled oxidation when catalase is not present in the assay[10]. Thus, making the identification of genuine HOs all the more difficult. ChuS from *E. coli* O157:H7 was originally identified as a HO[8]. However, a later report from the same group revealed a significantly decreased activity in the presence of catalase[67]. Similarly, the heme utilization protein HutZ from *V. cholerae* was described as a HO based on spectroscopic assays[200], but there was no indication that catalase or superoxide dismutase was included in the assay reported for the initial characterization, the products were never identified, nor was this activity observed by others[9]. Consequently, the benefit of studying an anaerobic heme-degrading enzyme *in vitro* is the minimal risk of non-enzymatic coupled oxidation artifacts. However, if ChuS and HutZ were bona fide heme degraders, this would allow enterohemorrhagic *E. coli* and *Vibrio cholerae* the ability to acquire iron from heme in varying oxygenic environments.

The existence of an anaerobic mechanism for heme degradation is consistent with i) the recent revelations in the heme biosynthetic pathways[118,201], ii) the characterization of radical SAM enzymes involved in catalyzing important steps in the anaerobic biosynthesis of protoheme[121,195], and iii) recent observations that heme degradation has evolved to suit the physiological needs of the organism[54]. In fact, the presence of radical-based enzyme reactions is well established in the central metabolic pathways required for anaerobic growth in bacteria[202,203]. Our *in vitro* data suggest that ChuW functions as a RSMT that methylates heme as part of a decyclization mechanism resulting in an open tetrapyrrole and the release of the essential nutrient, iron (Figure 2.11). Many of our observations overlap with what has been published for the class C RSMTs. Future studies will focus on the complete characterization of the tetrapyrrole products of both ChuW and

ChuY.

2.4 Materials and Methods

Chemicals- Porphyrins were a were purchased from Frontier Scientific with the exception of hemin chloride, which was purchased from Sigma Chemical Company. S-adenosylmethionine (SAM) HCl, 5'-deoxyadenosine, and S-adenosylhomocysteine were also purchased from Sigma. Buffer components were purchased from Fischer Scientific.

Iron analysis of purified ChuW- Iron quantitation of ChuW was performed as previously described[204]. Iron standards were prepared in acid washed glassware at a concentration of 0.5 mM ferrous ammonium sulfate heptahydrate and diluted to various concentrations between 0.012 mM to 0.2 mM to a final volume of 250 µL with identical buffers (20 mM Tris pH 8.0, 300 mM KCl, and 10% glycerol). After acid precipitation and heat incubation at 80℃, 750 µL of dH_2O was added and then precipitates pelleted by centrifugation. 750 µL of each solution was transferred to a new microcentrifuge tube, where 50 µL of 10% hydroxylamine and 250 µL of 0.1% bathophenanthroline were added with vortexing between additions. Samples were incubated at room temperature for one hour and measured at 535 nm following the incubation period. ChuW samples were prepared in the same manner with triplicate measurements per concentration tested, while independent experiments were performed in triplicate, as well.

EPR Spectroscopy of Purified ChuW- Samples were prepared by diluting ChuW to a final concentration of 400 µM either in the presence or absence of 2 mM sodium dithionite. Spectra are a result of 3 scans recorded at 10 K with 1 milliwatt microwave power, modulation frequency of 100 kHz, and modulation amplitude of 6.477 G.

High-performance liquid chromatography of S-adenosylmethionine cleavage by ChuW- Single turnover assays were performed in 2 mL reaction volumes with a final concentration of 1 mM SAM, 100 µM deuteroheme, 100 µM ChuW, and 2 mM sodium dithionite in a 20 mM Tris pH 8.1, 125 mM KCl, and 10% glycerol buffer. Controls were run in side-by-side reactions in the absence of either deuteroheme or sodium dithionite. 90 µL aliquots were subjected to acid precipitation with 50 µL of 1% TFA at 0, 0.5, 1, 3, 5 and 10 minutes. Samples were centrifuged and the supernatant was applied to a Denali C18 HPLC column (15 cm x 4.6 mm, 5 µm). Cleavage products were separated by a gradient of acetonitrile 0-80% in 0.1% TFA at a flow rate of 1 mL/min. When using NADPH, flavodoxin, and flavodoxin reductase, the flow rate was lowered to 0.8 mL/min. All HPLC assays were monitored at 260 nm and quantitation of 5'-dA and SAH were performed

by comparing the peak areas to a standard curve. To confirm the deuteron transfer from (d_3-methyl) SAM, 5'-dA was collected by manual fractionation and subjected to vacuum centrifugation. Mass spectrometry was performed on the collected fractions by direct infusion. Details of the instrument used and the conditions are described below.

Monitoring ChuW activity by UV-vis spectroscopy- All UV-visible spectra were recorded on an Agilent 8A53 diode array spectrophotometer using a Peltier temperature controller set to 25℃. Typical enzyme assays were conducted anaerobically with degassed buffer containing 5% DMSO, 1 µM ChuW, 5 µM EcFldA, 2 µM EcFpr, 250 µM NADPH, and 10 µM of either hemin or deuteroheme. Reactions were initiated by the addition of SAM to a final concentration of 250 µM. Spectra were taken from 350 nm to 900 nm every 2 minutes for 30 minutes. Extinction coefficients of DAB and anaerobilin were determined by the isosbestic point at 418 nm using the following relationship:

$$A = l\epsilon(C_{substrate} + C_{product}) \tag{2.1}$$

Mass spectrometry of reaction products- Deuteroanaerobilin and mesoanaerobilin were purified by separation of small molecules on a C1 sep pack attained from Silicycle. In short, a 5 mL reaction mixture containing 100 µM deuteroheme or mesoheme, 20 µM ChuW, 400 µM SAM, 500 µM NADPH, 20 µM EcFld and 5 µM EcFpr was incubated anaerobically for 4 hours at room temperature and in the dark. The assay mixture was applied to the sep pack pre-equilibrated with 1 eq of methanol, 1 eq of dH_2O, and 1 eq of assay buffer. Once the assay mixture ran through the column, it was washed with 1 eq of buffer, 2 eq. of water, 1 eq of 1% TFA, and 3 eq of water, before elution in 100% methanol. The eluent was diluted in methanol and analyzed using nanospray ionization mass spectrometry (NSI-MS) by direct infusion into a linear ion trap mass spectrometer (LTQ-Orbitrap Discovery; Thermo Fisher Scientific) using a nanoelectrospray source at a syringe flow rate of 0.40 µL/min and capillary temperature set to 210℃. Fragmentation by collision-induced dissociation (CID) in MS/MS and MSn was used with normalized collision energy of 35-40%. Automated acquisition of MS2 fragmentation was achieved using the total ion mapping (TIM) functionality of the Xcalibur software package (version 2.0, Thermo Fisher Scientific). Identical assays were performed with labeled S-adenosylmethionine substrate prepared as previously described[138].

High-performance liquid chromatography of isolated deuteroanaerobilin- Detection of deuteroanaerobilin isolated was performed using a SAS-Hypersil C1 column (150 x 4.6 mm) from Thermo scientific equipped with a 1 mL pre-column and monitoring at 400 nm. Isolated DAB solubilized in 100% methanol was manually

injected (20 µL). Separation was carried out using 100% methanol (Solvent A) and 1M ammonium acetate-acetic acid buffer (pH 4.6) (Solvent B) using a flow rate of 1.0 mL/min. Elution was achieved by applying a linear gradient starting with 62% solvent A and increasing to 80% by 20 minutes. The column was washed for 10 minutes with 80% solvent A before starting the next sample. The elution of DAB was compared to deuteroheme based on retention times.

Expression, purification, and enzymatic assay of ChuY- ChuY was expressed by growing the *E. coli* strain BL21 DE3 strain containing an IPTG inducible expression plasmid that carried the gene coding for ChuY with a 6xHis tag (pET15a). In short, a 20 mL starter culture was grown for 6 hours before inoculating six 1 L flasks containing TB media. Cultures were grown at 37℃ shaking at 200 rpm until the O.D. at 600 nm reached 0.8. IPTG was added to a final concentration of 500 µM. Cultures were incubated at 18℃ overnight shaking at 200 rpm and harvested by centrifugation before being stored at -80℃. The frozen cell pellets were solubilized in buffer containing 20 mM Tris pH 8.1, 300 mM KCL, and 10% glycerol with trace amounts of PMSF, lysozyme, and DNase. Cells were lysed by French pressure cell and lysate was ultracentrifuged at 65,000 x g for 1.5 hours. The supernatant was applied to Talon resin, washed with 2 column eq of water, and 8 column eq of solubilization buffer. After washing the column with 3 column eq of 10 mM imidazole, ChuY was eluted with buffer containing 250 mM imidazole. Fractions containing ChuY were pooled, buffer exchanged to remove imidazole, and then concentrated. Protein content was analyzed by SDS-PAGE and Biuret analyses before freezing aliquots at -80℃.

Monitoring activity of ChuY by UV-visible spectroscopy- All UV-visible spectra were recorded on an Agilent 8A53 diode array spectrophotometer using a Peltier temperature controller set to 25℃. Typical enzyme assays were conducted anaerobically with degassed buffer containing 250 µM NADPH and 20 µM of isolated deuteroanaerobilin. Reactions were initiated by the addition of ChuY to 1 µM. Spectra were taken from 350 nm to 900 nm every 2 minutes for 10 minutes. The activity was monitored by the disappearance of the 780 nm feature of DAB and was converted to concentration by the extinction coefficient for DAB.

2.5 Figures and Tables

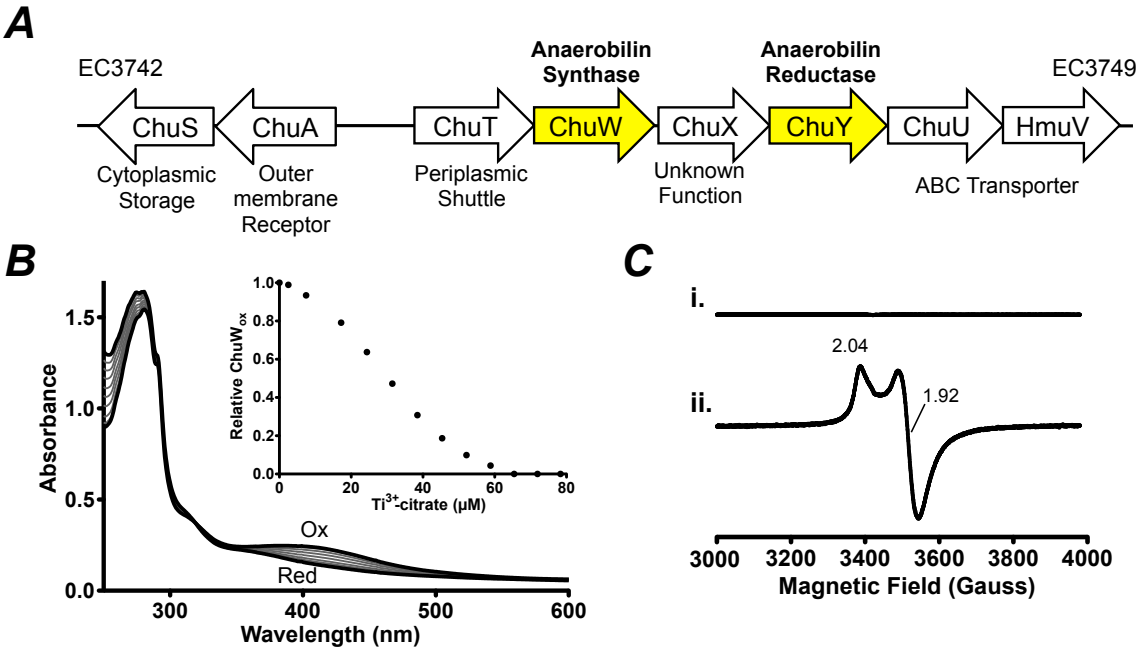

Figure 2.1: Genetic organization of the heme utilization operon in *Escherichia coli* O157:H7 and characterization of the Fe-S cluster coordinated by ChuW. *(Panel A)* ChuW is genetically adjacent to the heme uptake machinery that is expressed during iron starvation. *(Panel B)* UV-visible spectra of isolated ChuW and reduction of the Fe-S cluster. Scans were recorded after injecting with equivalents of Ti^{3+}citrate. *(Inset)* The percentage of oxidized ChuW based on the change in the absorption at 400 nm plotted with respect to the concentration of Ti^{3+}citrate added. *(Panel C)* EPR spectra of ChuW in the absence and presence of 1mM sodium dithionite (top and bottom trace, respectively) Spectra are a result of 3 scans recorded at 10 K with 1 milliwatt microwave power, a modulation frequency of 100 kHz, and modulation amplitude of 6.477 G.

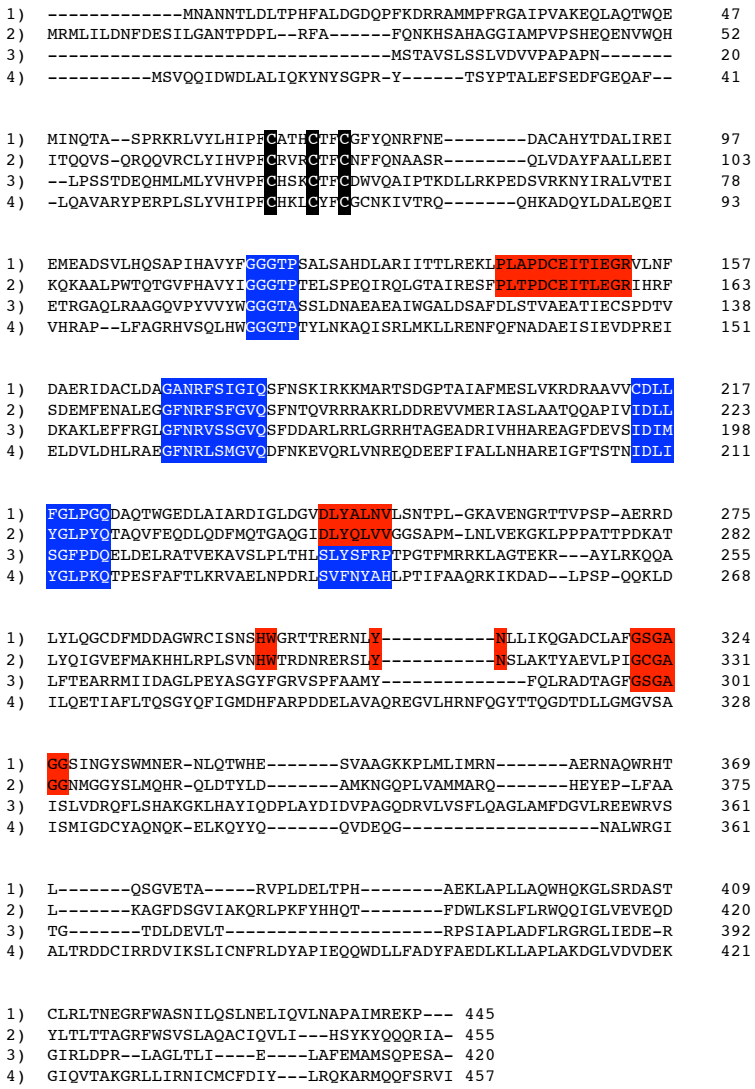

Figure 2.2: Multiple sequence alignment of ChuW. *E. coli* ChuW (1) was aligned with *V. cholerae* HutW (2), *S. actuosus* NocN (3), and *E. coli* HemN (4). Sequences highlighted in red represent motifs specific to ChuW/HutW homologues, whereas sequences in blue are homologous in all proteins presented. Black highlighted residues are conserved cysteines in the radical SAM CxxxCxxC motif.

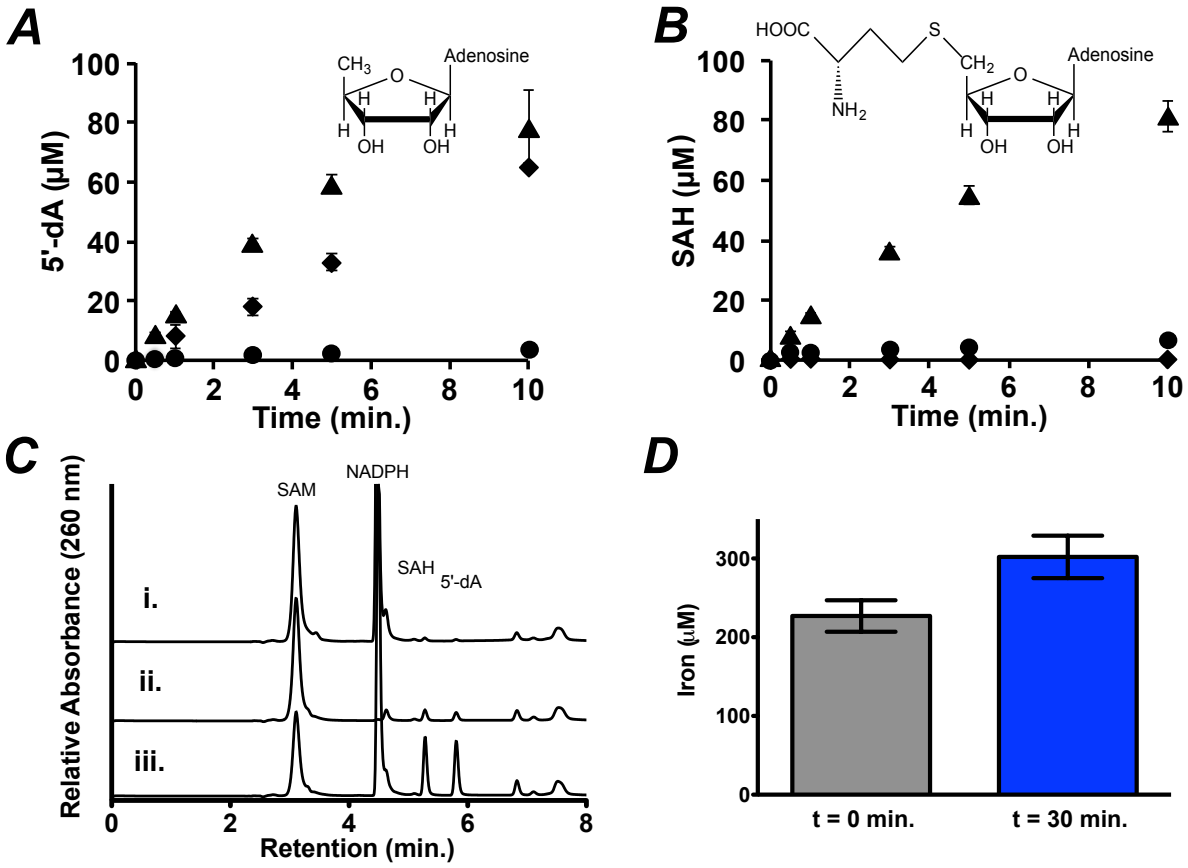

Figure 2.3: Quantification of 5'-deoxyadenosine, S-adenosylhomocysteine (SAH) and iron produced during the ChuW reaction. Separation and quantification of 5'-deoxyadenosine (5'-dA) and S-adenosylhomocysteine (SAH) using HPLC was performed as described in the "Materials and Methods". In the absence of sodium dithionite *(circles)*, no SAH or 5'-dA were produced *(compare Panels A and B)*, however, in the absence of only deuteroheme *(diamonds)* 5'-dA was still produced in a linear manner whereas SAH was not detected *(compare Panels A and B)*. In the presence of deuteroheme *(triangles)* SAH and 5'-dA were both produced in a 1:1 ratio *(compare Panels A and B)*. Products were quantified using a standard curve and assays were performed in triplicate. *(Panel C)* HPLC traces showing the results of a 20 minute assay using the physiological electron donor system flavodoxin, NADPH/flavodoxin reductase in the absence of NADPH (trace i), the absence of heme *(trace ii)* or with the complete assay mix *(trace iii.)*. *(Panel D)* Total labile iron present in the ChuW assay at the start of the reaction and after 30 minutes.

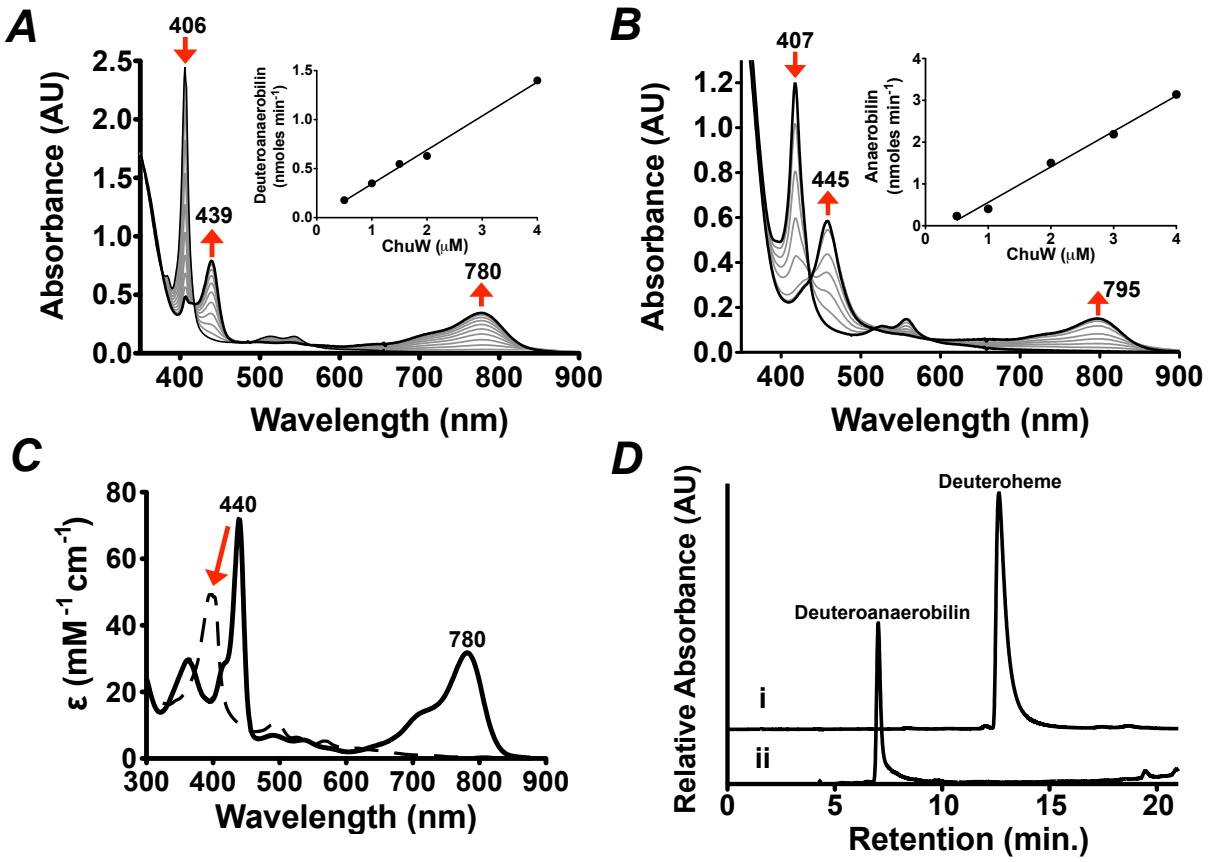

Figure 2.4: Characterization of anaerobic ChuW-dependent heme degradation by UV-visible spectroscopy. UV-visible spectroscopic assays were performed by adding ChuW (2 μM) to a solution containing 10 μM deuteroheme *(Panel A)* or heme *(Panel B)*, respectively, as well as the EcFld/EcFpr electron donor system (5 μM and 2 μM, respectively) with 200 μM NADPH. Assays were initiated by the addition of SAM (250 μM) and spectra were recorded every 2 minutes over the course of 30 minutes. The red arrows indicate the direction of spectral changes during the course of the experiment. The insets show a plot of the product formation rate at various ChuW concentrations. *(Panel C)* The UV-visible spectrum of isolated deuteroanaerobilin in methanol resulted in similar spectroscopic features observed in the enzyme assay *(solid spectra)*, while exposure to sunlight resulted in significant changes to the spectra *(dashed line)*. *(Panel D)* HPLC isolation of the deuteroheme substrate and the product of ChuW turnover, herein termed ”deuteroanaerobilin”.

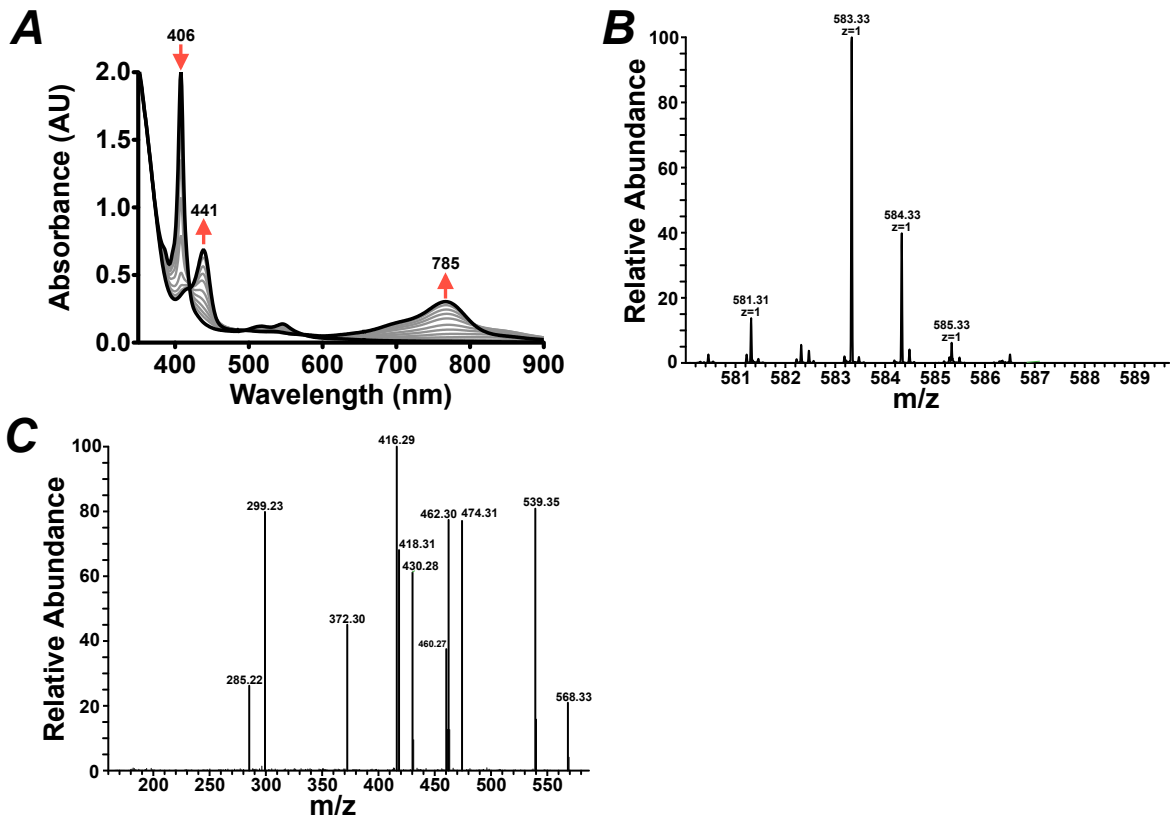

Figure 2.5: *(Panel A)* Spectroscopic assay utilizing mesoheme as a substrate, *(Panel B)* full MS spectra of the isolated mesoanaerobilin product acquired by direct infusion on an LTQ-Orbitrap mass spectrometer and *(Panel C)* MS/MS of the 583.33 peak acquired in Panel B.

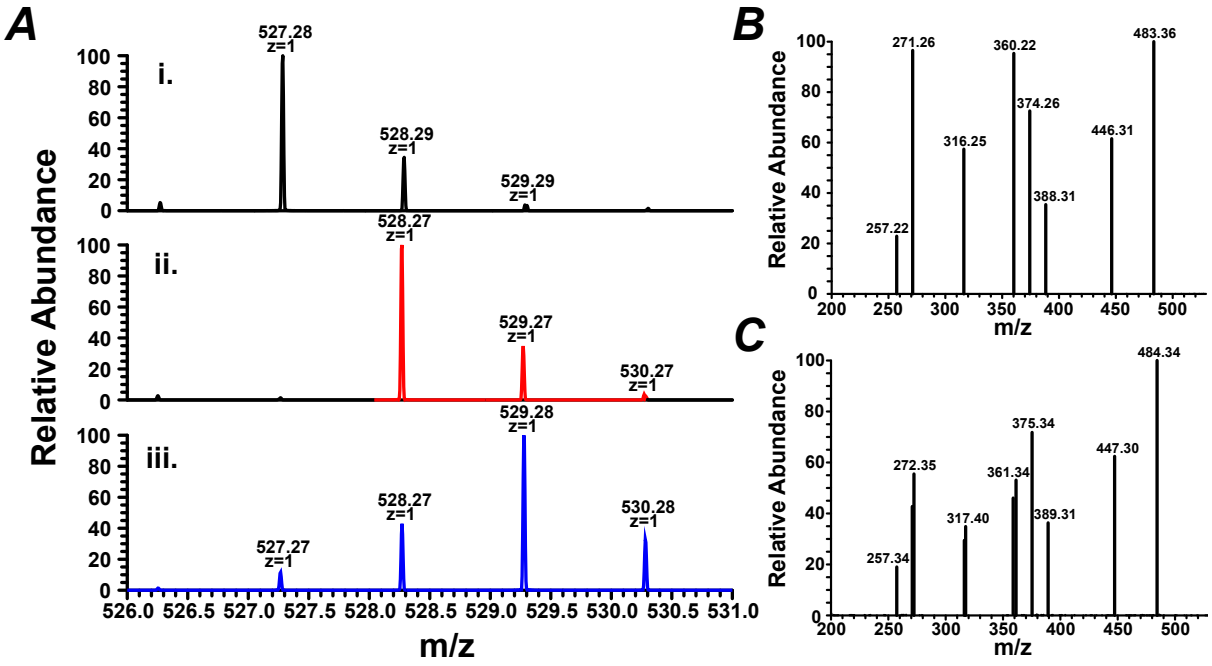

Figure 2.6: Mass spectroscopy (MS) of isolated deuteroanaerobilin. *(Panel A)* NSI-MS of deuteroanaerobilin was performed as described in the "Materials and Methods" using deuteroheme and i) (^{12}C-methyl) SAM, ii) (^{13}C-methyl) SAM, or iii) (d_3-methyl) SAM as substrates. *(Panel B and C)* The MS/MS of deuteroanaerobilin or ^{13}C-methylated deuteroanaerobilin revealed multiple fragments when using CID at 40%. Predicted fragment structures are shown in Figure 2.7.

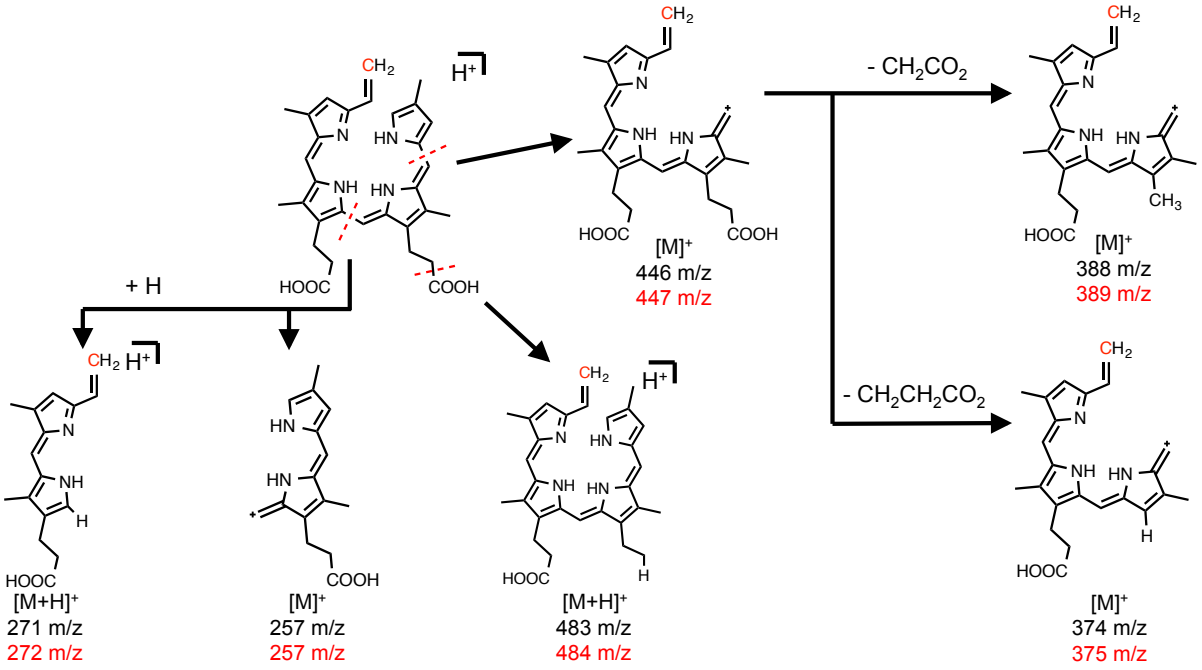

Figure 2.7: Proposed structures for observed MS/MS peaks of deuteroanaerobilin.

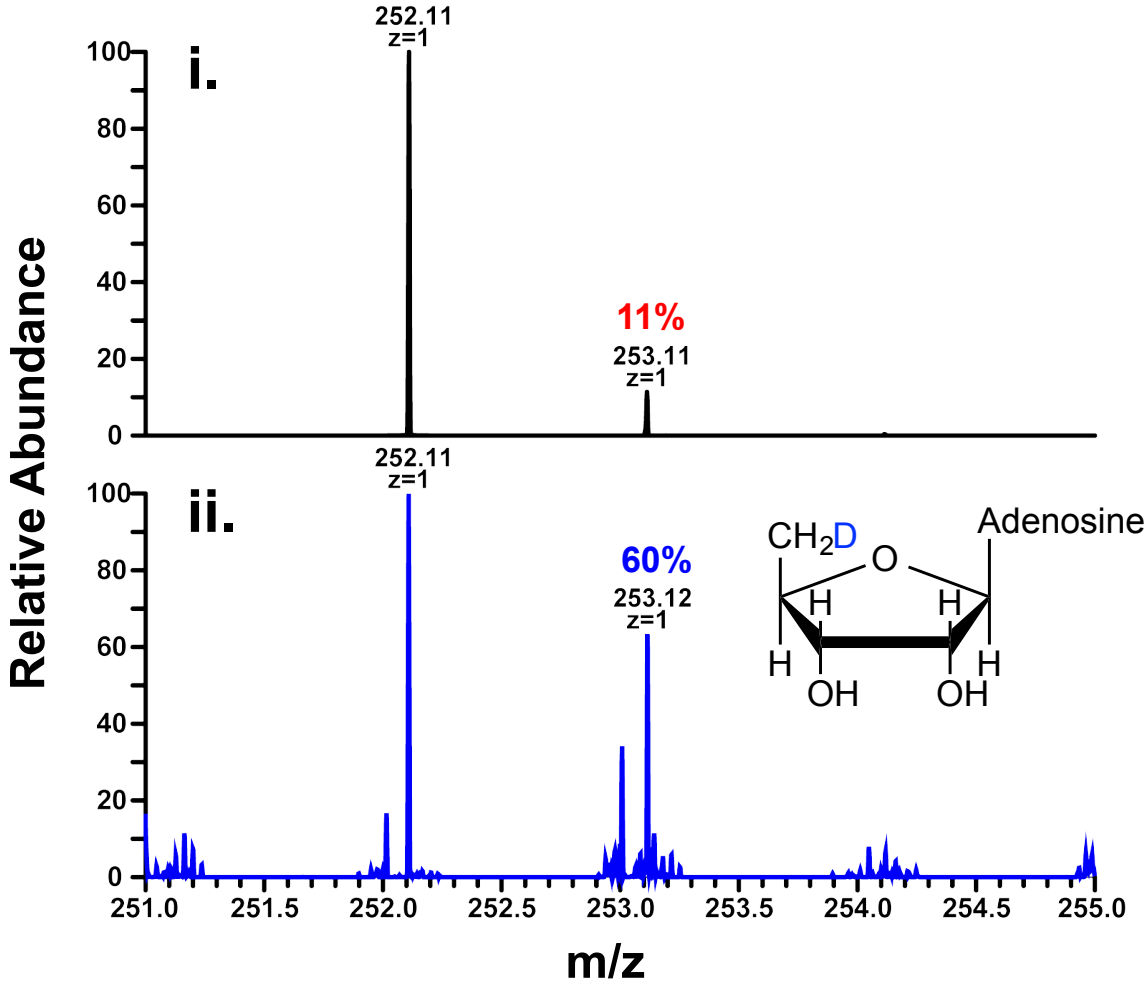

Figure 2.8: NSI-MS of 5'-dA. i) 5'-dA standard was analyzed by NSI-MS with a $[M+H]^+$ of 252.11 m/z. ii.) 5'-dA was isolated by HPLC post ChuW turnover using (d_3-methyl) SAM and resulted in a 49% increase in the A+1 peak at 253.12 m/z.

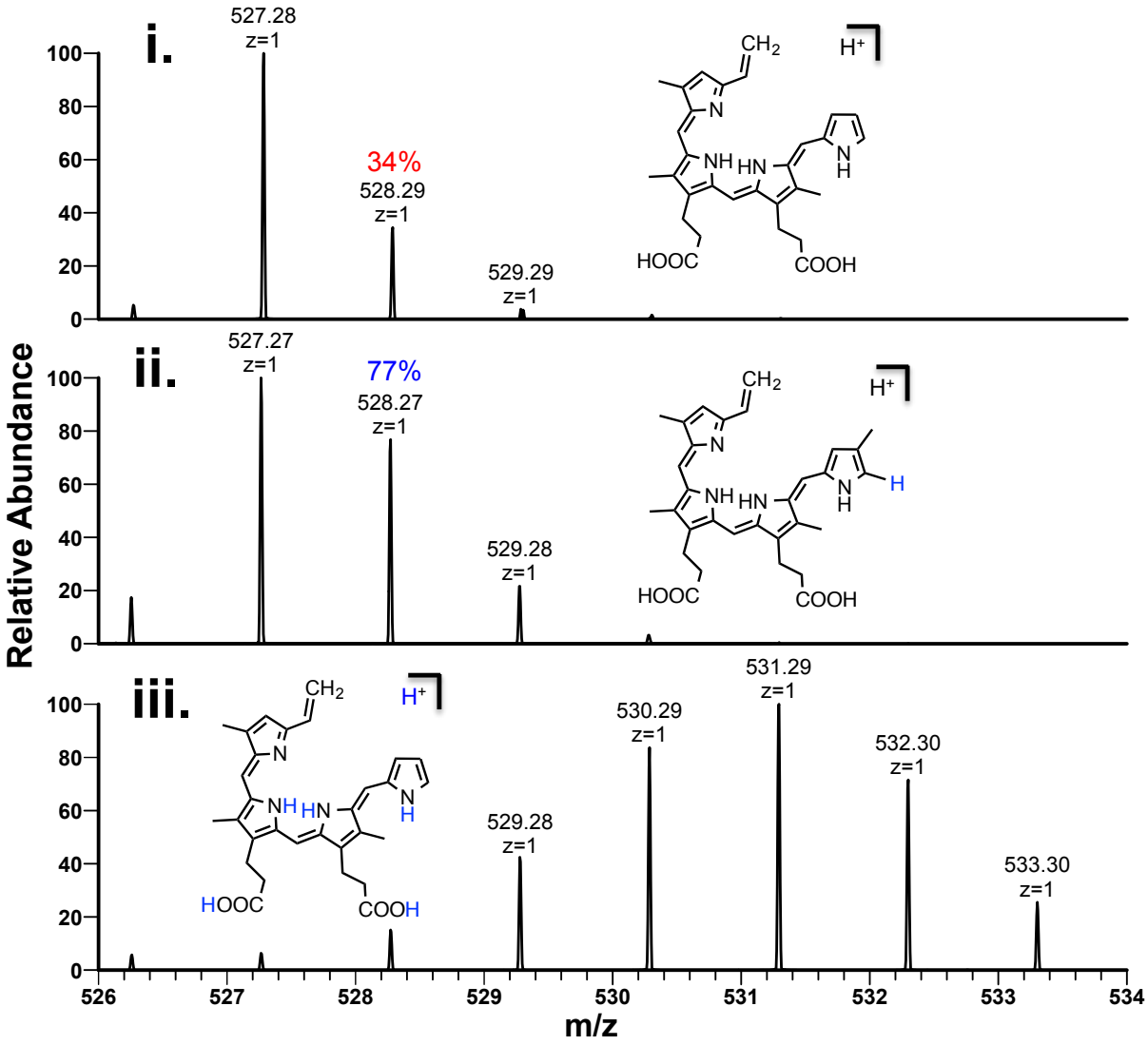

Figure 2.9: Mass spectrometry of solvent-derived deuterium incorporation into deuteroanaerobilin. ChuW was assayed in buffered H_2O and 70% buffered ^2H_2O (i and ii, respectively). Deuteroanaerobilin was isolated as described in the "Materials and Methods" and analyzed by NSI-MS. When assayed in buffered ^2H_2O, we observed a 43% enrichment of the A+1 peak at 528.27 m/z for the product (ii). NSI-MS of isolated deuteroanaerobilin in d_4-methanol (iii).

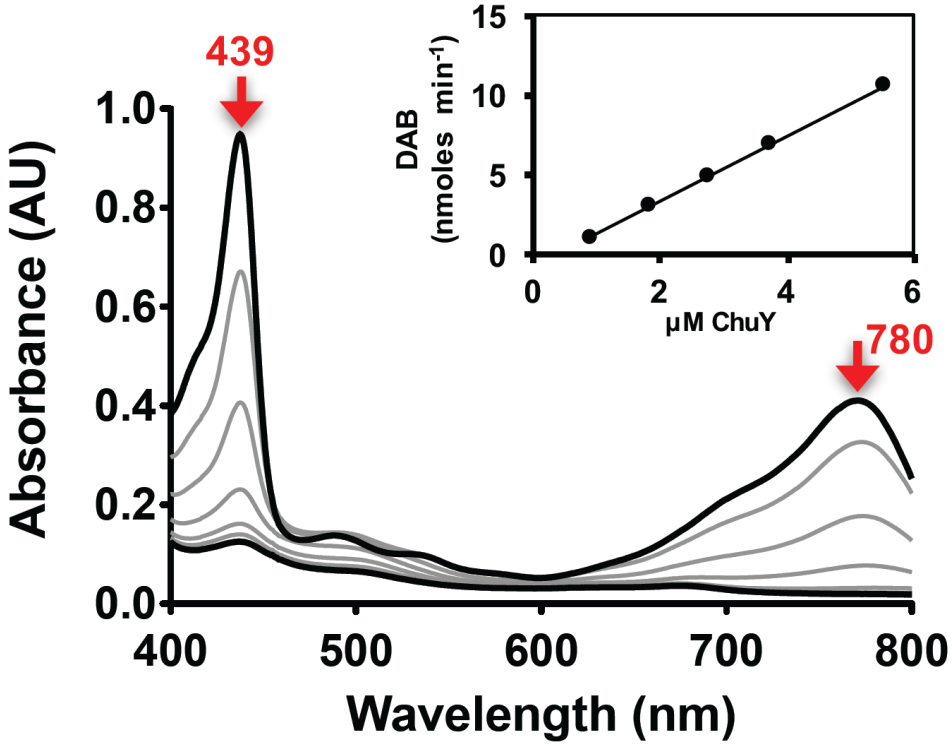

Figure 2.10: NADPH-dependent turnover of deuteroanaerobilin (DAB) by purified ChuY monitored by UV-visible spectroscopy. The arrows indicate the direction of spectroscopic changes during the time course of the assay. *Inset*; rate of DAB consumption at various ChuY concentration.

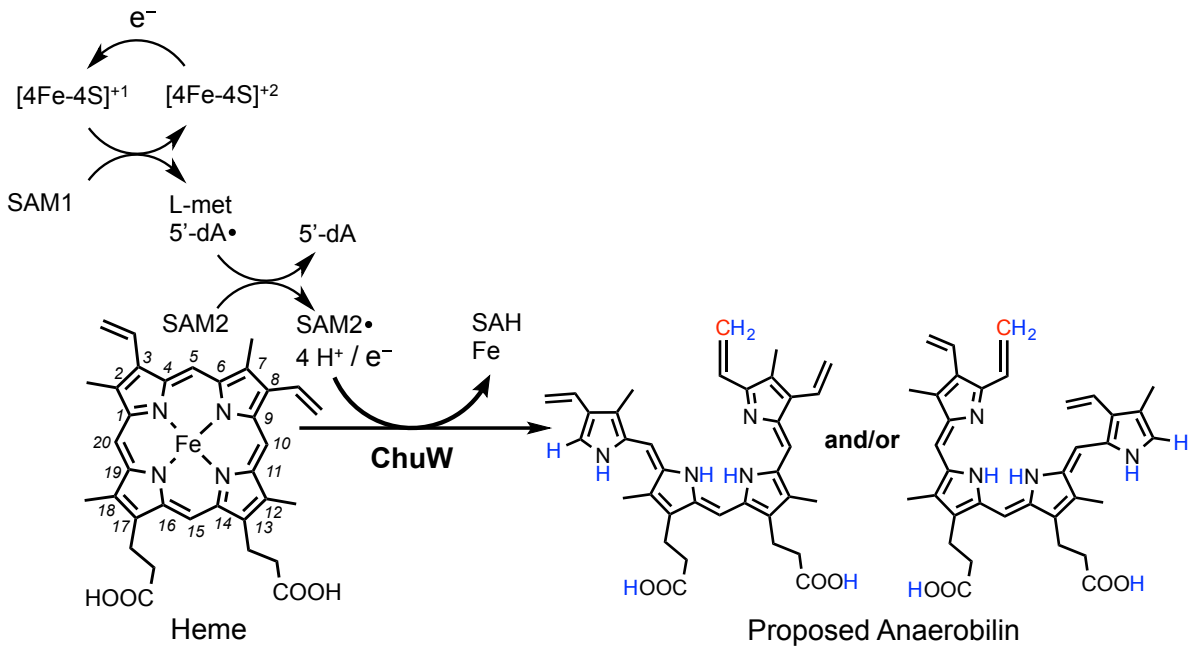

Figure 2.11: Proposed products and reaction scheme for ChuW. Predicted hydrogens observed by deuterium incorporation are labeled in blue and the SAM-methyl group transferred in red.

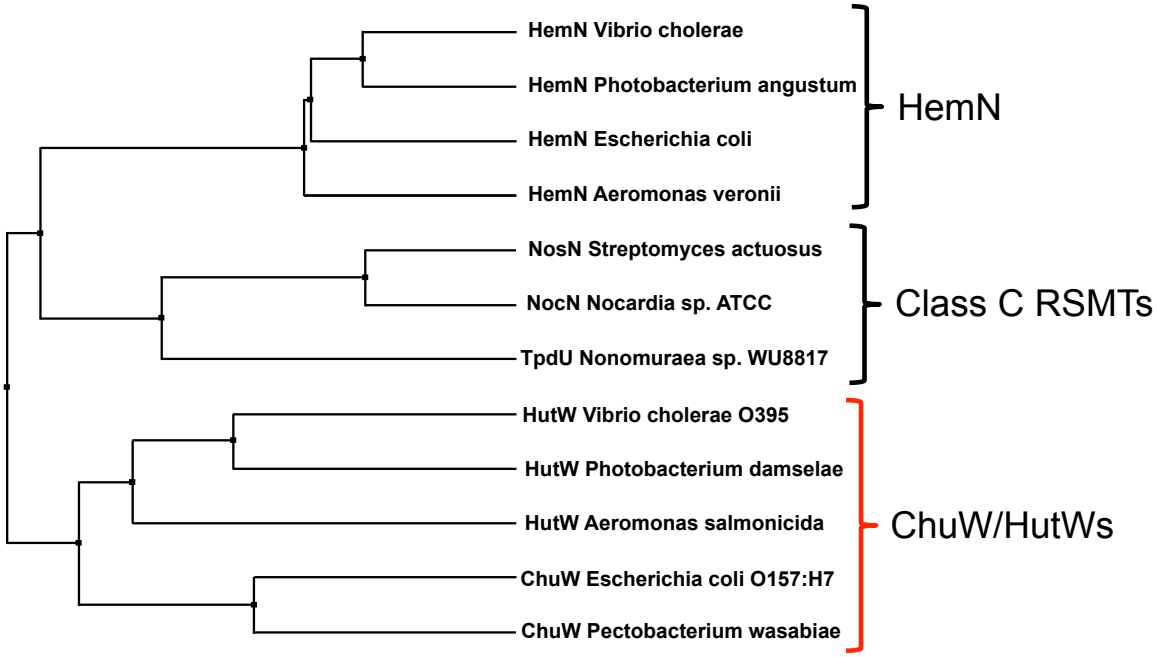

Figure 2.12: Phylogenetic comparison of HemN, class C RSMTs, and ChuW/HutW. The phylogenetic tree was generated by Jalview[205] from a sequence alignment based on % identity.

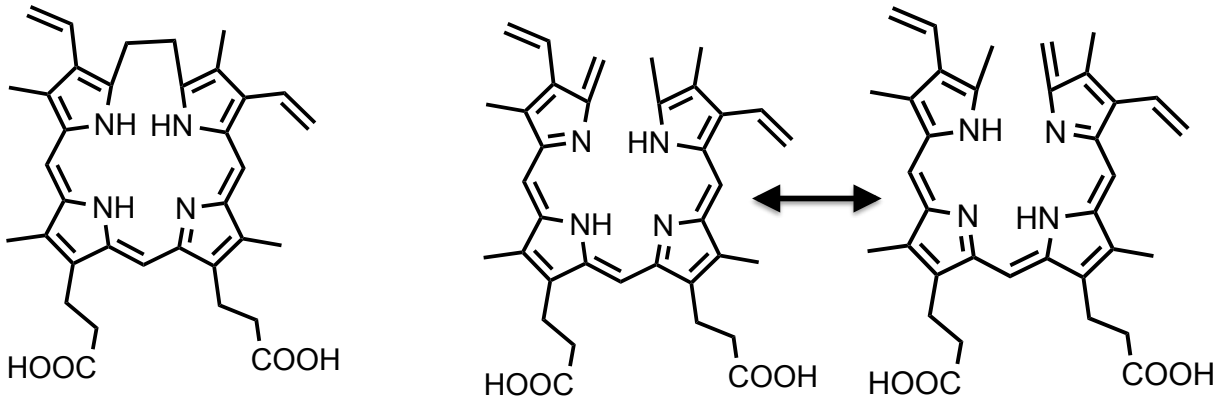

Figure 2.13: Alternative structures for anaerobilin that are consistent with the MS data obtained for deutero- and mesoanaerobilin.

CHAPTER 3

CHUY IS AN ANAEROBILIN REDUCTASE THAT EXHIBITS KINETIC COOPERATIVITY[1]

[1] **Joseph W. LaMattina**, David B. Nix, Anudeep R. Neelam, Kate G. Uy, Michael DelRossi, and William N. Lanzilotta. To be submitted to the Journal of Biochemistry

Abstract

Heme catabolism is an important biochemical process many bacterial pathogens utilize to acquire iron. However, tetrapyrrole catabolites often require further processing for their removal from the cell as a means to prevent toxicity. In previous work, we have presented *in vitro* evidence for an anaerobic heme degradation pathway in *Escherichia coli* O157:H7. In this system, the radical SAM enzyme ChuW transfers a methyl group to heme by a radical-mediated mechanism that causes the alteration with ring opening of porphyrin macrocycle, iron release, and the production of a new linear tetrapyrrole termed ”anaerobilin”. Here, we describe the structure and function of ChuY, the enzyme expressed downstream from ChuW in the same heme utilization operon. ChuY has structural similarities to biliverdin reductase and forms a dimeric complex and reduces anaerobilin to the product we have termed anaerorubin. Steady state analysis suggests ChuY exhibits kinetic cooperativity, which is best explained by a random addition mechanism with a kinetically preferred path for NADPH binding.

3.1 Introduction

Iron is an essential nutrient pathogenic bacteria must acquire during infection to ensure their survival in a mammalian host. The ability to acquire iron, either directly or from iron-protoporphyrin IX, contributes to the virulence and pathogenesis of the organism[5]. With tight regulation of iron transport and storage in eukaryotes, scavenging heme from the host and degrading it to acquire cellular iron is one mechanism microorganisms use to overcome this barrier[12,191]. The canonical pathway for enzymatic heme degradation is initiated by the conversion of heme to biliverdin IXα by heme oxygenase[22,23]. In eukaryotic systems, biliverdin is reduced at the γ-meso carbon by a biliverdin reductase prior to glucuronidation and removal from the cell[24]. Although, the entire canonical pathway is

not observed in proteobacteria, bacterial heme oxygenases have been identified[48,192,193]. In some of these microorganisms, the degradation products are used as precursors for the chromophore in phytochromes, which act as photosensors for light-dependent gene regulation[206–208]. Moreover, mechanisms must be in place to prevent accumulation of these catabolites to avoid cellular damage.

A heme oxygenase known for opening the porphyrin macrocycle has not been identified by BLAST searches or biochemical analysis for many enteric pathogens. Our previous work suggested that ChuW from *E. coli* O157:H7 is a radical SAM methyltransferase that degrades heme to a photoreactive tetrapyrrole termed ”anaerobilin” during the liberation of heme-iron[209]. Here, we report the structure and function of the downstream enzyme ChuY from enterohemorrhagic *E. coli* O157:H7 (EHEC). ChuY has structural homology to biliverdin reductase, but is void of BVR activity. Instead, activity assays and mass spectrometry analyses suggest the enzyme reduces anaerobilin to the linear tetrapyrrole we have termed ”anaerorubin”, consistent with a role in anaerobic heme degradation. Steady state analyses of ChuY suggests the enzyme exhibits kinetic cooperativity that is best explained by a random association model with a kinetically preferred path for NADPH binding prior to the tetrapyrrole.

3.2 Results

Crystal structure of apo-ChuY. ChuY is associated with the heme utilization operon and is downstream from *chuW* (Figure 3.1). The sequence of ChuY suggests its function as a NAD(P)H oxidoreductase based on bioinformatic annotation. The native crystal structure was solved to 2.0 Å resolution by molecular replacement using an NAD(P)H oxidoreductase from *Shigella flexneri* (PDB 3QVO) as the starting model. The asymmetric unit consists of two monomers related by a two-fold symmetry axis (Figure 3.2, Panel A). The core structure contains a Rossman fold with 7 beta sheets sandwiched by 3 alpha helices on each side. The surface representation of the fold reveals a large pocket that, presumably, binds the substrates. The majority of electron density is well-defined with the exception of a glycine-rich loop near the predicted location of NADPH binding. The B-factors also correspond to a flexible loop that may stabilize with NADPH bound. The F_o-F_c map suggested a molecule larger than water was bound to R27 and two water molecules. When phosphate was modeled in the density the thermal B-factors throughout the molecule averaged 40 Å^2 with subtle differences between the oxygen and phosphorous atom. Considering lithium sulfate was used as an additive in the crystallization condition, the density could also be modeled with sulfate with similar refinement statistics.

ChuY is a dimer in solution. The dimeric interaction is greatest in the non-crystallographic symmetry contact within the asymmetric unit. PISA analysis[210] calculated this dimer interface to be 672.9 Å^2 with a free energy of -8.8 kJ mol^{-1}. The interface is composed of hydrogen bonds and salt bridges with only 3 nonpolar residues from each monomer contributing to the interaction. Table 3.2 indicate specific residues involved in electrostatic interactions and residues buried in the interface. Despite the calculated surface area and free energy of dimerization, the free energy P-value associated with the interface specificity is 0.554 (values $<$0.5 represent a likely specific interaction) and

suggested a nonspecific interface interaction. In order to directly assess the oligomeric structure of ChuY, we performed sedimentation velocity analytical ultracentrifugation to determine the dominant species in solution (Figure 3.2, panel C). After comparing the predicted sedimentation coefficient calculated by HYDROPRO[211] (3.39 S) the observed coefficient value of 3.36 S confirms ChuY is a stable dimer in solution despite the appearance of a weak interface in the crystal structure. We do observe some tetrameric species at approximately 4.9 S, but the structure of ChuY did not provide evidence for a tetramer that was physiologically relevant and was only observed by crystallographic packing.

ChuY has structural homology to biliverdin IXβ reductases. ChuY belongs to the atypical short chain dehydrogenase (aSDR) protein family, which lack some of the conserved residues that make up the catalytic tetrad responsible for catalysis in the aldehyde NADPH oxidoreductases[179]. This classification makes it difficult to determine function based on the primary sequence. However, the sequence of ChuY suggests homology to biliverdin IXα β-reductase (BVβR). Thus, we aligned the backbone α-carbon atoms of the BVβR-NADP model (PDB 1HE3) with the native ChuY structure (PDB 5FFQ) (Figure 3.3, Panel A). When displaying only the $NADP^+$ molecule from the BVβR structure and the electrostatic representation of the ChuY model, we see positively charged surface residues that accomodate the orientation of the nicotinamide cofactor (Figure 3.3, Panel B). In fact, there is a lysine residue following two glycines that likely coordinates the 2'-phosphate of NADPH when bound. This may suggest that ChuY is in an open conformation in our crystallographic model.

Characterization of Deuteroanaerorubin. We isolated deuteroanaerorubin (DAR) and anaerorubin (AR) anaerobically in the dark to prevent any potential light or oxygen-driven modification of the tetrapyrrole, as has been observed for deuteroanaerobilin[209]. DAR had little absorption in the 400-800 nm visible range. We analyzed the molecule using mass spectrometry by direct infusion. The dominant mass peak was at 529 m/z with

an additional signal at 531 m/z (Figure 3.4, Panel A). Both masses are in agreement with a reduction of DAB; however, it is unclear if two subsequent reductions are occurring for the larger mass. To confirm ChuY also reduces anaerobilin, we performed MS of isolated anaerorubin, which resulted in only a 4 electron reduction of anaerobilin (Figure 3.5). This product is likely from two subsequent reductions.

The MS/MS of 529 DAR mass indicates a reduction occurs at either the β- or δ- meso position, based on the naming scheme of a porphyrin (Figure 3.4, Panel C). Moreover, the observation of an even mass fragment at 364 m/z, indicates an odd number of nitrogens are present. This can be explained by the reduction of either the β- or δ- meso carbon atoms. To probe the structure of deuteroanaerorubin further, we used ^{13}C-methyl-S-adenosylmethionine ([^{13}C-methyl]-SAM) to prepare deuteroanaerorubin with the isotopic label incorporated (Figure 3.4, Panel B). We observed a [M+1] enrichment at 530 m/z, indicating incorporation of the isotopic label. Upon fragmentation of [^{13}C-methyl]-anaerorubin, we observed retention of approximately 66% of the isotopic label and 33% without, relative to the fragmented peak (365 and 364 m/z, respectively) (Figure 3.4, Panel D).

ChuY displays kinetic cooperativity with the DAB substrate. Considering the homology to BVR, we attempted activity assays using DAB and NADPH as substrates for ChuY. Omission of either substrate resulted in no observable changes in the UV-visible spectrum of DAB within five minutes. When both substrates were present, a decrease of the 439 nm and 780 nm features was observed in an enzyme-dependent manner (Figure 3.6, Panels A and B). The loss of the Soret and longer wavelength features are consistent with a reduction of DAB and disruption of the conjugation within the tetrapyrrole. We performed substrate saturation curves of NADPH in the presence of 5 μM DAB by monitoring the two wavelength maxima for the tetrapyrrole (439 ad 780 nm). The rates of deuteroanaerobillin reduction were plotted using the extinction coefficients 95 and 31.5

mM^{-1} cm^{-1}, respectively. Additionally, all rates were obtained within the first 100 seconds of the assay as a Selwyn's test[212] indicated enzyme death at greater time intervals. The available kinetic data shows that *E. coli* ChuY exhibits strongly sigmoidal kinetics for NADPH and were fit to the Hill equation (Eq. 4.1), with a K_m^{app} of 3.5 and 3.7 μM, and a hill of 2.5 for the respective wavelengths (Figure 3.6, Panels A and B). These data suggested positive cooperativity with the NADPH ligand. However, cooperativity observed in steady state kinetics is not definitive of a thermodynamic process and must be confirmed by equilibrium binding studies[213–215]. Hence, we applied intrinsic protein fluorescence to study the binding of the cofactor to ChuY. Upon exciting at 280 nm we observe a tryptophan emission signal at 354 nm. Addition of NADPH caused quenching of the tryptophan emission peak in a concentration dependent manner. The change in fluorescence intensity was plotted with respect to the concentration of free NADPH and the data fit to a hyperbola. (Figure 3.7, panel C). All thermodynamic and kinetic parameters observed are shown in table 3.3.

Since we observe cooperativity in steady state kinetics and not in equilibrium binding experiments, we acquired the saturation plot of DAB to provide insight to the kinetic model of ChuY. The initial concentration of DAB was calculated by the extinction coefficient at 780 nm at initial time points of the assay and plotted against the respective rates. NADPH was supplied to 10x the K_d (30 μM) in assays, which exhibited a V_{max} that decreased with increasing concentrations of DAB (Figure 3.6, Panel E). The data was modeled to an equation for substrate inhibition (Eq. 4.2) and displayed a K_m^{app} of 1.6 $\pm$ 0.3 μM and K_i^{app} of 14 $\pm$ 2 μM (Table 3.3). Considering the sigmoidal substrate saturation curve for NADPH, the observation of substrate inhibition for deuteroanaerobilin suggested kinetic cooperativity. To test the possibility of a kinetic preference for binding NADPH, we performed the same DAB substrate saturation curve with more than 200x K_d of NADPH (500 μM) in the assay to probe the substrate inhibition effect (Figure 3.7, Panel B). Providing excess NADPH

would cause thermodynamic favoring of NADPH binding prior to DAB. This would result in a change of the apparent K_i^{app} if the substrate inhibition is not due to a thermodynamic event or substrate solubility. The data attained were modeled to the substrate inhibition equation (Eq. 4.2). Although the V_{max} and K_m^{app} were similar to the previous DAB saturation, the K_i^{app} was estimated to be 107 µM, albeit with a significant error due to the concentration range of DAB that was tested.

3.3 Discussion

Biliverdin reductases (BVRs) are responsible for the conversion of biliverdin to bilirubin, which provides antioxidant benefits and allows for the removal of tetrapyrroles from the cell[216,217]. BVRs are prevalent in eukaryotic heme degradation pathways and play a role in the regulating the levels of bilirubin in the cell, which can act as an antioxidant. Although many heme oxygenases have been characterized in bacterial systems, no equivalent reductase has been identified that corresponds to the well-established pathway in eukaryotes. With the exception of cyanobacteria, ChuY is the first example of a verdin reductase characterized from a bacterial heme degradation system that is similar to BVR. Our data suggest ChuY uses NADPH as a co-substrate to reduce anaerobilin and deuteroanaerobilin (DAB) (Figures 3.5 and 3.5) We show that despite the genetic differences, ChuY has structural homology to fetal BVβR (Figure 3.3, Panel A and B). Binding studies suggested ChuY uses NADPH rather than NADH as the preferred nicotinamide cofactor. Tryptophan fluorescence did not result in meaningful quenching of the ChuY signal when up to 80 µM NADH was used in the assay, whereas the NADPH binding isotherm suggests a dissociation constant of 2.7 µM.

The oxygen-independent heme degradation pathway from *E. coli* O157:H7 consists of ChuW, a radical SAM methyltransferase, which methylates heme to form the linear tetrapyrrole anaerobilin. ChuY uses anaerobilin as a substrate reducing it to the tetrapyrrole termed "anaerorubin", which has little color. Mass spectrometry analysis of the isolated anaerorubin suggests a four electron reduction of anaerobilin, presumably from two subsequent turnovers (Figure 3.5). When using deuteroheme as a substrate, the reaction catalyzed by ChuW results in the decyclization of the macrocycle causing the release of iron from the tetrapyrrole[209]. However, formation of (^{13}C-methyl)-deuteroanaerorubin resulted in only a two electron reduction (Figure 3.4). Comparing the fragmentation patterns of DAR

prepared with either ^{12}C or ^{13}C-methyl DAB were useful for proposing a structure. The even mass observed for the dominant 364 m/z species indicates a loss of one nitrogen atom (Figure 3.4, Panel B). This fragment observed would be from a reduction that occurred at either the β- or the δ-methine bridging carbon. The precise location of the ^{13}C-methyl is still unclear as it could either be located at the 1 or 21 position of the linear tetrapyrrole based on the predicted mechanism by ChuW. However, fragmentation of ^{13}C-methyl DAR allows for the identification of the reduction position in relation to the isotopic label. For instance, a reduction occurring on the distal side of the tetrapyrrole would cause retention of the label, whereas reduction to the adjacent methine bridging carbon would result in the loss. The fragmentation shows both species in a 3:1 ratio, respectively, suggesting the reduction can occur at either position and/or the isotopic label can be at either side of the bilin. Based on the postulated mechanism for anaerobic heme degradation both are possible.

When performing steady state kinetics of *E. coli* ChuY using deuteroanaerobilin (DAB) as a substrate, we observe a distinct positive cooperativity with respect to NADPH saturation, but substrate inhibition with respect to DAB (Figure 3.7, Panels A, B and E). Although cooperativity is common for many oligomeric enzymes, sigmoidal kinetics do not unequivocally establish thermodynamic cooperativity[213,214]. Equilibrium binding studies are the only way to confirm the possibility of a site to site communication described by thermodynamic cooperativity[213–215]. Thus, the observation of a hyperbolic binding isotherm of ChuY and NADPH indicate a kinetic cooperative mechanism. However, kinetic cooperativity can be described by either a hysteretic lag in progress curves[215,218], or it can be due to a kinetic preference for substrate binding during turnover[219]. Based on the observation of sigmoidal kinetics with NADPH saturation and substrate inhibition with DAB, the kinetic cooperativity by ChuY is best explained by random association of substrates with a kinetically preferred path for NADPH binding (Figure 3.8, Panel A). This mechanism is possible if $k_1k_3 > k_2k_4$

and if k_5 is not rate-limiting. The kinetic differences for substrate binding in the random association model provides an explanation for the apparent inhibition observed for DAB saturation kinetics. At lower concentrations of DAB, turnover will proceed through the kinetically preferred path of initial NADPH binding. However, at higher concentrations of DAB the kinetic path will gradually switch to the kinetically unfavored path of initial DAB binding. As more of the ChuY population switches to this path, the rate decreases causing what appears to be substrate inhibition. To overcome the apparent inhibition effect, NADPH must be provided in excess to thermodynamically favor binding of the nicotinamide cofactor throughout the DAB saturation. Providing 200x the k_d of NADPH caused a 10x increase in the apparent K_i (Figure 3.8, Panel B) due to the majority of ChuY binding NADPH initially before proceeding through the kinetically preferred path. Since NADPH will likely at higher concentrations than anaerobilin *in vivo*, this kinetic model may provide a physiological benefit in quicker turnover when anaerobilin is produced. In fact, the ability to pre-load ChuY with NADPH, would allow for the greatest activity at concentrations of anaerobilin below 2 µM.

ChuW has sequence homology to HutW from *Vibrio cholerae*, however these enzymes form a different clade when the phylogenetic tree is constructed based on sequence identity[209]. Suggestions for this diversity may underlie the fact that *E. coli* contains this anaerorubin reductase ChuY, whereas *Vibrio* species harbor *hutZ* in the equivalent location on the operon. There are currently two models for HutZ; the initial characterization suggested the ability for *hutZ* to functionally replace an HO. However, HutZ did not appear to have such activity in enzyme assays. Considering the ability for HutZ to bind heme, Wyckoff *et al.* predicted the protein acts as a heme chaperone[9]. Later reports suggested HutZ has *in vitro* HO activity, though products were never identified and the bonafide heme degrading activity was disputed by others[10]. The structure has been solved to 2.0 Å, and is described as having a split barrel fold that is typical for FMN-binding proteins[184]. Future

studies will test overlaping features of HutZ and ChuY to see if HutZ can replace ChuY using a flavin cofactor.

3.4 Materials and Methods

Expression, purification, and enzymatic assay of ChuY. ChuY was expressed by growing the *E. coli* strain BL21 DE3 strain containing an IPTG inducible expression plasmid that carried the gene coding for ChuY with a 6xHis tag (pET15a). In short, a 20 mL starter culture was grown for 6 hours before inoculating six 1 L flasks containing TB media. Cultures were grown at 37℃ shaking at 200 rpm until the O.D. at 600 nm reached 0.8. IPTG was added to a final concentration of 500 µM. Cultures were incubated at 18℃ overnight shaking at 200 rpm and harvested by centrifugation before being stored at -80℃. The frozen cell pellets were solubilized in buffer containing 20 mM Tris (pH 8.1), 300 mM KCL, and 10% glycerol with trace amounts of PMSF, lysozyme, and DNase. Cells were lysed by French pressure cell and lysate was ultracentrifuged at 65,000 g for 1.5 hours. The supernatant was applied to Talon resin, washed with 2 column equivalents of water, and 8 column equivalents of solubilization buffer. After washing the column with 3 column equivalents of 10 mM imidazole, ChuY was eluted with buffer containing 250 mM imidazole. Fractions containing ChuY were pooled, buffer exchanged to remove imidazole, and then concentrated. Protein content was analyzed by SDS-PAGE and Biuret analyses before freezing aliquots at -80℃.

Crystallization, data collection, phasing, model building and refinement of ChuY. Diffraction quality crystals of ChuY were obtained when purified enzyme (1 µL at 15 mg mL^{-1}) was mixed 1:1 with precipitating solution containing 10% 1,4-butanediol, 100 mM Bis-Tris buffer (pH 5.5), 19% PEG 3350, and 150 mM lithium sulfate (80 µL reservoir) in a hanging drop experiment. Crystals appeared within 48 hours after incubation at 18℃.

Monochromatic data collection with 0.98 Å X-rays was performed at SER-CAT on the 22-BM beamline at the Advanced Photon Source (Argonne, IL). Data were processed using SGXPRO, and 5% of the reflections were set aside for cross-validation (Table 3.1)[220]. A BLAST search against the Protein Data Bank structures revealed that the structure of a Rossmann-fold NAD(P)-binding family protein from *Shigella flexneri* was 89% similar to ChuY. A poly-alanine model of this structure (PDB ID 3QVO) was used as a successful molecular replacement model for initial phasing using PHENIX[221]. Successive rounds of model building and refinement were performed using COOT[222] and PHENIX[221].

Sedimentation Velocity. ChuY (1 mM) was dialyzed into 25 mM HEPES (pH 7.5) and 200 mM KCl. After dialysis, 400 µL of diluted sample (24 µM) or reference buffer solution was loaded into 12 mm double-sector Epon centerpieces equipped with quartz windows and equilibrated at 20℃ in an AN60 Ti rotor for 1 hr. Sedimentation velocity studies were collected in an Optima XLA analytical ultracentrifuge using a rotor speed of 50,000 rpm at 20℃. Data were recorded at a wavelength of 280 nm using a radial step size of 0.003 cm. The partial specific volume, density, and viscosity were calculated to be 0.73478 mL/g, 1.00961 g/mL, and 0.01017 P, respectively, using SEDNTERP[223]. SEDFIT[224] was used to model and analyze the sedimentation data. Modeled data were fit as a continuous sedimentation coefficient c(s) distribution using the baseline, meniscus, frictional coefficient, systematic time-invariant noise and radial-invariant noise. The weight-averaged sedimentation coefficient (sw) for each species was determined by integrating each peak in the c(s) distribution. The theoretical sedimentation coefficient (S) values were calculated with HYDROPRO[211] using the ChuY atomic coordinates. The root-mean-square deviation (rmsd) value for the experiment was $<$0.002 OD.

Mass spectrometry of anaerorubin. Deuteroanaerobilin and anaerobilin were prepared as previously described. Isolated substrates (50 µM) were mixed with 200 µM NADPH and 5 µM ChuY. After one hour, the reaction mixture was applied to a C1-sep pack

(Silicycle™) after washing with 1 mL of methanol, water, and then reaction buffer. The column was washed with 5 mL of water before eluting in methanol. Products were analyzed using nanospray ionization mass spectrometry (NSI-MS) by direct infusion into a linear ion trap mass spectrometer (LTQ-Orbitrap Discovery; Thermo Fisher Scientific) using a nanoelectrospray source at a syringe flow rate of 0.40 µL min^{-1} and capillary temperature set to 210℃. Fragmentation by collision-induced dissociation (CID) in MS/MS and MSn was used with normalized collision energy of 35-40%.

Steady state kinetics by ChuY. Typical UV-vis assays were performed using a 3 mL quartz cuvette prepared anaerobically and sealed with a rubber septa. Deuteroanaerobilin, prepared as previously described[209], and NADPH were added to buffer containing 20 mM Tris (pH 8.1), 300 mM KCl, and 10% glycerol for a 2 mL reaction. Assays were initiated by injecting isolated ChuY using a gas-tight syringe. Spectra were recorded using an Agilent 8A53 diode array spectrophotometer with a Peltier temperature controller set to 25℃ and a glass slide to reduce ultraviolet light exposure of DAB. Spectra were recorded in one-second intervals for the course of 15 minutes. Activity was determined by monitoring initial changes at 439 nm and 780 nm using extinction coefficients previously reported[209]. Data were fit using nonlinear regression in PRISM (GraphPad Software Inc., San Diego, CA). The substrate saturation curve were fit to either a hyperbolic or sigmoidal model based on residual analysis (for hyperbolic kinetics, h = 1):

$$v_o = \frac{V_{max}[S]^h}{(K_m^h + [S]^h)} \tag{3.1}$$

The deuteroanaerobilin substrate curves of ChuY revealed substrate inhibition and were fit to:

$$v_o = \frac{V_{max}[S]}{(K_m + [S])(1 + \frac{[S]}{K_i})} \tag{3.2}$$

Equilibrium Binding Assays. Intrinsic tryptophan fluorescence quenching of ChuY was

monitored to assess binding of NADPH. Fluorescence binding titrations were performed at 22℃ in reaction buffer (20 mM Tris, pH 8.1, 150 mM KCl, and 5% glycerol) containing 400 nM ChuY. Fluorescence was measured using a Shimadzu RF-5301 spectrofluometer with excitation and emission wavelengths at 280 and 354 nm, respectively, and slit widths set to 5 mm and a glass slide was used in the emission path. Raw data were corrected for the inner filter effect as previously described[225]. Due to the moderate affinity for NADPH ($<$4 μM), we used the following relationship to calculate unbound NADPH (NADPHfree):

$$\frac{\Delta F}{\Delta F_{max}} = \frac{[ChuY_{bound}]}{[ChuY_{total}]} \tag{3.3}$$

$$[ChuY_{bound}] = [NADPH_{bound}] \tag{3.4}$$

$$[NADPH_{free}] = [NADPH_{total}] - [NADPH_{bound}] \tag{3.5}$$

The corrected $\triangle$F was plotted versus the free NADPH concentrations. The dissociation constant (K_d) and the cooperativity were determined by fitting the data to a sigmoidal model based on residual analysis:

$$\Delta F = \frac{(\Delta F_{max}[NADPH^h_{free})}{(K^h_d + [NADPH_{free}]^h)} \tag{3.6}$$

3.5 Figures and Tables

Table 3.1: Data collection and refinement statistics for ChuY

PDB ID code	5FFQ
Space Group	$P2_1$
Wavelength	0.98
Resolution Range (Å)	50.0-2.0
Outer Shell	2.07-2.0
Unique Observations	30,647
Completeness (%)	98.9(90.3)[a]
R_{sym} (%)[b]	0.08(0.36)
Redundancy	3.8(2.3)
I/σ	14.3(2.8)
Unit Cell (*a, b, c*) in Å	50 x 63 x 66; α=γ=90, β=106
Protein Atoms	3087
Solvent Atoms	306
Resolution Limits (Å)	50.0-2.0
R_{cryst} (%)	17.8
R_{free} (%)	23.9
rmsd bonds (Å)	0.008
rmsd angles (°)	1.07
average B factor (Å^2)	27.3

[a] Numbers in parentheses denote values for the outermost resolution shell.

[b] $R_{sym} = \sum hkl[\sum I(|I_{hkl,I} - < I_{hkl}>|)]/\sum hkl, I<\mathrm{I}_{hkl}>$, where I_{hkl} is the intensity of an individual measurement of the reflection with indeces hkl and $<\mathrm{I}_{hkl}>$ is the mean intensity of that reflection.

Table 3.2: Interface residues

electrostatic interactions between chains			
Arg87 (NH1 and NH2) $\leftrightarrow$ Glu130 (Oϵ1) Arg87 (NH2) $\leftrightarrow$ Glu130 (Oϵ2)			
buried residues			
Tyr83	Leu84	Ile90	Asp91
Glu94	Gly110	Trp113	Gln126
Thr132	Leu133	Ser136	Trp137
Gln139	Thr140	Ser141	Gln194

Table 3.3: ChuY thermodynamic and kinetic parameters

	steady state parameters[a]				**equilibrium binding**[b]	
ligand	$K_m{}^{app}$ (μM)	Hill coefficient	k_{cat} (s^{-1})	$K_i{}^{app}$ (μM)	Hill coefficient	K_d (μM)
NADPH	3.5 ± 0.2	2.5 ± 0.5	0.082 ± 0.002[c]	-	1.0[d]	2.7 ± 0.2[d]
NADPH	3.7 ± 0.2	2.6 ± 0.3	0.082 ± 0.002[c]	-		
DAB	1.6 ± 0.3[e]	1.0[e]	0.0127 ± 0.009[e]	14 ± 2[e]		
DAB	1.2 ± 0.2[f]	1.0[f]	0.014 ± 0.01[f]	108 ± 67[f]		

[a] Fit to eq. 1 or 2 in "Materials and Methods".
[b] NADPH binding fit to equation 4.6 in "Materials and Methods".
[c] Based on NADPH saturation curve with DAB not fully saturated.
[d] Based on intrinsic Tryptophan fluorescence quenching (see Figure 3.6, panel C).
[e] Based on DAB saturation kinetics with $10K_d$ of NADPH.
[f] Based on DAB saturation kinetics with $200K_d$ of NADPH

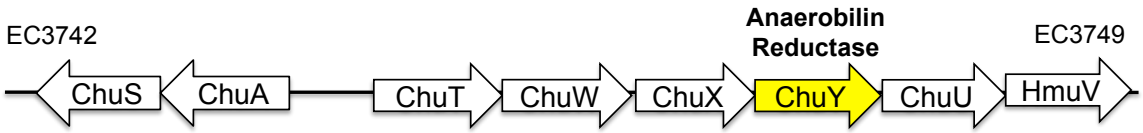

Figure 3.1: Genetic organization of the heme utilization operon in *E. coli* O157:H7.

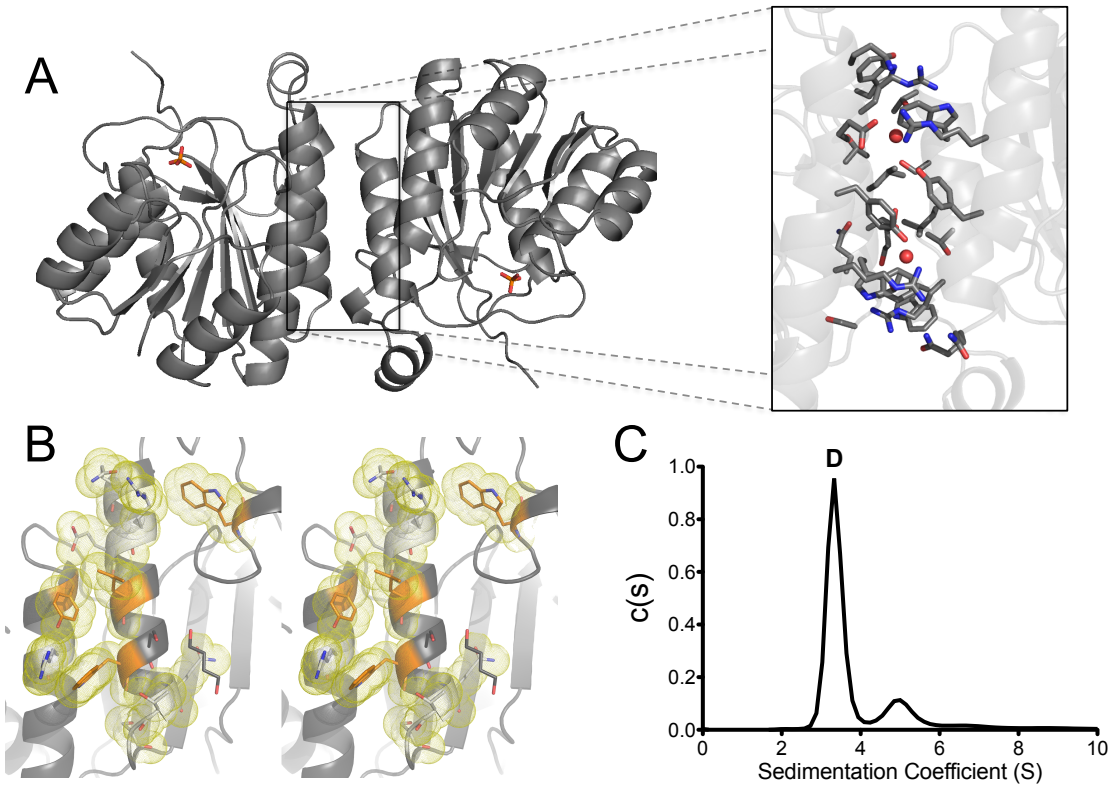

Figure 3.2: Cartoon representation of the ChuY dimer *(Panels A and B)* and the sedimentation velocity study *(Panel C)*. *(Panel A)* Cartoon representation of the native structure for ChuY with a zoomed in window of the stick representation of the dimer interface residues display primarily hydrophilic interactions. *(Panel B)* Wall-eyed stereoview for half of the interface residues colored orange and with their respective Van Der Waals surface shown in a yellow cloud. *(Panel C)* The c(s) sedimentation distribution of ChuY reveals a species at 3.4 S (90 %) and a species at 5.0 S (10 %) corresponding to a tetramer.

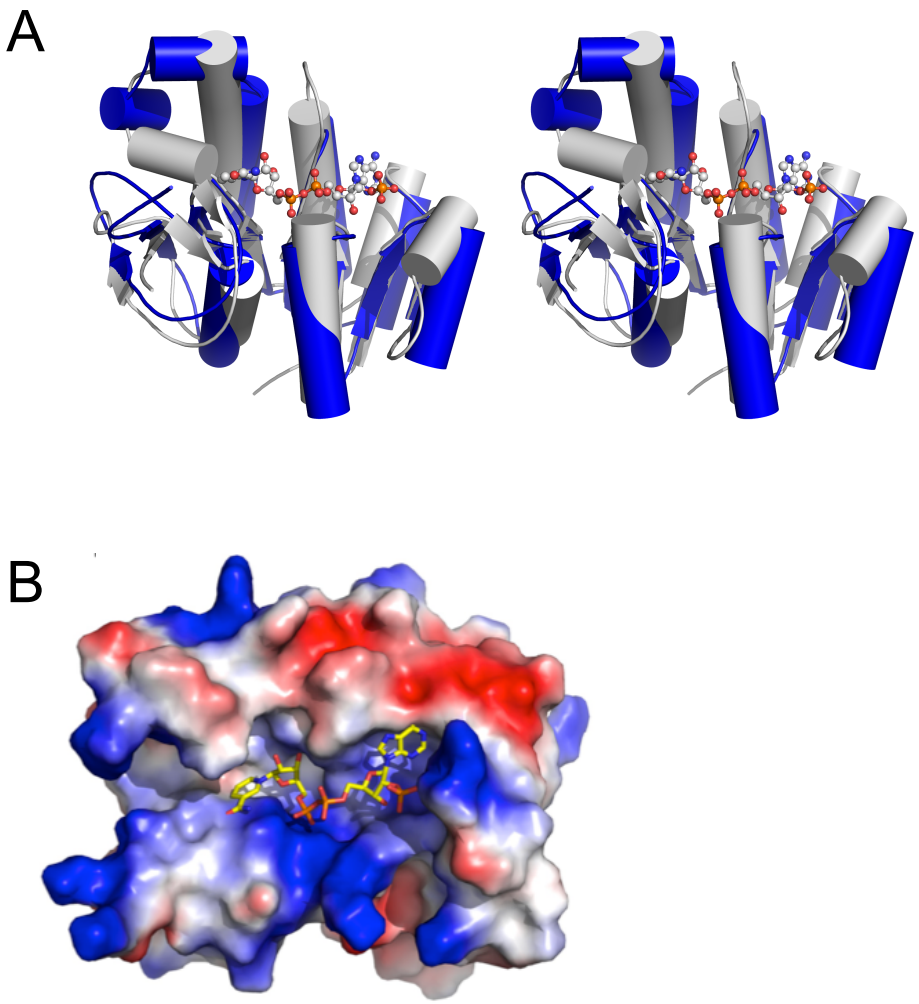

Figure 3.3: ChuY structural overlay with biliverdin β reductase (PDB 1HE3) *(Panels A and B)*. *(Panel A)* The cartoon representation of ChuY aligned with biliverdin β reductase by the Cα carbons resulted in a r.m.s.d of 3.06 Å^2. *(Panel B)* The same overlay showing only the cofactor from biliverdin reductase and the electrostatic surface representation of ChuY reveals the likely binding pocket.

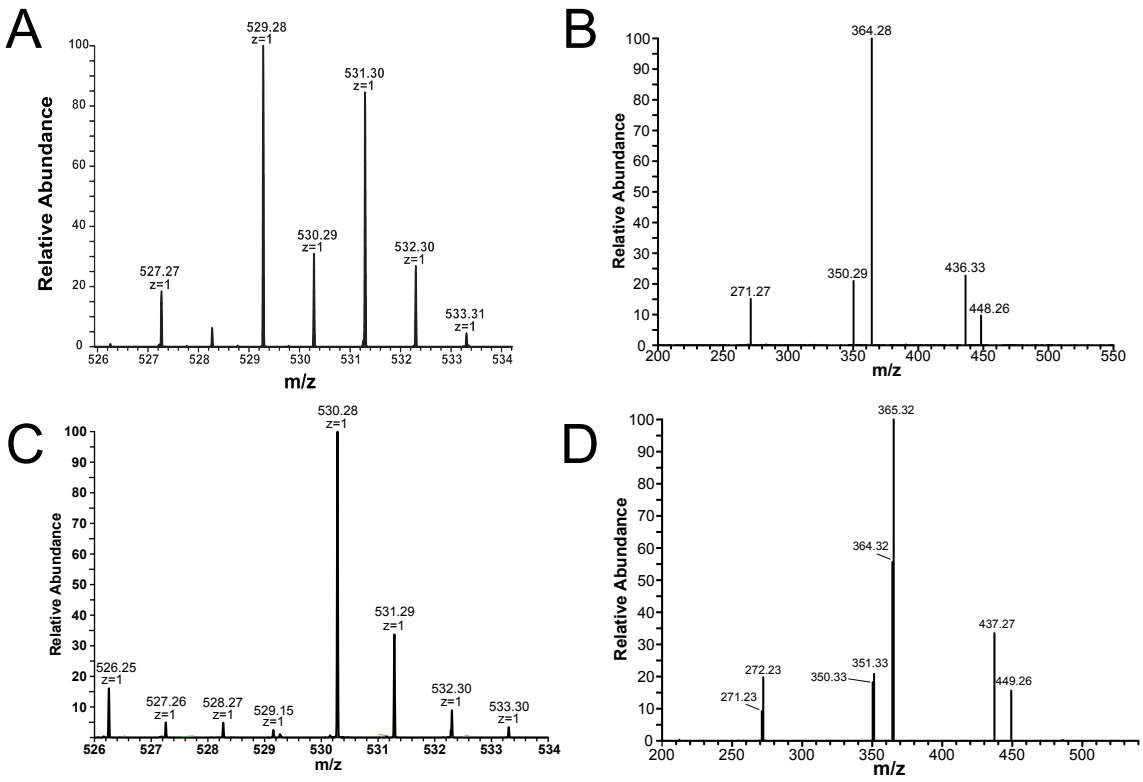

Figure 3.4: Mass spectrometry of deuteroanaerorubin (DAR). *(Panel A)* MS analysis of DAR resulted in a $[M+H]^+$ mixture of 529 and 531 m/z. *(Panel B)*MS/MS fragmentation of DAR reavealed a dominant fragment at 364 m/z corresponding to the loss of a pyrrole ring. *(Panel C)* MS of (^{13}C-methyl)-DAR attained by reacting ChuY with DAB prepared using (^{13}C-methyl)-SAM indicated retention of the isotopic label with a dominant $[M+H]^+$ of 530 m/z. *(Panel D)* Fragmentation of the isotopically labeled DAR resulting in a dominant species at 365 and 364 m/z indicating the label could be lost upon fragmenting DAR.

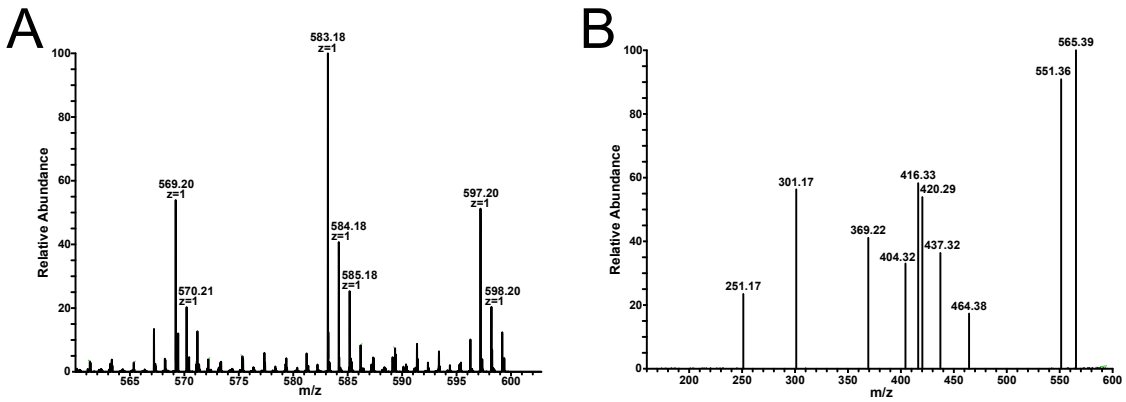

Figure 3.5: Mass spectrometry of anaerorubin was performed by assaying ChuY (2 µM) with 30 µM of anaerobilin and NADPH for 4 hours. *(Panel A)* Isolated products were analyzed by NSI-MS by direct infusion and revealed a $[M+H]^+$ at 583 m/z. *(Panel B)* MS/MS of anaerorubin reavealed multiple fragments corresponding to the reduction of the tetrapyrrole.

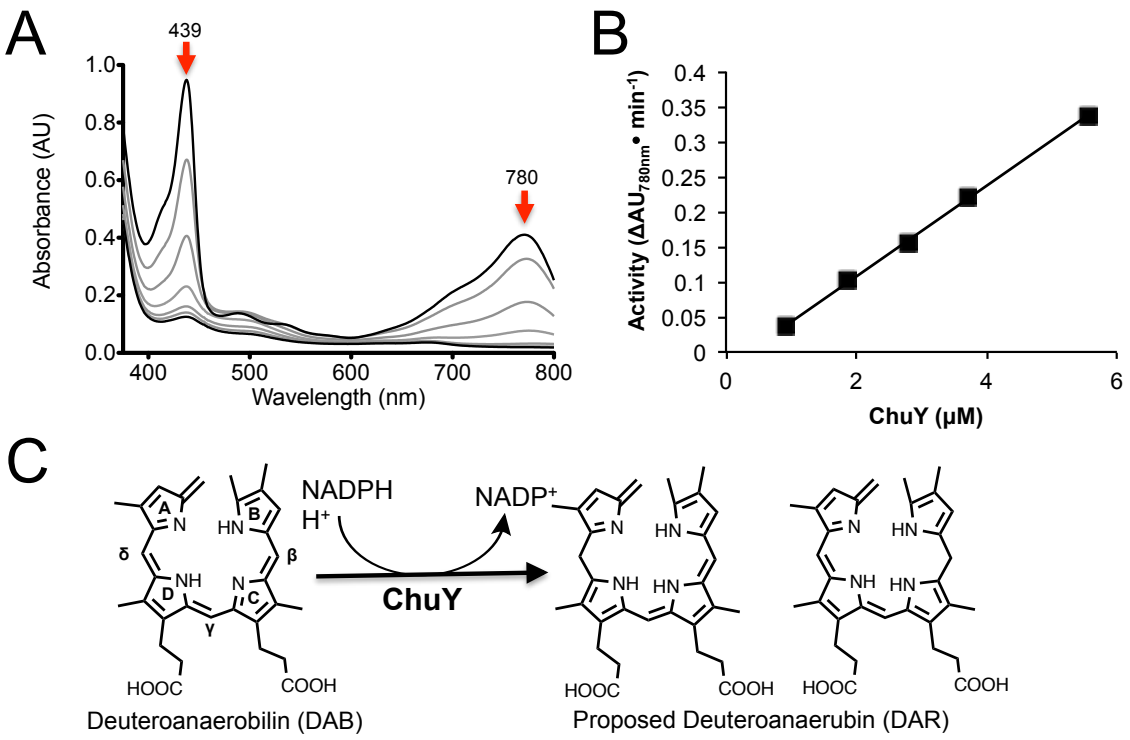

Figure 3.6: Activity assays of ChuY using Deuteroanaerobilin (DAB) as a substrate and the proposed reaction scheme. *(Panel A)* UV-visible spectrum of ChuY (1 μM) assay with Deuteroanaerobilin (15 μM) and NADPH (100 μM). Upon addition of NADPH, the 440 and 780 nm decrease with respect to time. *(Panel B)* Initial rate of ChuY activity with respect to the concentration of enzyme. *(Panel C)* The proposed reaction scheme based on the mass spectrometry data from Figure 3.4.

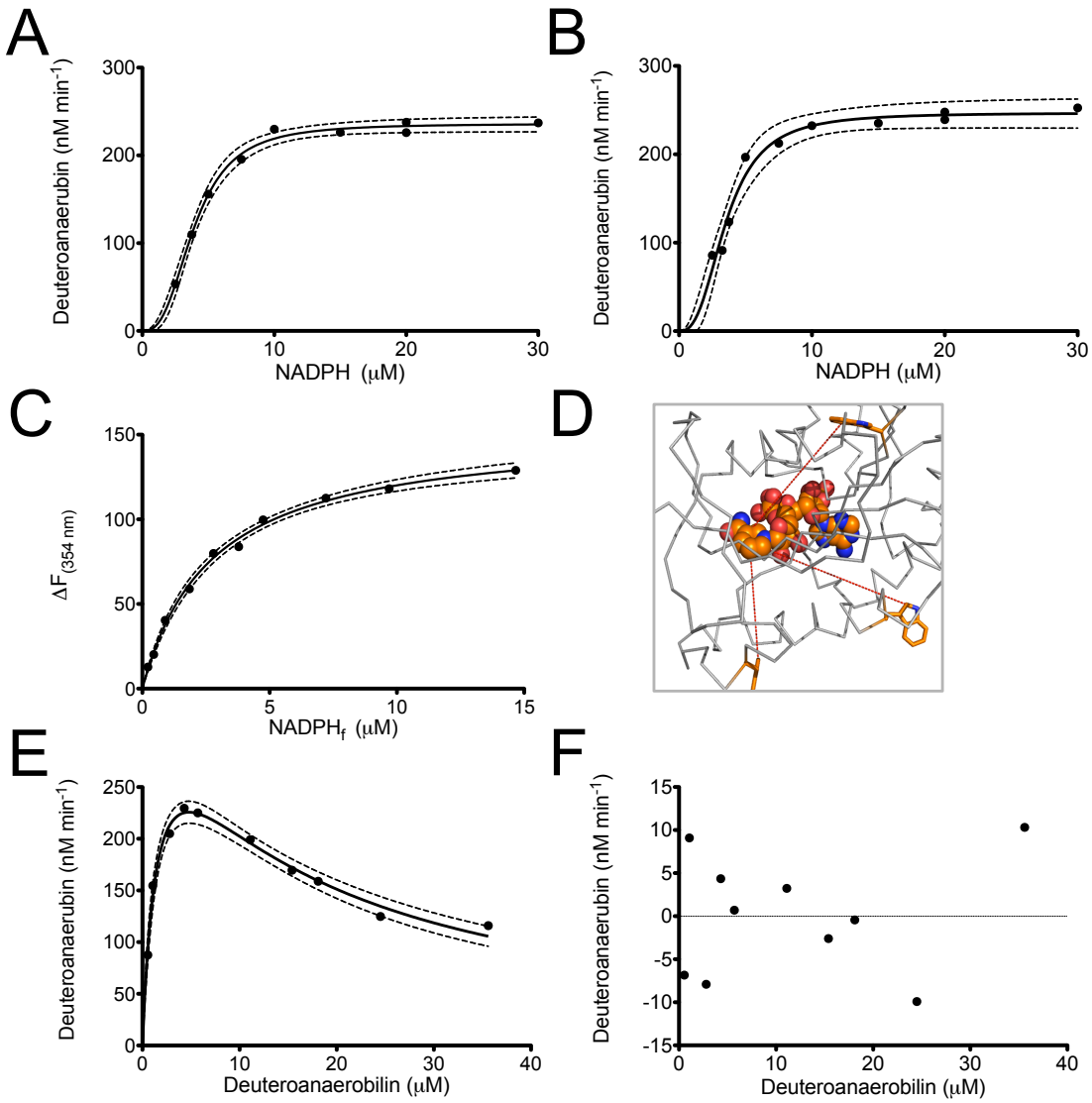

Figure 3.7: Steady state analysis and equilibrium binding of ChuY. *(Panels A and B)* NADPH saturation kinetics were performed by monitoring the decrease in either the 440 or 780 nm absorption maxima using 5 μM DAB and 50 nM ChuY and plotted with respect to the concentration of NADPH. The saturation plots were fit to the Hill equation (Equation 4.1) and analyzed by residual analysis. *(Panel C)* Equilibrium binding assays were performed by intrinsic tryptophan fluorescence quenching by monitoring the Δ emission maxima for ChuY tryptophan at 354 nm with respect to the NADPH concentration. *(Panel D)* Spatial arrangment of the ChuY tryptophan residues (orange) in relation to the predicted NADPH binding site. *(Panel E)* DAB saturation kinetics in the presence of 30 μM NADPH. The plot was fit to an equation for substrate inhibition (Equation 4.2). *(Panel F)* Residual analysis of the substrate inhibition curve from Panel D.

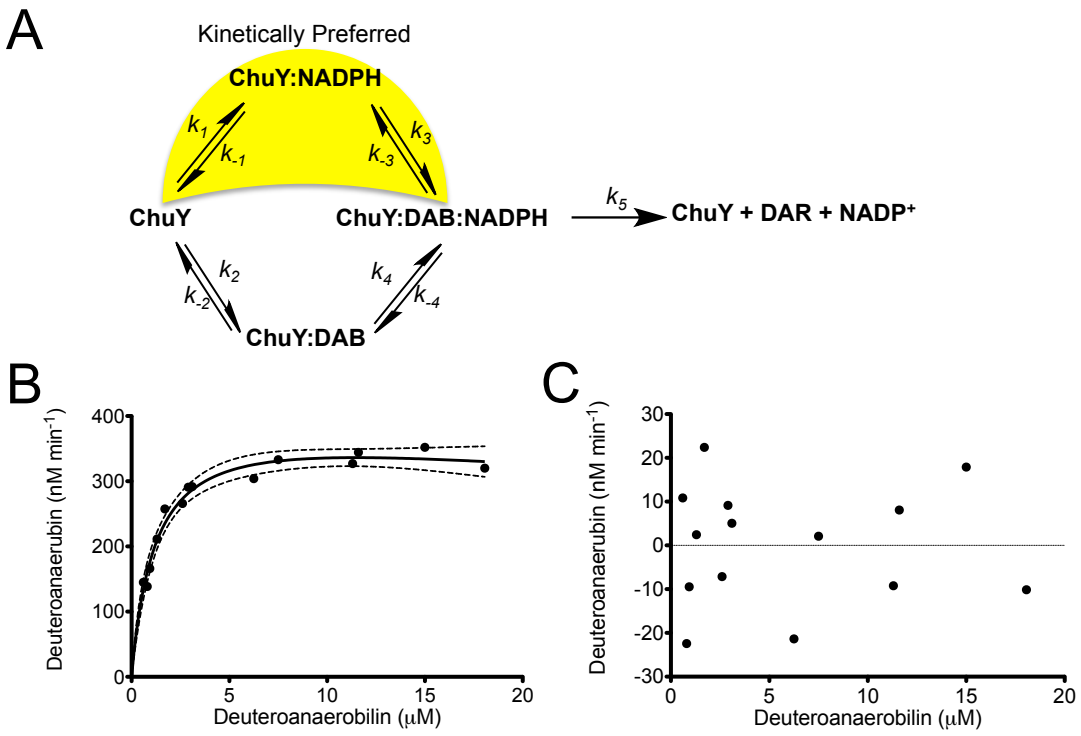

Figure 3.8: Validating the proposed kinetic model of ChuY. ChuY appears to follow a random association kinetic model with an kinetic preference for NADPH binding *(Panel A)*. *(Panel B)* DAB saturation kinetics were performed similarly to Figure 3.6, Panel E, using approximately 200 μM NADPH. The rates were plotted with respect to the DAB concentration and fit to the equation for substrate inhibition (Equation 4.2). *(Panel C)* Residual analysis was used to assess the fit of the data.

CHAPTER 4

FUTURE DIRECTIONS AND FINAL REMARKS

For at least 50 years, enzymatic heme oxygenation was thought to only occur by the canonical heme oxygenase originally discovered in mammals. Due to the similarities between the eukaryotic and prokaryotic HOs, the presence of an oxygen-independent heme degradation pathway in microorganisms has remained largely overlooked. The discovery of the novel verdins produced by IsdG and MhuD represents a milestone demonstrating that heme degradation pathways have evolved to suit the physiological need of the organism. In these cases, the enzymes limit CO production by either releasing formaldehyde (IsdG) or retention of the single carbon atom on mycobilin (MhuD). Considering that the function of these enzymes is to degrade heme to liberate iron, perhaps the emergence of these pathways is a product of convergent evolution by which certain organisms developed specific pathways to survive in their ecological niche. Indeed, this hypothesis would provide an explanation for the vast differences in protein structure between HemO/hHO-1 and MhuD/IsdG in addition to the subtle differences in mechanism. Likewise, this hypothesis provides the foundation for understanding the the origins of ChuW, as there does not seem to be overlap between the oxygen-dependent and oxygen-independent heme degradation pathways since the majority of the organisms searched have one or the other.

Postulating a mechanism for oxygen-independent heme degradation

The precise mechanism by which anaerobic heme degradation can occur is of interest for several reasons; mainly to ***i)*** provide insight to the HemN mechanism and ***ii)*** developing inhibitors of the enzyme as potential new antibiotics. We have postulated a detailed mechanism using the information attained from our study (Figure 4.1) and precedent set for other class C RSMTs[148]. However, studies of ChuW are still in their infancy. Considering the sequence alignment for ChuW, HemN, and other Class C RSMTs (Figure 2.2), many of the residues responsible for binding a second SAM molecule are conserved. Therefore, ChuW is a tri-substrate enzyme that binds two molecules of S-adenosylmethionine at two distinct locations within the active site in addition to heme. These sites presumably have different thermodynamic properties for binding considering interactions expected. The SAM molecule that gets reductively cleaved (SAM1) coordinates to the unique iron in the [4Fe-4S] cluster. This interaction is fundamental for all radical SAM enzymes and often have a Michaelis constant (K_m) between 4 and 50 μM[226]. The interactions for SAM2, which performs the methylation, is likely with residues similar to HemN and may have a lower affinity based on the relative interactions that occur in HemN with SAM2. Performing anaerobic isothermal titration calorimetry may provide details regarding the two sites. However, the use of site-directed mutagenesis and a detailed kinetic investigation is needed to determine random association or sequential binding between the substrates.

In the absence of crystallographic data for ChuW, probing the electronic environment of the [4Fe-4S]-SAM1 complex may provide additional mechanistic insight. In the absence of SAM, EPR of reduced ChuW results in an axial spectra characteristic of other radical SAM enzymes (Figure 4.2, top trace). However, adding S-adenosylmethionine to a concentration of 1 mM resulted in a broad feature at g = 1.74 that could be due to electronic coupling of the iron-sulfur cluster to another species (Figure 4.2). This spectra is unlike what has been

observed in other radical SAM enzymes[109,125]. The use of ^{57}Fe for the reconstitution of the Fe-S cluster and isotopic labeling of S-adenosylmethionine, or analogs of SAM, may be used in conjunction with continuous wave EPR and HYSCORE to determine the source of the spectrum observed. These techniques would also provide a spatial arrangement of these cofactors in the active site.

Once the 5'-dA• is formed from SAM1, hydrogen abstraction of the methyl-hydrogen from SAM2 makes sense based on our MS data (Figure 2.8). This abstraction would result in a SAM-methylene radical and is proposed to resolve in one of two ways. One option (Path A) is for radical addition on the α-meso carbon of heme directly to produce a SAM-heme adduct with a delocalized radical within the π-bonds of the porphyrin ring. This radical would be distinct from the heme-peroxidases that form a π-cation radical, but should be similar in a sense that detection by EPR would likely result in a broad organic radical centered at g = 2[227]. Similar to the studies done with HemN[122], the use of isotopically labeled heme with ^{13}C-carbon at various positions on the porphyrin and/or SAM, would allow for the further characterization of this radical. Upon collapse of the porphyrin radical intermediate a bond can form at the SAM-methyl bridge and either the C4 or C6 positions on the porphyrin ring to form a cyclopropane intermediate and release C-C bond scission to form a S-adenosylhomocysteine-yl radical[148]. With the addition of an electron, SAH will be formed.

The other option (Path B) is for the second electron needed for turnover to be used for production of a SAM-ylide that will perform nucleophilic addition on heme at the α-meso carbon. This would result in a porphyrin anion that would be stabilized by resonance of the porphyrin ring, similar to the porphyrin radical. Rearrangement of this anion can cause the formation of the similar intermediate proposed from path A, in which a cyclopropane intermediate is formed across the C4-C5 bond or the C5-C6. Formation of this intermediate would result in the SAH-methyl bond scission and release of SAH. However, this model is

difficult to test due to the lack of detection methods for a delocalized anion. One approach to use would be to compare the energetics of the intermediates formed in the two paths by molecular dynamics.

The two mechanistic paths converge at the formation of a cyclopropane intermediate. Acid-base chemistry is predicted to aid in the opening of the porphyrin ring by addition of a proton from solvent, as was observed when performing ChuW assays in $^{2}H_{2}O$ (Figure 2.7). This likely is a slow step in the mechanism, so it is a priority to use stopped-flow and freeze-quench spectroscopic methods to observe this intermediate and confirm the postulated mechanism. After tautomerization, anaerobilin in formed. However, anaerobilin has only been observed by MS and to confirm our prediction for the structure of this product NMR must be performed in the future. The difficulties with this analysis arise with the oxygen and photo-lability of anaerobilin, since exposure to either of these results in significant modification to the product. To reduce this effect, we have tried Ti^{3+}-citrate as a reductant in place of the *E. coli* flavodoxin reducing system. Using this reducing agent causes chemical reduction of the product after ChuW turnover, resulting in a product with a size of 529 m/z (Figure 4.3). MS/MS of this product results in a fragmentation pattern nearly identical to what is observed for DAR, the product of ChuY (Compare Figures 4.3 Panel B and 3.4 Panel B). Further studies are needed to be done to test the oxygen and photo-lability of this product for use in NMR.

Identification of ChuW as an antimicrobial target

Determining the mechanism for anaerobic heme degradation is exciting, but determining the function of this pathway *in vivo* is important for the development of antibiotics. ChuW homologues have been identified in predominately pathogenic microorganisms that infect mammals, fish, and plants. Although knockouts of *hutW* from *Vibrio cholerae* did not result in a pronounced phenotype[9], these experiments were largely performed *in vitro* and

cannot be used to determine competitiveness of the organism in the gut. If ChuW confers an advantage during colonization and/or pathogenesis, then the gene may be an effective antimicrobial target. From aspects of the mammalian pathogens, using a mouse model to test the competitive ability of a $\triangle$*chuW* strain of *E. coli* could be performed similarly to what has been attempted with ChuA, in which knockouts were tested for the ability to compete against wildtype[5]. However, those experiments prevented the organism from acquiring heme, whereas knockouts of *chuW* would specifically allow the prevention of heme-iron acquisition.

Since ChuW homologs are also identified in the plant pathogen *Pectobacterium carotovorum*, this organism could be used as a model to study *in vivo* function of ChuW similar genetic knockouts. *P. carotovorum* is one of the bacteria responsible for soft rot of crops and is the primary cause for post-harvest produce loss in agricultural farming. This organism is genetically tractable and the eukaryotic host could be a wide range of produce from a supermarket, allowing for inexpensive studies to be done. Thus, targeting ChuW in this organism could allow for the development of antibiotic pesticides that aid with increase production of crops by prevention of soft rot.

Despite the increased interest to understand the enteric microorganisms that comprise the human microbiome, other ChuW homologues are interesting in terms of the evolutionary implications they have for the anaerobic degradation of porphyrins. In fact, homologues have been identified bioinformatically in the anoxygenic purple non-sulfur bacteria, such as *Rhodopseudomonas* and *Rhodospirillum*. Considering ChuW does not require a porphyrin-chelated metal for turnover, it's possible this anaerobic pathway was originally utilized for degradation and clearing of porphyrin molecules in order to prevent cellular damage. This idea is based on the proposal that HemN and ChuW have a similar protein fold, which suggests that these two enzymes may have diverged during or shortly after the evolution of heme biosynthesis, as phylogenetic analysis suggests the class C radical SAM

methytransferases are distinct from HemN (Figure 2.12).

Delivery of heme to ChuW

One subtle difference in the ChuW/HutW protein family is the divergence between the two protein sequences which can be separated into two distinct groups when using an e-value cut off above 10^{-80}. Interestingly, this divergence correlates with the differences in the operon structure. In the *E. coli* subgroup, *chuWXY* are present, but the *Vibrio* subgroup encodes a *hutWXZ*. We have observed similar activity with *Vibrio fischeri* HutW compared to ChuW and it would be interesting to test the differences of activity in HutZ and ChuY to determine a functional overlap in these pathways. In addition, the precise mechanism of cytosolic heme transport, as well as storage, is an important aspect to address in the pathogenic *E. coli* strains. In *Pseudomonas aeruginosa* PhuS is responsible for transporting heme from the ABC transporter to the Pa-HO[65], but *E. coli* also has a ChuS and suggests a similar mechanism for heme transport. However, whether or or not ChuS can successfully deliver heme to ChuW and/or is selective for ChuW rather than Pa-HO is unknown. If ChuS is responsible for transporting heme to ChuW, addition of holo-ChuS with ChuW may facilitate faster turnover of ChuW, especially when coupled to ChuY. The observation of faster turnover, or a high affinity protein-protein interaction between ChuW and ChuS would suggest a physiological relevance. This would then call in to question the proposed interaction for HutX and HutZ, which has a dissociation constant of 500 μM[178].

Final remarks

The emergence of oxygen in the atmosphere during the Great Oxygenation Events provided a selective pressure for organisms to augment anaerobic pathways with aerobic mechanisms. This change is observed in nearly all aspects of metabolism, where fer-

mentation and anaerobic respiration was supplemented with oxidative phosphorylation. However, in some cases where organisms do not come into contact with molecular oxygen, these anaerobic pathways have persisted. This oxygen-independent heme degradation pathway is observed in bacteria that undergo anaerobic growth so that they may presumably outcompete other bacteria and/or survive in their niche. The work presented herein lay the foundation for determining the enzyme mechanism for ChuW, the oxygen-independent heme degrader. Many questions are still to be addressed, but the existence of a pathway that is evolutionarily different than the eukaryotic mechanism for heme degradation provide an opportunity to develop antibiotics that specifically target the anaerobic systems. Overall, these studies have merged the vast fields of heme degradation and radical SAM enzymes, of which before this work there was not an acknowledged relationship spanning over 60 years. Despite the stark differences in the mechanism for oxygen-independent versus oxygen-dependent heme degradation, the overall pathway is analogous to heme oxygenase and biliverdin reductase.

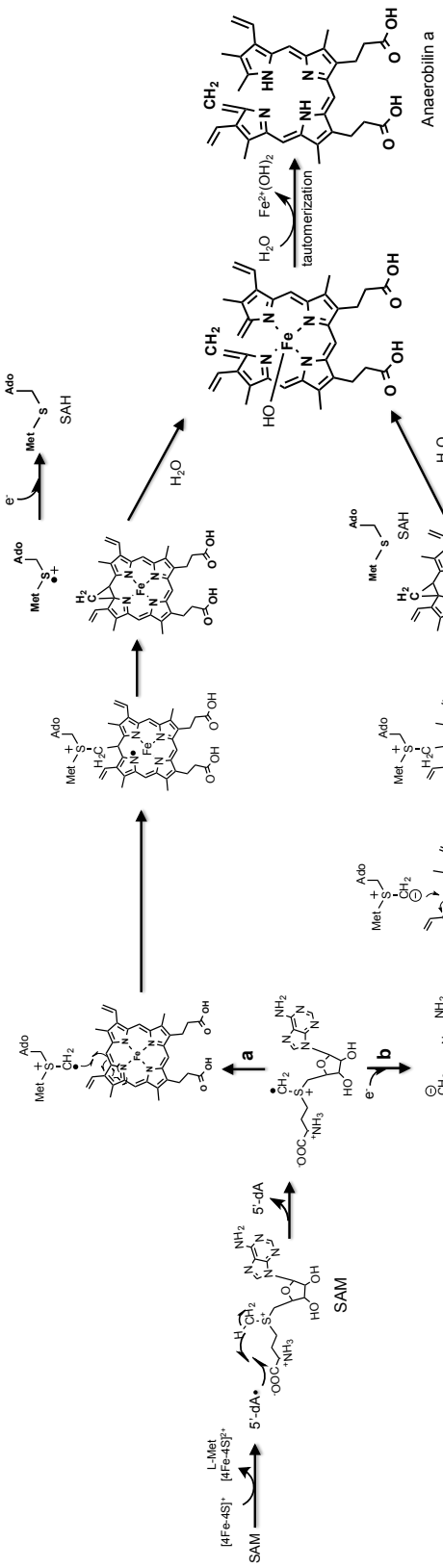

Figure 4.1: Postulated mechanism for heme decyclization

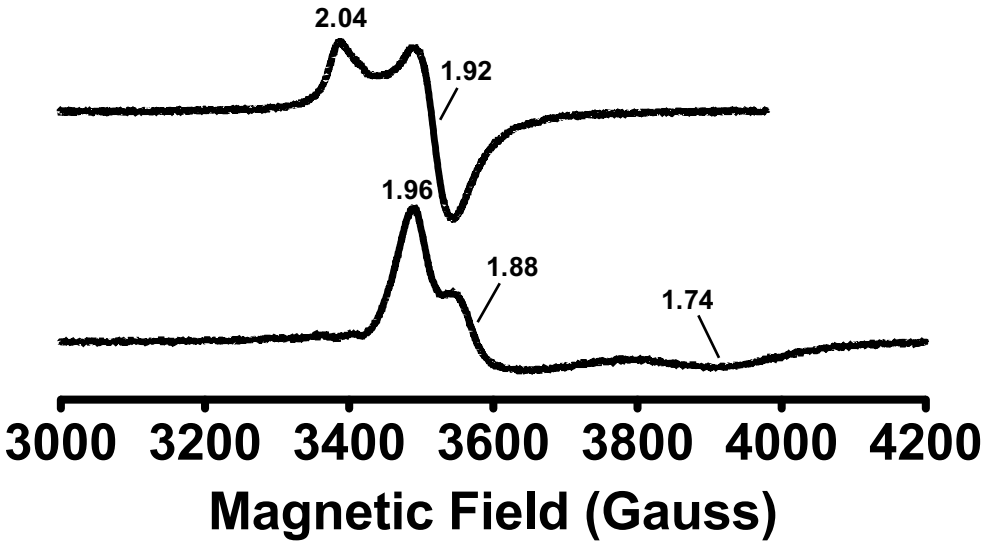

Figure 4.2: Effect of S-adenosylmethionine on the EPR spectrum of ChuW. *(Top spectra)* ChuW in the presence of 1 mM dithionite resembles an axial spectra for the coordination of a [4Fe-4S] cluster. *(Bottom spectra)* Upon addition of S-adenosylmethionine (1 mM) the lineshape changes significantly revealing a broad signal at g = 1.74.

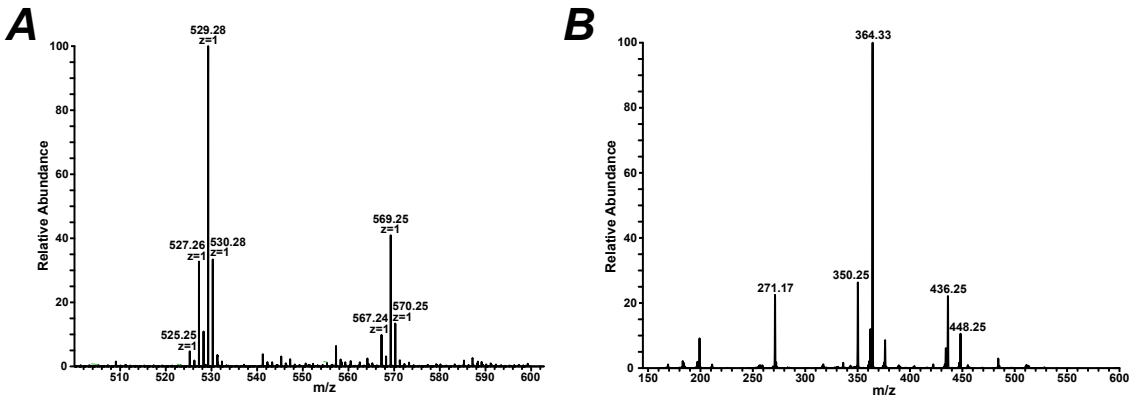

Figure 4.3: Mass spectrometry of DAR produced by Ti^{3+}-citrate. Enzyme assays were performed in the presence of 1 mM Ti^{3+}-citrate, 100 µM deuteroheme, and 250 µM SAM. Assays were initiated with 2 µM ChuW added to the mixture. Products were isolated as previously described[209]. *(Panel A)* Samples were analyzed by mass spectrometry by direct infusion. The spectrum of DAR is shown from 500-600 m/z with the dominant peak at 529 m/z as observed for DAR produced by ChuY in Figure 3.4, Panel A. *(Panel B)* Fragmentation of the 529 signal resulted in nearly an identical pattern when compared to DAR from Figure 3.4, Panel B.

References

1 Anbar AD. Oceans. Elements and evolution. Science. 2008;322(5907):1481–3. Available from: http://www.ncbi.nlm.nih.gov/pubmed/19056967.

2 Williams PH. Novel iron uptake system specified by ColV plasmids: an important component in the virulence of invasive strains of Escherichia coli. Infect Immun. 1979;26(3):925–32. Available from: http://www.ncbi.nlm.nih.gov/pubmed/160892.

3 Crosa JH. A plasmid associated with virulence in the marine fish pathogen Vibrio anguillarum specifies an iron-sequestering system. Nature. 1980;284(5756):566–8. Available from: http://www.ncbi.nlm.nih.gov/pubmed/7366725.

4 Mickelsen PA, Sparling PF. Ability of Neisseria gonorrhoeae, Neisseria meningitidis, and commensal Neisseria species to obtain iron from transferrin and iron compounds. Infect Immun. 1981;33(2):555–64. Available from: http://www.ncbi.nlm.nih.gov/pubmed/6792081.

5 Torres AG, Redford P, Welch RA, Payne SM. TonB-dependent systems of uropathogenic Escherichia coli: aerobactin and heme transport and TonB are required for virulence in the mouse. Infect Immun. 2001;69(10):6179–85. Available from: http://www.ncbi.nlm.nih.gov/pubmed/11553558. doi:10.1128/IAI.69.10.6179-6185.2001.

6 Henderson DP, Payne SM. Vibrio cholerae iron transport systems: roles of heme and siderophore iron transport in virulence and identification of a gene associated with multiple iron transport systems. Infect Immun. 1994;62(11):5120–5.

7 Duncan SH, Louis P, Flint HJ. Cultivable bacterial diversity from the human colon. Lett Appl Microbiol. 2007;44(4):343–50. Available from: http://www.ncbi.nlm.nih.gov/pubmed/17397470. doi:10.1111/j.1472-765X.2007.02129.x.

8 Suits MD, Pal GP, Nakatsu K, Matte A, Cygler M, Jia Z. Identification of an Escherichia coli O157:H7 heme oxygenase with tandem functional repeats. Proc Natl Acad Sci U S A. 2005;102(47):16955–60. Available from: http://www.ncbi.nlm.nih.gov/pubmed/16275907. doi:10.1073/pnas.0504289102.

9 Wyckoff EE, Schmitt M, Wilks A, Payne SM. HutZ is required for efficient heme utilization in Vibrio cholerae. J Bacteriol. 2004;186(13):4142–51. doi:10.1128/JB.186.13.4142-4151.2004.

10 Wilks A, Ikeda-Saito M. Heme utilization by pathogenic bacteria: not all pathways lead to biliverdin. Acc Chem Res. 2014;47(8):2291–8. doi:10.1021/ar500028n.

11 Ponka P. Cell biology of heme. Am J Med Sci. 1999;318(4):241–56. Available from: http://www.ncbi.nlm.nih.gov/pubmed/10522552.

12 Anzaldi LL, Skaar EP. Overcoming the heme paradox: heme toxicity and tolerance in bacterial pathogens. Infect Immun. 2010;78(12):4977–89. doi:10.1128/IAI.00613-10.

13 Simpson W, Wang CY, Mikolajczyk-Pawlinska J, Potempa J, Travis J, Bond VC, et al. Transposition of the endogenous insertion sequence element IS1126 modulates gingipain expression in Porphyromonas gingivalis. Infect Immun. 1999;67(10):5012–20. Available from: http://www.ncbi.nlm.nih.gov/pubmed/10496872.

14 Otto BR, van Dooren SJ, Nuijens JH, Luirink J, Oudega B. Characterization of a hemoglobin protease secreted by the pathogenic Escherichia coli strain EB1. J Exp Med. 1998;188(6):1091–1103. Available from: http://www.ncbi.nlm.nih.gov/pubmed/9743528.

15 Singer ST, Quirolo K, Nishi K, Hackney-Stephens E, Evans C, Vichinsky EP. Erythrocytapheresis for chronically transfused children with sickle cell disease: an effective method for maintaining a low hemoglobin S level and reducing iron overload. J Clin Apher. 1999;14(3):122–5. Available from: http://www.ncbi.nlm.nih.gov/pubmed/10540366.

16 Lewis LA, Sung MH, Gipson M, Hartman K, Dyer DW. Transport of intact porphyrin by HpuAB, the hemoglobin-haptoglobin utilization system of Neisseria meningitidis. J Bacteriol. 1998;180(22):6043–7. Available from: http://www.ncbi.nlm.nih.gov/pubmed/9811666.

17 Hrkal Z, Vodrazka Z, Kalousek I. Transfer of heme from ferrihemoglobin and ferrihemoglobin isolated chains to hemopexin. Eur J Biochem. 1974;43(1):73–8. Available from: http://www.ncbi.nlm.nih.gov/pubmed/4209590.

18 Hanson MS, Hansen EJ. Molecular cloning, partial purification, and characterization of a haemin-binding lipoprotein from Haemophilus influenzae type b. Mol Microbiol. 1991;5(2):267–78. Available from: http://www.ncbi.nlm.nih.gov/pubmed/2041470.

19 Cope LD, Yogev R, Muller-Eberhard U, Hansen EJ. A gene cluster involved in the utilization of both free heme and heme:hemopexin by Haemophilus influenzae type b. J Bacteriol. 1995;177(10):2644–53.

20 Fournier C, Smith A, Delepelaire P. Haem release from haemopexin by HxuA allows Haemophilus influenzae to escape host nutritional immunity. Mol Microbiol. 2011;80(1):133–48. Available from: http://www.ncbi.nlm.nih.gov/pubmed/21276097. doi:10.1111/j.1365-2958.2011.07562.x.

21 Dockal M, Carter DC, Ruker F. The three recombinant domains of human serum albumin. Structural characterization and ligand binding properties. J Biol Chem. 1999;274(41):29303–10. Available from: http://www.ncbi.nlm.nih.gov/pubmed/10506189.

22 Tenhunen R. The enzymatic degradation of heme. Semin Hematol. 1972;9(1):19–29. Available from: http://www.ncbi.nlm.nih.gov/pubmed/4550942.

23 Tenhunen R, Marver HS, Schmid R. The enzymatic conversion of heme to bilirubin by microsomal heme oxygenase. Proc Natl Acad Sci U S A. 1968;61(2):748–55.

24 Wong KP. Bilirubin glucuronyltransferase. Specific assay and kinetic studies. Biochem J. 1971;125(1):27–35. Available from: http://www.ncbi.nlm.nih.gov/pubmed/5158913.

25 Tenhunen R, Marver HS, Schmid R. Microsomal heme oxygenase. Characterization of the enzyme. J Biol Chem. 1969;244(23):6388–94.

26 Yoshida T, Kikuchi G. Reaction of the microsomal heme oxygenase with cobaltic protoporphyrin IX, and extremely poor substrate. J Biol Chem. 1978;253(23):8479–82. Available from: http://www.ncbi.nlm.nih.gov/pubmed/101544.

27 Takahashi S, Wang J, Rousseau DL, Ishikawa K, Yoshida T, Host JR, et al. Heme-heme oxygenase complex. Structure of the catalytic site and its implication for oxygen activation. J Biol Chem. 1994;269(2):1010–4. Available from: http://www.ncbi.nlm.nih.gov/pubmed/8288555.

28 Takahashi S, Wang J, Rousseau DL, Ishikawa K, Yoshida T, Takeuchi N, et al. Heme-heme oxygenase complex: structure and properties of the catalytic site from resonance Raman scattering. Biochemistry. 1994;33(18):5531–8. Available from: http://www.ncbi.nlm.nih.gov/pubmed/8180175.

29 Sun J, Wilks A, Ortiz de Montellano PR, Loehr TM. Resonance Raman and EPR spectroscopic studies on heme-heme oxygenase complexes. Biochemistry. 1993;32(51):14151–7. Available from: http://www.ncbi.nlm.nih.gov/pubmed/8260499.

30 Sun J, Loehr TM, Wilks A, Ortiz de Montellano PR. Identification of histidine 25 as the heme ligand in human liver heme oxygenase. Biochemistry. 1994;33(46):13734–40. Available from: http://www.ncbi.nlm.nih.gov/pubmed/7947784.

31 Wilks A, Ortiz de Montellano PR, Sun J, Loehr TM. Heme oxygenase (HO-1): His-132 stabilizes a distal water ligand and assists catalysis. Biochemistry. 1996;35(3):930–6. Available from: http://www.ncbi.nlm.nih.gov/pubmed/8547275. doi:10.1021/bi952405f.

32 Matera KM, Zhou H, Migita CT, Hobert SE, Ishikawa K, Katakura K, et al. Histidine-132 does not stabilize a distal water ligand and is not an important residue for the enzyme activity in heme oxygenase-1. Biochemistry. 1997;36(16):4909–15. Available from: http://www.ncbi.nlm.nih.gov/pubmed/9125512. doi:10.1021/bi962321m.

33 Schmitt MP. Utilization of host iron sources by Corynebacterium diphtheriae: identification of a gene whose product is homologous to eukaryotic heme oxygenases and is required for acquisition of iron from heme and hemoglobin. J Bacteriol. 1997;179(3):838–45.

34 Schmitt MP. Transcription of the Corynebacterium diphtheriae hmuO gene is regulated by iron and heme. Infect Immun. 1997;65(11):4634–41.

35 Chu GC, Katakura K, Tomita T, Zhang X, Sun D, Sato M, et al. Histidine 20, the crucial proximal axial heme ligand of bacterial heme oxygenase Hmu O from Corynebacterium diphtheriae. J Biol Chem. 2000;275(23):17494–500. doi:10.1074/jbc.M000830200.

36 Wilks A, Moenne-Loccoz P. Identification of the proximal ligand His-20 in heme oxygenase (Hmu O) from Corynebacterium diphtheriae. Oxidative cleavage of the heme macrocycle does not require the proximal histidine. J Biol Chem. 2000;275(16):11686–92. Available from: http://www.ncbi.nlm.nih.gov/pubmed/10766788.

37 Unno M, Matsui T, Chu GC, Couture M, Yoshida T, Rousseau DL, et al. Crystal structure of the dioxygen-bound heme oxygenase from Corynebacterium diphtheriae: implications for heme oxygenase function. J Biol Chem. 2004;279(20):21055–61. Available from: http://www.ncbi.nlm.nih.gov/pubmed/14966119. doi:10.1074/jbc.M400491200.

38 Friedman J, Lad L, Deshmukh R, Li H, Wilks A, Poulos TL. Crystal structures of the NO- and CO-bound heme oxygenase from Neisseriae meningitidis. Implications for O2 activation. J Biol Chem. 2003;278(36):34654–9. Available from: http://www.ncbi.nlm.nih.gov/pubmed/12819228. doi:10.1074/jbc.M302985200.

39 Liu Y, Koenigs Lightning L, Huang H, Moenne-Loccoz P, Schuller DJ, Poulos TL, et al. Replacement of the distal glycine 139 transforms human heme oxygenase-1 into a peroxidase. J Biol Chem. 2000;275(44):34501–7. Available from: http://www.ncbi.nlm.nih.gov/pubmed/10942763. doi:10.1074/jbc.M004245200.

40 Tasler R, Moises T, Frankenberg-Dinkel N. Biochemical and spectroscopic characterization of the bacterial phytochrome of Pseudomonas aeruginosa. FEBS J. 2005;272(8):1927–36. doi:10.1111/j.1742-4658.2005.04623.x.

41 Yoshida T, Kikuchi G. Purification and properties of heme oxygenase from rat liver microsomes. J Biol Chem. 1979;254(11):4487–91. Available from: http://www.ncbi.nlm.nih.gov/pubmed/438202.

42 Schuller DJ, Wilks A, Ortiz de Montellano PR, Poulos TL. Crystal structure of human heme oxygenase-1. Nat Struct Biol. 1999;6(9):860–7. doi:10.1038/12319.

43 Davydov RM, Yoshida T, Ikeda-Saito M, Hoffman BM. Hydroperoxy-Heme Oxygenase generated by cryreduction catalyzes the formation of α-*meso*-hydroxyheme as detected by EPR and ENDOR. J Am Chem Soc. 1999;121(45):10656–57. doi:10.1021/ja99245v.

44 Liu Y, Ortiz de Montellano PR. Reaction intermediates and single turnover rate constants for the oxidation of heme by human heme oxygenase-1. J Biol Chem. 2000;275(8):5297–307. Available from: http://www.ncbi.nlm.nih.gov/pubmed/10681502.

45 Lad L, Ortiz de Montellano PR, Poulos TL. Crystal structures of ferrous and ferrous-NO forms of verdoheme in a complex with human heme oxygenase-1: catalytic implications for heme cleavage. J Inorg Biochem. 2004;98(11):1686–95. Available from: http://www.ncbi.nlm.nih.gov/pubmed/15522396. doi:10.1016/j.jinorgbio.2004.07.004.

46 Sato H, Sugishima M, Sakamoto H, Higashimoto Y, Shimokawa C, Fukuyama K, et al. Crystal structure of rat haem oxygenase-1 in complex with ferrous verdohaem: presence of a hydrogen-bond network on the distal side. Biochem J. 2009;419(2):339–45. Available from: http://www.ncbi.nlm.nih.gov/pubmed/19154182. doi:10.1042/BJ20082279.

47 Matsui T, Nakajima A, Fujii H, Matera KM, Migita CT, Yoshida T, et al. O(2)- and H(2)O(2)-dependent verdoheme degradation by heme oxygenase: reaction mechanisms and potential physiological roles of the dual pathway degradation. J Biol Chem. 2005;280(44):36833–40. Available from: http://www.ncbi.nlm.nih.gov/pubmed/16115896. doi:10.1074/jbc.M503529200.

48 Ratliff M, Zhu W, Deshmukh R, Wilks A, Stojiljkovic I. Homologues of neisserial heme oxygenase in gram-negative bacteria: degradation of heme by the product of the pigA gene of Pseudomonas aeruginosa. J Bacteriol. 2001;183(21):6394–403. doi:10.1128/JB.183.21.6394-6403.2001.

49 Friedman J, Lad L, Li H, Wilks A, Poulos TL. Structural basis for novel delta-regioselective heme oxygenation in the opportunistic pathogen Pseudomonas aeruginosa. Biochemistry. 2004;43(18):5239–45. doi:10.1021/bi049687g.

50 Hernandez G, Wilks A, Paolesse R, Smith KM, Ortiz de Montellano PR, La Mar GN. Proton NMR investigation of substrate-bound heme oxygenase: evidence for electronic and steric contributions to stereoselective heme cleavage. Biochemistry. 1994;33(21):6631–41.

51 Wu R, Skaar EP, Zhang R, Joachimiak G, Gornicki P, Schneewind O, et al. Staphylococcus aureus IsdG and IsdI, heme-degrading enzymes with structural similarity to monooxygenases. J Biol Chem. 2005;280(4):2840–6. doi:10.1074/jbc.M409526200.

52 Reniere ML, Skaar EP. Staphylococcus aureus haem oxygenases are differentially regulated by iron and haem. Mol Microbiol. 2008;69(5):1304–15. doi:10.1111/j.1365-2958.2008.06363.x.

53 Reniere ML, Ukpabi GN, Harry SR, Stec DF, Krull R, Wright DW, et al. The IsdG-family of haem oxygenases degrades haem to a novel chromophore. Mol Microbiol. 2010;75(6):1529–38. doi:10.1111/j.1365-2958.2010.07076.x.

54 Matsui T, Nambu S, Ono Y, Goulding CW, Tsumoto K, Ikeda-Saito M. Heme degradation by Staphylococcus aureus IsdG and IsdI liberates formaldehyde rather than carbon monoxide. Biochemistry. 2013;52(18):3025–7. doi:10.1021/bi400382p.

55 Nobre LS, Seixas JD, Romao CC, Saraiva LM. Antimicrobial action of carbon monoxide-releasing compounds. Antimicrob Agents Chemother. 2007;51(12):4303–7. Available from: http://www.ncbi.nlm.nih.gov/pubmed/17923486. doi:10.1128/AAC.00802-07.

56 Lee WC, Reniere ML, Skaar EP, Murphy ME. Ruffling of metalloporphyrins bound to IsdG and IsdI, two heme-degrading enzymes in Staphylococcus aureus. J Biol Chem. 2008;283(45):30957–63. doi:10.1074/jbc.M709486200.

57 Lockhart CL, Conger MA, Pittman DS, Liptak MD. Hydrogen bond donation to the heme distal ligand of Staphylococcus aureus IsdG tunes the electronic structure. J Biol Inorg Chem. 2015;20(5):757–70. Available from: http://www.ncbi.nlm.nih.gov/pubmed/25911498. doi:10.1007/s00775-015-1263-5.

58 Chim N, Iniguez A, Nguyen TQ, Goulding CW. Unusual diheme conformation of the heme-degrading protein from Mycobacterium tuberculosis. J Mol Biol. 2010;395(3):595–608. Available from: http://www.ncbi.nlm.nih.gov/pubmed/19917297. doi:10.1016/j.jmb.2009.11.025.

59 Nambu S, Matsui T, Goulding CW, Takahashi S, Ikeda-Saito M. A new way to degrade heme: the Mycobacterium tuberculosis enzyme MhuD catalyzes heme degradation without generating CO. J Biol Chem. 2013;288(14):10101–9. doi:10.1074/jbc.M112.448399.

60 Kumar A, Deshane JS, Crossman DK, Bolisetty S, Yan BS, Kramnik I, et al. Heme oxygenase-1-derived carbon monoxide induces the Mycobacterium tuberculosis dormancy regulon. J Biol Chem. 2008;283(26):18032–9. Available from: http://www.ncbi.nlm.nih.gov/pubmed/18400743. doi:10.1074/jbc.M802274200.

61 Shiloh MU, Manzanillo P, Cox JS. Mycobacterium tuberculosis senses host-derived carbon monoxide during macrophage infection. Cell Host Microbe. 2008;3(5):323–30. Available from: http://www.ncbi.nlm.nih.gov/pubmed/18474359. doi:10.1016/j.chom.2008.03.007.

62 Graves AB, Morse RP, Chao A, Iniguez A, Goulding CW, Liptak MD. Crystallographic and Spectroscopic Insights into Heme Degradation by Mycobacterium tuberculosis MhuD. Inorganic Chemistry. 2014;53(12):5931–5940. Available from: <GotoISI>://WOS:000337557800013. doi:10.1021/ic500033b.

63 Stojiljkovic I, Hantke K. Transport of haemin across the cytoplasmic membrane through a haemin-specific periplasmic binding-protein-dependent transport system in Yersinia enterocolitica. Mol Microbiol. 1994;13(4):719–32.

64 Lansky IB, Lukat-Rodgers GS, Block D, Rodgers KR, Ratliff M, Wilks A. The cytoplasmic heme-binding protein (PhuS) from the heme uptake system of Pseudomonas aeruginosa is an intracellular heme-trafficking protein to the delta-regioselective heme oxygenase. J Biol Chem. 2006;281(19):13652–62. Available from: http://www.ncbi.nlm.nih.gov/pubmed/16533806. doi:10.1074/jbc.M600824200.

65 O'Neill MJ, Bhakta MN, Wilks A. Induced fit on heme binding to the Pseudomonas aeruginosa cytoplasmic protein (PhuS) drives interaction with heme oxygenase (HemO). Proc Natl Acad Sci U S A. 2012;109(15):5639–44. doi:10.1073/pnas.1121549109.

66 O'Neill MJ, Wilks A. The P. aeruginosa heme binding protein PhuS is a heme oxygenase titratable regulator of heme uptake. ACS Chem Biol. 2013;8(8):1794–802. doi:10.1021/cb400165b.

67 Lee MJ, Schep D, McLaughlin B, Kaufmann M, Jia Z. Structural analysis and identification of PhuS as a heme-degrading enzyme from Pseudomonas aeruginosa. J Mol Biol. 2014;426(9):1936–46. doi:10.1016/j.jmb.2014.02.013.

68 Suits MD, Jaffer N, Jia Z. Structure of the Escherichia coli O157:H7 heme oxygenase ChuS in complex with heme and enzymatic inactivation by mutation of the heme coordinating residue His-193. J Biol Chem. 2006;281(48):36776–82. doi:10.1074/jbc.M607684200.

69 Ouellet YH, Ndiaye CT, Gagne SM, Sebilo A, Suits MD, Jubinville E, et al. An alternative reaction for heme degradation catalyzed by the Escherichia coli O157:H7 ChuS protein: Release of hematinic acid, tripyrrole and Fe(III). J Inorg Biochem. 2016;154:103–13. Available from: http://www.ncbi.nlm.nih.gov/pubmed/26598215. doi:10.1016/j.jinorgbio.2015.11.002.

70 Allen CE, Schmitt MP. HtaA is an iron-regulated hemin binding protein involved in the utilization of heme iron in Corynebacterium diphtheriae. J Bacteriol. 2009;191(8):2638–48. Available from: http://www.ncbi.nlm.nih.gov/pubmed/19201805. doi:10.1128/JB.01784-08.

71 Torres AG, Payne SM. Haem iron-transport system in enterohaemorrhagic Escherichia coli O157:H7. Mol Microbiol. 1997;23(4):825–33. Available from: http://www.ncbi.nlm.nih.gov/pubmed/9157252.

72 Hagan EC, Mobley HL. Haem acquisition is facilitated by a novel receptor Hma and required by uropathogenic Escherichia coli for kidney infection. Mol Microbiol. 2009;71(1):79–91. Available from: http://www.ncbi.nlm.nih.gov/pubmed/19019144. doi:10.1111/j.1365-2958.2008.06509.x.

73 Jin H, Ren Z, Whitby PW, Morton DJ, Stull TL. Characterization of hgpA, a gene encoding a haemoglobin/haemoglobin-haptoglobin-binding protein of Haemophilus influenzae. Microbiology. 1999;145 (Pt 4):905–14. Available from: http://www.ncbi.nlm.nih.gov/pubmed/10220170. doi:10.1099/13500872-145-4-905.

74 Ren Z, Jin H, Morton DJ, Stull TL. hgpB, a gene encoding a second Haemophilus influenzae hemoglobin- and hemoglobin-haptoglobin-binding protein. Infect Immun. 1998;66(10):4733–41. Available from: http://www.ncbi.nlm.nih.gov/pubmed/9746572.

75 Cope LD, Thomas SE, Latimer JL, Slaughter CA, Muller-Eberhard U, Hansen EJ. The 100 kDa haem:haemopexin-binding protein of Haemophilus influenzae: structure and localization. Mol Microbiol. 1994;13(5):863–73.

76 Lewis LA, Gray E, Wang YP, Roe BA, Dyer DW. Molecular characterization of hpuAB, the haemoglobin-haptoglobin-utilization operon of Neisseria meningitidis. Mol Microbiol. 1997;23(4):737–49.

77 Stojiljkovic I, Hwa V, de Saint Martin L, O'Gaora P, Nassif X, Heffron F, et al. The Neisseria meningitidis haemoglobin receptor: its role in iron utilization and virulence. Mol Microbiol. 1995;15(3):531–41. Available from: http://www.ncbi.nlm.nih.gov/pubmed/7783623.

78 Simpson W, Olczak T, Genco CA. Characterization and expression of HmuR, a TonB-dependent hemoglobin receptor of Porphyromonas gingivalis. J Bacteriol. 2000;182(20):5737–48. Available from: http://www.ncbi.nlm.nih.gov/pubmed/11004172.

79 Karunakaran T, Madden T, Kuramitsu H. Isolation and characterization of a hemin-regulated gene, hemR, from Porphyromonas gingivalis. J Bacteriol. 1997;179(6):1898–908. Available from: http://www.ncbi.nlm.nih.gov/pubmed/9068634.

80 Ochsner UA, Johnson Z, Vasil ML. Genetics and regulation of two distinct haem-uptake systems, phu and has, in Pseudomonas aeruginosa. Microbiology. 2000;146 (Pt 1):185–98. Available from: http://www.ncbi.nlm.nih.gov/pubmed/10658665. doi:10.1099/00221287-146-1-185.

81 Smith AD, Wilks A. Differential contributions of the outer membrane receptors PhuR and HasR to heme acquisition in Pseudomonas aeruginosa. J Biol Chem. 2015;290(12):7756–66. Available from: http://www.ncbi.nlm.nih.gov/pubmed/25616666. doi:10.1074/jbc.M114.633495.

82 Mills M, Payne SM. Identification of shuA, the gene encoding the heme receptor of Shigella dysenteriae, and analysis of invasion and intracellular multiplication of a shuA mutant. Infect Immun. 1997;65(12):5358–63. Available from: http://www.ncbi.nlm.nih.gov/pubmed/9393841.

83 Ghigo JM, Letoffe S, Wandersman C. A new type of hemophore-dependent heme acquisition system of Serratia marcescens reconstituted in Escherichia coli. J Bacteriol. 1997;179(11):3572–9. Available from: http://www.ncbi.nlm.nih.gov/pubmed/9171402.

84 Henderson DP, Payne SM. Characterization of the Vibrio cholerae outer membrane heme transport protein HutA: sequence of the gene, regulation of expression, and homology to the family of TonB-dependent proteins. J Bacteriol. 1994;176(11):3269–77. Available from: http://www.ncbi.nlm.nih.gov/pubmed/8195082.

85 Mey AR, Payne SM. Haem utilization in Vibrio cholerae involves multiple TonB-dependent haem receptors. Mol Microbiol. 2001;42(3):835–49.

86 Thompson JM, Jones HA, Perry RD. Molecular characterization of the hemin uptake locus (hmu) from Yersinia pestis and analysis of hmu mutants for hemin and hemoprotein utilization. Infect Immun. 1999;67(8):3879–92. Available from: http://www.ncbi.nlm.nih.gov/pubmed/10417152.

87 Stojiljkovic I, Hantke K. Hemin uptake system of Yersinia enterocolitica: similarities with other TonB-dependent systems in gram-negative bacteria. EMBO J. 1992;11(12):4359–67. Available from: http://www.ncbi.nlm.nih.gov/pubmed/1425573.

88 Omura T, Sato R. A new cytochrome in liver microsomes. J Biol Chem. 1962;237:1375–6. Available from: http://www.ncbi.nlm.nih.gov/pubmed/14482007.

89 Rittle J, Green MT. Cytochrome P450 compound I: capture, characterization, and C-H bond activation kinetics. Science. 2010;330(6006):933–7. Available from: http://www.ncbi.nlm.nih.gov/pubmed/21071661. doi:10.1126/science.1193478.

90 Rutter R, Hager LP, Dhonau H, Hendrich M, Valentine M, Debrunner P. Chloroperoxidase compound I: Electron paramagnetic resonance and Mossbauer studies. Biochemistry. 1984;23(26):6809–16. Available from: http://www.ncbi.nlm.nih.gov/pubmed/6099143.

91 Egawa T, Miki H, Ogura T, Makino R, Ishimura Y, Kitagawa T. Observation of the FeIV=O stretching Raman band for a thiolate-ligated heme protein. Compound I of chloroperoxidase. FEBS Lett. 1992;305(3):206–8. Available from: http://www.ncbi.nlm.nih.gov/pubmed/1299616.

92 Frey PA, Abeles RH. The role of the B12 coenzyme in the conversion of 1,2-propanediol to propionaldehyde. J Biol Chem. 1966;241(11):2732–3. Available from: http://www.ncbi.nlm.nih.gov/pubmed/5911645.

93 Sofia HJ, Chen G, Hetzler BG, Reyes-Spindola JF, Miller NE. Radical SAM, a novel protein superfamily linking unresolved steps in familiar biosynthetic pathways with radical mechanisms: functional characterization using new analysis and information visualization methods. Nucleic Acids Res. 2001;29(5):1097–106.

94 Pegg SC, Brown SD, Ojha S, Seffernick J, Meng EC, Morris JH, et al. Leveraging enzyme structure-function relationships for functional inference and experimental design: the structure-function linkage database. Biochemistry. 2006;45(8):2545–55. doi:10.1021/bi052101l.

95 Chirpich TP, Zappia V, Costilow RN, Barker HA. Lysine 2,3-aminomutase. Purification and properties of a pyridoxal phosphate and S-adenosylmethionine-activated enzyme. J Biol Chem. 1970;245(7):1778–89.

96 Zappia V, Barker HA. Studies on lysine-2,3-aminomutase. Subunit structure and sulfhydryl groups. Biochim Biophys Acta. 1970;207(3):505–13.

97 Aberhart DJ, Gould SJ, Lin HJ, Thiruvengadam TK, Wieiller BH. Stereochemistry of lysine 2,3-aminomutase isolated from Clostridium subterminale strain SB4 [Journal Article]. J Am Chem Soc. 1983;105(16):5461–5470. doi:10.1021/ja00354a046.

98 Frey PA. Lysine 2,3-aminomutase: is adenosylmethionine a poor man's adenosylcobalamin? FASEB J. 1993;7(8):662–70.

99 Moss M, Frey PA. The role of S-adenosylmethionine in the lysine 2,3-aminomutase reaction. J Biol Chem. 1987;262(31):14859–62.

100 Buckel W, Golding BT. Radical enzymes in anaerobes. Annu Rev Microbiol. 2006;60:27–49. Available from: http://www.ncbi.nlm.nih.gov/pubmed/16704345. doi:10.1146/annurev.micro.60.080805.142216.

101 Utter MF, Wood HG, Reiner JM. Anaerobic glycolysis in nervous tissue. J Biol Chem. 1945;161:197–217.

102 Knappe J, Neugebauer FA, Blaschkowski HP, Ganzler M. Post-translational activation introduces a free radical into pyruvate formate-lyase. Proc Natl Acad Sci U S A. 1984;81(5):1332–5.

103 Barlow T. Evidence for a new ribonucleotide reductase in anaerobic E. coli. Biochem Biophys Res Commun. 1988;155(2):747–53.

104 Raynaud C, Sarcabal P, Meynial-Salles I, Croux C, Soucaille P. Molecular characterization of the 1,3-propanediol (1,3-PD) operon of Clostridium butyricum. Proc Natl Acad Sci U S A. 2003;100(9):5010–5. Available from: http://www.ncbi.nlm.nih.gov/pubmed/12704244. doi:10.1073/pnas.0734105100.

105 Yu L, Blaser M, Andrei PI, Pierik AJ, Selmer T. 4-Hydroxyphenylacetate decarboxylases: properties of a novel subclass of glycyl radical enzyme systems. Biochemistry. 2006;45(31):9584–92. Available from: http://www.ncbi.nlm.nih.gov/pubmed/16878993. doi:10.1021/bi060840b.

106 Leuthner B, Leutwein C, Schulz H, Horth P, Haehnel W, Schiltz E, et al. Biochemical and genetic characterization of benzylsuccinate synthase from Thauera aromatica: a new glycyl radical enzyme catalysing the first step in anaerobic toluene metabolism. Mol Microbiol. 1998;28(3):615–28. Available from: http://www.ncbi.nlm.nih.gov/pubmed/9632263.

107 Frey PA, Magnusson OT. S-Adenosylmethionine: a wolf in sheep's clothing, or a rich man's adenosylcobalamin? Chem Rev. 2003;103(6):2129–48. doi:10.1021/cr020422m.

108 Petrovich RM, Ruzicka FJ, Reed GH, Frey PA. Characterization of iron-sulfur clusters in lysine 2,3-aminomutase by electron paramagnetic resonance spectroscopy. Biochemistry. 1992;31(44):10774–81.

109 Lieder KW, Booker S, Ruzicka FJ, Beinert H, Reed GH, Frey PA. S-Adenosylmethionine-dependent reduction of lysine 2,3-aminomutase and observation of the catalytically functional iron-sulfur centers by electron paramagnetic resonance. Biochemistry. 1998;37(8):2578–85. doi:10.1021/bi972417w.

110 Magnusson OT, Reed GH, Frey PA. Characterization of an allylic analogue of the 5'-deoxyadenosyl radical: an intermediate in the reaction of lysine 2,3-aminomutase. Biochemistry. 2001;40(26):7773–82. Available from: http://www.ncbi.nlm.nih.gov/pubmed/11425303.

111 Nicolet Y, Drennan CL. AdoMet radical proteins–from structure to evolution–alignment of divergent protein sequences reveals strong secondary structure element conservation. Nucleic Acids Res. 2004;32(13):4015–25. doi:10.1093/nar/gkh728.

112 Frey PA, Hegeman AD, Ruzicka FJ. The Radical SAM Superfamily. Crit Rev Biochem Mol Biol. 2008;43(1):63–88. doi:10.1080/10409230701829169.

113 Farrar CE, Siu KK, Howell PL, Jarrett JT. Biotin synthase exhibits burst kinetics and multiple turnovers in the absence of inhibition by products and product-related biomolecules. Biochemistry. 2010;49(46):9985–96. doi:10.1021/bi101023c.

114 Bruender NA, Young AP, Bandarian V. Chemical and Biological Reduction of the Radical SAM Enzyme CPH4 Synthase. Biochemistry. 2015;54(18):2903–10. Available from: http://www.ncbi.nlm.nih.gov/pubmed/25933252. doi:10.1021/acs.biochem.5b00210.

115 Berkovitch F, Nicolet Y, Wan JT, Jarrett JT, Drennan CL. Crystal structure of biotin synthase, an S-adenosylmethionine-dependent radical enzyme. Science. 2004;303(5654):76–9. Available from: http://www.ncbi.nlm.nih.gov/pubmed/14704425. doi:10.1126/science.1088493.

116 Chatterjee A, Li Y, Zhang Y, Grove TL, Lee M, Krebs C, et al. Reconstitution of ThiC in thiamine pyrimidine biosynthesis expands the radical SAM superfamily. Nat Chem Biol. 2008;4(12):758–65. Available from: http://www.ncbi.nlm.nih.gov/pubmed/18953358. doi:10.1038/nchembio.121.

117 Nicolet Y, Rubach JK, Posewitz MC, Amara P, Mathevon C, Atta M, et al. X-ray structure of the [FeFe]-hydrogenase maturase HydE from Thermotoga maritima. J Biol Chem. 2008;283(27):18861–72. Available from: http://www.ncbi.nlm.nih.gov/pubmed/18400755. doi:10.1074/jbc.M801161200.

118 Dailey HA, Gerdes S, Dailey TA, Burch JS, Phillips JD. Noncanonical coproporphyrin-dependent bacterial heme biosynthesis pathway that does not use protoporphyrin. Proc Natl Acad Sci U S A. 2015;112(7):2210–5. Available from: http://www.ncbi.nlm.nih.gov/pubmed/25646457. doi:10.1073/pnas.1416285112.

119 Tait GH. Coproporphyrinogenase activity in extracts from Rhodopseudomonas spheroides. Biochem Biophys Res Commun. 1969;37(1):116–22. Available from: http://www.ncbi.nlm.nih.gov/pubmed/5346353.

120 Tait GH. Coproporphyrinogenase activities in extracts of Rhodopseudomonas spheroides and Chromatium strain D. Biochem J. 1972;128(5):1159–69. Available from: http://www.ncbi.nlm.nih.gov/pubmed/4345352.

121 Layer G, Verfurth K, Mahlitz E, Jahn D. Oxygen-independent coproporphyrinogen-III oxidase HemN from Escherichia coli. J Biol Chem. 2002;277(37):34136–42. doi:10.1074/jbc.M205247200.

122 Layer G, Pierik AJ, Trost M, Rigby SE, Leech HK, Grage K, et al. The substrate radical of Escherichia coli oxygen-independent coproporphyrinogen III oxidase HemN. J Biol Chem. 2006;281(23):15727–34. doi:10.1074/jbc.M512628200.

123 Rand K, Noll C, Schiebel HM, Kemken D, Dulcks T, Kalesse M, et al. The oxygen-independent coproporphyrinogen III oxidase HemN utilizes harderoporphyrinogen as a reaction intermediate during conversion of coproporphyrinogen III to protoporphyrinogen IX. Biol Chem. 2010;391(1):55–63. doi:10.1515/BC.2010.006.

124 Layer G, Moser J, Heinz DW, Jahn D, Schubert WD. Crystal structure of coproporphyrinogen III oxidase reveals cofactor geometry of Radical SAM enzymes. EMBO J. 2003;22(23):6214–24. doi:10.1093/emboj/cdg598.

125 Layer G, Grage K, Teschner T, Schunemann V, Breckau D, Masoumi A, et al. Radical S-adenosylmethionine enzyme coproporphyrinogen III oxidase HemN: functional features of the [4Fe-4S] cluster and the two bound S-adenosyl-L-methionines. J Biol Chem. 2005;280(32):29038–46. doi:10.1074/jbc.M501275200.

126 Schnoes AM, Brown SD, Dodevski I, Babbitt PC. Annotation error in public databases: misannotation of molecular function in enzyme superfamilies. PLoS Comput Biol. 2009;5(12):e1000605. Available from: http://www.ncbi.nlm.nih.gov/pubmed/20011109. doi:10.1371/journal.pcbi.1000605.

127 Goto T, Aoki R Fau Minamizaki K, Minamizaki K Fau Fujita Y, Fujita Y. Functional differentiation of two analogous coproporphyrinogen III oxidases for heme and chlorophyll biosynthesis pathways in the cyanobacterium Synechocystis sp. PCC 6803. Plant Cell Physiol. 2010;51(4):650–63. doi:10.1093/pcp/pcq023.

128 Abicht HK, Martinez J, Layer G, Jahn D, Solioz M. Lactococcus lactis HemW (HemN) is a haem-binding protein with a putative role in haem trafficking. Biochem J. 2012;442(2):335–43. doi:10.1042/BJ20111618.

129 Zhang Q, van der Donk Wa Fau Liu W, Liu W. Radical-mediated enzymatic methylation: a tale of two SAMS. Acc Chem Res. 2012;45(4). doi:10.1021/ar200202c.

130 Benitez-Paez A, Villarroya M, Armengod ME. The Escherichia coli RlmN methyltransferase is a dual-specificity enzyme that modifies both rRNA and tRNA and controls translational accuracy. RNA. 2012;18(10):1783–95. Available from: http://www.ncbi.nlm.nih.gov/pubmed/22891362. doi:10.1261/rna.033266.112.

131 Long KS, Poehlsgaard J, Kehrenberg C, Schwarz S, Vester B. The Cfr rRNA methyltransferase confers resistance to Phenicols, Lincosamides, Oxazolidinones, Pleuromutilins, and Streptogramin A antibiotics. Antimicrob Agents Chemother. 2006;50(7):2500–5. doi:10.1128/AAC.00131-06.

132 Schwalm EL, Grove TL, Booker SJ, Boal AK. Crystallographic capture of a radical S-adenosylmethionine enzyme in the act of modifying tRNA. Science. 2016;352(6283):309–12. Available from: http://www.ncbi.nlm.nih.gov/pubmed/27081063. doi:10.1126/science.aad5367.

133 Grove TL, Radle MI, Krebs C, Booker SJ. Cfr and RlmN contain a single [4Fe-4S] cluster, which directs two distinct reactivities for S-adenosylmethionine: methyl transfer by SN2 displacement and radical generation. J Am Chem Soc. 2011;133(49):19586–9. Available from: http://www.ncbi.nlm.nih.gov/pubmed/21916495. doi:10.1021/ja207327v.

134 Boal AK, Grove TL, McLaughlin MI, Yennawar NH, Booker SJ, Rosenzweig AC. Structural basis for methyl transfer by a radical SAM enzyme. Science. 2011;332(6033):1089–92. doi:10.1126/science.1205358.

135 Yan F, Fujimori DG. RNA methylation by radical SAM enzymes RlmN and Cfr proceeds via methylene transfer and hydride shift. Proc Natl Acad Sci U S A. 2011;108(10):3930–4. doi:10.1073/pnas.1017781108.

136 Silakov A, Grove TL, Radle MI, Bauerle MR, Green MT, Rosenzweig AC, et al. Characterization of a cross-linked protein-nucleic acid substrate radical in the reaction catalyzed by RlmN. J Am Chem Soc. 2014;136(23):8221–8. Available from: http://www.ncbi.nlm.nih.gov/pubmed/24806349. doi:10.1021/ja410560p.

137 McCusker KP, Medzihradszky KF, Shiver AL, Nichols RJ, Yan F, Maltby DA, et al. Covalent intermediate in the catalytic mechanism of the radical S-adenosyl-L-methionine methyl synthase RlmN trapped by mutagenesis. J Am Chem Soc. 2012;134(43):18074–81. doi:10.1021/ja307855d.

138 Grove TL, Benner JS, Radle MI, Ahlum JH, Landgraf BJ, Krebs C, et al. A radically different mechanism for S-adenosylmethionine-dependent methyltransferases. Science. 2011;332(6029):604–7. doi:10.1126/science.1200877.

139 Wei Y, Mathies G, Yokoyama K, Chen J, Griffin RG, Stubbe J. A chemically competent thiosulfuranyl radical on the Escherichia coli class III ribonucleotide reductase. J Am Chem Soc. 2014;136(25):9001–13. Available from: http://www.ncbi.nlm.nih.gov/pubmed/24827372. doi:10.1021/ja5030194.

140 Kim HJ, McCarty RM, Ogasawara Y, Liu YN, Mansoorabadi SO, Levieux J, et al. GenK-Catalyzed C-6' Methylation in the Biosynthesis of Gentamicin: Isolation and Characterization of a Cobalamin-Dependent Radical SAM Enzyme. J Am Chem Soc. 2013;135(22):8093–6. doi:10.1021/ja312641f.

141 Blaszczyk AJ, Silakov A, Zhang B, Maiocco SJ, Lanz ND, Kelly WL, et al. Spectroscopic and Electrochemical Characterization of the Iron-Sulfur and Cobalamin Cofactors of TsrM, an Unusual Radical S-Adenosylmethionine Methylase. J Am Chem Soc. 2016;Available from: http://www.ncbi.nlm.nih.gov/pubmed/26841310. doi:10.1021/jacs.5b12592.

142 Hoerlein G. Glufosinate (phosphinothricin), a natural amino acid with unexpected herbicidal properties. Rev Environ Contam Toxicol. 1994;138:73–145. Available from: http://www.ncbi.nlm.nih.gov/pubmed/7938785.

143 Werner WJ, Allen KD, Hu K, Helms GL, Chen BS, Wang SC. In vitro phosphinate methylation by PhpK from Kitasatospora phosalacinea. Biochemistry. 2011;50(42):8986–8. doi:10.1021/bi201220r.

144 Allen KD, Wang SC. Initial characterization of Fom3 from Streptomyces wedmorensis: The methyltransferase in fosfomycin biosynthesis. Arch Biochem Biophys. 2014;543:67–73. Available from: http://www.ncbi.nlm.nih.gov/pubmed/24370735. doi:10.1016/j.abb.2013.12.004.

145 Kuzuyama T, Hidaka T, Kamigiri K, Imai S, Seto H. Studies on the biosynthesis of fosfomycin. 4. The biosynthetic origin of the methyl group of fosfomycin. J Antibiot (Tokyo). 1992;45(11):1812–4. Available from: http://www.ncbi.nlm.nih.gov/pubmed/1468993.

146 Kelly WL, Pan L, Li C. Thiostrepton biosynthesis: prototype for a new family of bacteriocins. J Am Chem Soc. 2009;131(12):4327–34. Available from: http://www.ncbi.nlm.nih.gov/pubmed/19265401. doi:10.1021/ja807890a.

147 Benjdia A, Pierre S, Gherasim C, Guillot A, Carmona M, Amara P, et al. The thiostrepton A tryptophan methyltransferase TsrM catalyses a cob(II)alamin-dependent methyl transfer reaction. Nat Commun. 2015;6:8377. Available from: http://www.ncbi.nlm.nih.gov/pubmed/26456915. doi:10.1038/ncomms9377.

148 Bauerle MR, Schwalm EL, Booker SJ. Mechanistic diversity of radical S-adenosylmethionine (SAM)-dependent methylation. J Biol Chem. 2015;290(7):3995–4002. doi:10.1074/jbc.R114.607044.

149 Pucci MJ, Bronson JJ, Barrett JF, DenBleyker KL, Discotto LF, Fung-Tomc JC, et al. Antimicrobial evaluation of nocathiacins, a thiazole peptide class of antibiotics. Antimicrob Agents Chemother. 2004;48(10):3697–701. Available from: http://www.ncbi.nlm.nih.gov/pubmed/15388422. doi:10.1128/AAC.48.10.3697-3701.2004.

150 Yu Y, Duan L, Zhang Q, Liao R, Ding Y, Pan H, et al. Nosiheptide biosynthesis featuring a unique indole side ring formation on the characteristic thiopeptide framework. ACS Chem Biol. 2009;4(10):855–64. doi:10.1021/cb900133x.

151 Ding Y, Yu Y, Pan H, Guo H, Li Y, Liu W. Moving posttranslational modifications forward to biosynthesize the glycosylated thiopeptide nocathiacin I in Nocardia sp. ATCC202099. Mol Biosyst. 2010;6(7):1180–5. doi:10.1039/c005121g.

152 Watanabe H, Tokiwano T, Oikawa H. Biosynthetic study of FR-900848: unusual observation on polyketide biosynthesis that did not accept acetate as origin of acetyl-CoA. Tet Lett. 2006;47(9):1399–1402.

153 Allen KD, Xu H, White RH. Identification of a unique radical S-adenosylmethionine methylase likely involved in methanopterin biosynthesis in Methanocaldococcus jannaschii. J Bacteriol. 2014;196(18):3315–23. Available from: http://www.ncbi.nlm.nih.gov/pubmed/25002541. doi:10.1128/JB.01903-14.

154 Hippler B, Homuth G, Hoffmann T, Hungerer C, Schumann W, Jahn D. Characterization of Bacillus subtilis hemN. J Bacteriol. 1997;179(22):7181–5. Available from: http://www.ncbi.nlm.nih.gov/pubmed/9371469.

155 Miller JR, Busby RW, Jordan SW, Cheek J, Henshaw TF, Ashley GW, et al. Escherichia coli LipA is a lipoyl synthase: in vitro biosynthesis of lipoylated pyruvate dehydrogenase complex from octanoyl-acyl carrier protein [Journal Article]. Biochemistry. 2000;39(49):15166–78. Available from: http://www.ncbi.nlm.nih.gov/pubmed/11106496.

156 Vey JL, Drennan CL. Structural insights into radical generation by the radical SAM superfamily. Chem Rev. 2011;111(4):2487–506. Available from: http://www.ncbi.nlm.nih.gov/pubmed/21370834. doi:10.1021/cr9002616.

157 Giessing AM, Jensen SS, Rasmussen A, Hansen LH, Gondela A, Long K, et al. Identification of 8-methyladenosine as the modification catalyzed by the radical SAM methyltransferase Cfr that confers antibiotic resistance in bacteria. RNA. 2009;15(2):327–36. Available from: http://www.ncbi.nlm.nih.gov/pubmed/19144912. doi:10.1261/rna.1371409.

158 Toh SM, Xiong L, Bae T, Mankin AS. The methyltransferase YfgB/RlmN is responsible for modification of adenosine 2503 in 23S rRNA. RNA. 2008;14(1):98–106. doi:10.1261/rna.814408.

159 Allen KD, Wang SC. Initial characterization of Fom3 from Streptomyces wedmorensis: The methyltransferase in fosfomycin biosynthesis. Arch Biochem Biophys. 2014;543:67–73. Available from: http://www.ncbi.nlm.nih.gov/pubmed/24370735. doi:10.1016/j.abb.2013.12.004.

160 Dairi T, Ohta T, Hashimoto E, Hasegawa M. Organization and nature of fortimicin A (astromicin) biosynthetic genes studied using a cosmid library of Micromonospora olivasterospora DNA. Mol Gen Genet. 1992;236(1):39–48. Available from: http://www.ncbi.nlm.nih.gov/pubmed/1494349.

161 Marous DR, Lloyd EP, Buller AR, Moshos KA, Grove TL, Blaszczyk AJ, et al. Consecutive radical S-adenosylmethionine methylations form the ethyl side chain in thienamycin biosynthesis. Proc Natl Acad Sci U S A. 2015;112(33):10354–8. Available from: http://www.ncbi.nlm.nih.gov/pubmed/26240322. doi:10.1073/pnas.1508615112.

162 Zhang W, Ostash B, Walsh CT. Identification of the biosynthetic gene cluster for the pacidamycin group of peptidyl nucleoside antibiotics. Proc Natl Acad Sci U S A. 2010;107(39):16828–33. Available from: http://www.ncbi.nlm.nih.gov/pubmed/20826445. doi:10.1073/pnas.1011557107.

163 Rachid S, Scharfe M, Blocker H, Weissman KJ, Muller R. Unusual chemistry in the biosynthesis of the antibiotic chondrochlorens. Chem Biol. 2009;16(1):70–81. Available from: http://www.ncbi.nlm.nih.gov/pubmed/19171307. doi:10.1016/j.chembiol.2008.11.005.

164 Watanabe K, Hotta K, Nakaya M, Praseuth AP, Wang CC, Inada D, et al. Escherichia coli allows efficient modular incorporation of newly isolated quinomycin biosynthetic enzyme into echinomycin biosynthetic pathway for rational design and synthesis of potent antibiotic unnatural natural product. J Am Chem Soc. 2009;131(26):9347–53. Available from: http://www.ncbi.nlm.nih.gov/pubmed/19514719. doi:10.1021/ja902261a.

165 Gomez Maqueo Chew A, Frigaard NU, Bryant DA. Bacteriochlorophyllide c C-8(2) and C-12(1) methyltransferases are essential for adaptation to low light in Chlorobaculum tepidum. J Bacteriol. 2007;189(17):6176–84. Available from: http://www.ncbi.nlm.nih.gov/pubmed/17586634. doi:10.1128/JB.00519-07.

166 Funabashi M, Yang Z, Nonaka K, Hosobuchi M, Fujita Y, Shibata T, et al. An ATP-independent strategy for amide bond formation in antibiotic biosynthesis. Nat Chem Biol. 2010;6(8):581–6. Available from: http://www.ncbi.nlm.nih.gov/pubmed/20562876. doi:10.1038/nchembio.393.

167 Westrich L, Heide L, Li SM. CloN6, a novel methyltransferase catalysing the methylation of the pyrrole-2-carboxyl moiety of clorobiocin. Chembiochem. 2003;4(8):768–73. doi:10.1002/cbic.200300609.

168 Wang ZX, Li SM, Heide L. Identification of the coumermycin A(1) biosynthetic gene cluster of Streptomyces rishiriensis DSM 40489. Antimicrob Agents Chemother. 2000;44(11):3040–8. Available from: http://www.ncbi.nlm.nih.gov/pubmed/11036020.

169 Liao R, Duan L, Lei C, Pan H, Ding Y, Zhang Q, et al. Thiopeptide biosynthesis featuring ribosomally synthesized precursor peptides and conserved posttranslational modifications. Chem Biol. 2009;16(2):141–7. Available from: http://www.ncbi.nlm.nih.gov/pubmed/19246004. doi:10.1016/j.chembiol.2009.01.007.

170 Kamigiri K, Hidaka T, Imai S, Murakami T, Seto H. Studies on the biosynthesis of bialaphos (SF-1293) 12. C-P bond formation mechanism of bialaphos: discovery of a P-methylation enzyme. J Antibiot (Tokyo). 1992;45(5):781–7.

171 Morris RP, Leeds JA, Naegeli HU, Oberer L, Memmert K, Weber E, et al. Ribosomally synthesized thiopeptide antibiotics targeting elongation factor Tu. J Am Chem Soc. 2009;131(16):5946–55. doi:10.1021/ja900488a.

172 Du L, Sanchez C, Chen M, Edwards DJ, Shen B. The biosynthetic gene cluster for the antitumor drug bleomycin from Streptomyces verticillus ATCC15003 supporting functional interactions between nonribosomal peptide synthetases and a polyketide synthase. Chem Biol. 2000;7(8):623–42. doi:S1074-5521(00)00011-9.

173 Tao M, Wang L Fau Wendt-Pienkowski E, Wendt-Pienkowski E Fau George NP, George Np Fau Galm U, Galm U Fau Zhang G, Zhang G Fau Coughlin JM, et al. The tallysomycin biosynthetic gene cluster from Streptoalloteichus hindustanus E465-94 ATCC 31158 unveiling new insights into the biosynthesis of the bleomycin family of antitumor antibiotics. Mol Biosys. 2007;3(1):60–74.

174 Galm U, Wendt-Pienkowski E Fau Wang L, Wang L Fau George NP, George Np Fau Oh TJ, Oh Tj Fau Yi F, Yi F Fau Tao M, et al. The biosynthetic gene cluster of zorbamycin, a member of the bleomycin family of antitumor antibiotics, from Streptomyces flavoviridis ATCC 21892. Mol Biosyst. 2009;(1742-2051). doi:10.1039/b814075h.

175 Huang W, Xu H, Li Y, Zhang F, Chen XY, He QL, et al. Characterization of yatakemycin gene cluster revealing a radical S-adenosylmethionine dependent methyltransferase and highlighting spirocyclopropane biosynthesis. J Am Chem Soc. 2012;134(21):8831–40. Available from: http://www.ncbi.nlm.nih.gov/pubmed/22612591. doi:10.1021/ja211098r.

176 Henderson DP, Wyckoff EE, Rashidi CE, Verlei H, Oldham AL. Characterization of the Plesiomonas shigelloides genes encoding the heme iron utilization system. J Bacteriol. 2001;183(9):2715–23. Available from: http://www.ncbi.nlm.nih.gov/pubmed/11292789. doi:10.1128/JB.183.9.2715-2723.2001.

177 Suits MD, Lang J, Pal GP, Couture M, Jia Z. Structure and heme binding properties of Escherichia coli O157:H7 ChuX. Protein Sci. 2009;18(4):825–38. doi:10.1002/pro.84.

178 Sekine Y, Tanzawa T, Tanaka Y, Ishimori K, Uchida T. Cytoplasmic Heme-Binding Protein (HutX) from Vibrio cholerae Is an Intracellular Heme Transport Protein for the Heme-Degrading Enzyme, HutZ. Biochemistry. 2015;55(6):2291–98. doi:10.1021/ar5000028n.

179 Buysschaert G, Verstraete K, Savvides SN, Vergauwen B. Structural and biochemical characterization of an atypical short-chain dehydrogenase/reductase reveals an unusual cofactor preference. FEBS J. 2013;280(5):1358–70. Available from: http://www.ncbi.nlm.nih.gov/pubmed/23311896. doi:10.1111/febs.12128.

180 Oldham AL, Wood TA, Henderson DP. Plesiomonas shigelloides hugZ encodes an iron-regulated heme binding protein required for heme iron utilization. Can J Microbiol. 2008;54(2):97–102. doi:10.1139/w07-122.

181 Zhang R, Zhang J, Guo G, Mao X, Tong W, Zhang Y, et al. Crystal structure of Campylobacter jejuni ChuZ: a split-barrel family heme oxygenase with a novel heme-binding mode. Biochem Biophys Res Commun. 2011;415(1):82–7. Available from: http://www.ncbi.nlm.nih.gov/pubmed/22020097. doi:10.1016/j.bbrc.2011.10.016.

182 Guo Y, Guo G, Mao X, Zhang W, Xiao J, Tong W, et al. Functional identification of HugZ, a heme oxygenase from Helicobacter pylori. BMC Microbiol. 2008;8:226. doi:10.1186/1471-2180-8-226.

183 Hu Y, Jiang F, Guo Y, Shen X, Zhang Y, Zhang R, et al. Crystal structure of HugZ, a novel heme oxygenase from Helicobacter pylori. J Biol Chem. 2011;286(2):1537–44. doi:10.1074/jbc.M110.172007.

184 Liu X, Gong J, Wei T, Wang Z, Du Q, Zhu D, et al. Crystal structure of HutZ, a heme storage protein from Vibrio cholerae: A structural mismatch observed in the region of high sequence conservation. BMC Struct Biol. 2012;12:23. Available from: http://www.ncbi.nlm.nih.gov/pubmed/23013214. doi:10.1186/1472-6807-12-23.

185 Wilks A. The ShuS protein of Shigella dysenteriae is a heme-sequestering protein that also binds DNA. Arch Biochem Biophys. 2001;387(1):137–42. doi:10.1006/abbi.2000.2250.

186 Wilks A, Burkhard KA. Heme and virulence: how bacterial pathogens regulate, transport and utilize heme. Nat Prod Rep. 2007;24(3):511–22. doi:10.1039/b604193k.

187 Carpenter CE, Mahoney AW. Contributions of heme and nonheme iron to human nutrition. Crit Rev Food Sci Nutr. 1992;31(4):333–67. Available from: http://www.ncbi.nlm.nih.gov/pubmed/1581009. doi:10.1080/10408399209527576.

188 Hooda J, Shah A, Zhang L. Heme, an essential nutrient from dietary proteins, critically impacts diverse physiological and pathological processes. Nutrients. 2014;6(3):1080–102. Available from: http://www.ncbi.nlm.nih.gov/pubmed/24633395. doi:10.3390/nu6031080.

189 Frankenberg-Dinkel N. Bacterial heme oxygenases. Antioxid Redox Signal. 2004;6(5):825–34. Available from: http://www.ncbi.nlm.nih.gov/pubmed/15345142. doi:10.1089/ars.2004.6.825.

190 Wandersman C, Delepelaire P. Bacterial iron sources: from siderophores to hemophores. Annu Rev Microbiol. 2004;58:611–47. doi:10.1146/annurev.micro.58.030603.123811.

191 Wilks A. Heme oxygenase: evolution, structure, and mechanism. Antioxid Redox Signal. 2002;4(4):603–14. Available from: http://www.ncbi.nlm.nih.gov/pubmed/12230872. doi:10.1089/15230860260220102.

192 Wilks A, Schmitt MP. Expression and characterization of a heme oxygenase (Hmu O) from Corynebacterium diphtheriae. Iron acquisition requires oxidative cleavage of the heme macrocycle. J Biol Chem. 1998;273(2):837–41.

193 Zhu W, Wilks A, Stojiljkovic I. Degradation of heme in gram-negative bacteria: the product of the hemO gene of Neisseriae is a heme oxygenase. J Bacteriol. 2000;182(23):6783–90.

194 Septer AN, Wang Y, Ruby EG, Stabb EV, Dunn AK. The haem-uptake gene cluster in Vibrio fischeri is regulated by Fur and contributes to symbiotic colonization. Environ Microbiol. 2011;13(11):2855–64. doi:10.1111/j.1462-2920.2011.02558.x.

195 Lobo SA, Lawrence AD, Romao CV, Warren MJ, Teixeira M, Saraiva LM. Characterisation of Desulfovibrio vulgaris haem b synthase, a radical SAM family member. Biochim Biophys Acta. 2014;1844(7):1238–47. Available from: http://www.ncbi.nlm.nih.gov/pubmed/24713144. doi:10.1016/j.bbapap.2014.03.016.

196 Grove TL, Lee KH, St Clair J, Krebs C, Booker SJ. In vitro characterization of AtsB, a radical SAM formylglycine-generating enzyme that contains three [4Fe-4S] clusters. Biochemistry. 2008;47(28):7523–38. doi:10.1021/bi8004297.

197 Wilks A. Purification and characterization of heme oxygenase. Curr Protoc Toxicol. 2003;Chapter 9:Unit9 9. Available from: http://www.ncbi.nlm.nih.gov/pubmed/23045096. doi:10.1002/0471140856.tx0909s15.

198 Hiratsuka T, Suzuki H, Kariya R, Seo T, Minami A, Oikawa H. Biosynthesis of the structurally unique polycyclopropanated polyketide-nucleoside hybrid jawsamycin (FR-900848). Angew Chem Int Ed Engl. 2014;53(21):5423–6. Available from: http://www.ncbi.nlm.nih.gov/pubmed/24756819. doi:10.1002/anie.201402623.

199 Gorchein A, Lim CK, Cassey P. Extraction and analysis of colourful eggshell pigments using HPLC and HPLC/electrospray ionization tandem mass spectrometry. Biomed Chromatogr. 2009;23(6):602–6. Available from: http://www.ncbi.nlm.nih.gov/pubmed/19277957. doi:10.1002/bmc.1158.

200 Uchida T, Sekine Y, Matsui T, Ikeda-Saito M, Ishimori K. A heme degradation enzyme, HutZ, from Vibrio cholerae. Chem Commun (Camb). 2012;48(53):6741–3. doi:10.1039/c2cc31147j.

201 Dailey HA, Gerdes S. HemQ: An iron-coproporphyrin oxidative decarboxylase for protoheme synthesis in Firmicutes and Actinobacteria. Arch Biochem Biophys. 2015;574:27–35. Available from: http://www.ncbi.nlm.nih.gov/pubmed/25711532. doi:10.1016/j.abb.2015.02.017.

202 Chase J T, Rabinowitz JC. Role of pyruvate and S-adenosylmethioine in activating the pyruvate formate-lyase of Escherichia coli. J Bacteriol. 1968;96(4):1065–78. Available from: http://www.ncbi.nlm.nih.gov/pubmed/4879554.

203 Sawers G, Bock A. Anaerobic regulation of pyruvate formate-lyase from Escherichia coli K-12. J Bacteriol. 1988;170(11):5330–6. Available from: http://www.ncbi.nlm.nih.gov/pubmed/3053657.

204 Lovenberg W, Buchanan BB, Rabinowitz JC. STUDIES ON THE CHEMICAL NATURE OF CLOSTRIDIAL FERREDOXIN. J Biol Chem. 1963;238:3899–913.

205 Waterhouse AM, Procter JB, Martin DM, Clamp M, Barton GJ. Jalview Version 2–a multiple sequence alignment editor and analysis workbench. Bioinformatics. 2009;25(9):1189–91. Available from: http://www.ncbi.nlm.nih.gov/pubmed/19151095. doi:10.1093/bioinformatics/btp033.

206 Wegele R, Tasler R, Zeng Y, Rivera M, Frankenberg-Dinkel N. The heme oxygenase(s)-phytochrome system of Pseudomonas aeruginosa. J Biol Chem. 2004;279(44):45791–802. Available from: http://www.ncbi.nlm.nih.gov/pubmed/15310749. doi:10.1074/jbc.M408303200.

207 Davis SJ, Vener AV, Vierstra RD. Bacteriophytochromes: phytochrome-like photoreceptors from nonphotosynthetic eubacteria. Science. 1999;286(5449):2517–20. Available from: http://www.ncbi.nlm.nih.gov/pubmed/10617469.

208 Bhoo SH, Davis SJ, Walker J, Karniol B, Vierstra RD. Bacteriophytochromes are photochromic histidine kinases using a biliverdin chromophore. Nature. 2001;414(6865):776–9. Available from: http://www.ncbi.nlm.nih.gov/pubmed/11742406. doi:10.1038/414776a.

209 LaMattina JL, Nix DB, Lanzilotta WN. A radical paradigm for heme degradation: ChuW from E. coli O157:H7 is a heme decyclase. Proc Natl Acad Sci U S A. 2016;To be published.

210 Krissinel E, Henrick K. Inference of macromolecular assemblies from crystalline state. J Mol Biol. 2007;372(3):774–97. Available from: http://www.ncbi.nlm.nih.gov/pubmed/17681537. doi:10.1016/j.jmb.2007.05.022.

211 Ortega A, Amoros D, Garcia de la Torre J. Prediction of hydrodynamic and other solution properties of rigid proteins from atomic- and residue-level models. Biophys J. 2011;101(4):892–8. Available from: http://www.ncbi.nlm.nih.gov/pubmed/21843480. doi:10.1016/j.bpj.2011.06.046.

212 Selwyn MJ. A simple test for inactivation of an enzyme during assay. Biochim Biophys Acta. 1965;105(1):193–5. Available from: http://www.ncbi.nlm.nih.gov/pubmed/4221326.

213 Hammes GG, Wu CW. Kinetics of allosteric enzymes. Annu Rev Biophys Bioeng. 1974;3(0):1–33. Available from: http://www.ncbi.nlm.nih.gov/pubmed/4371650. doi:10.1146/annurev.bb.03.060174.000245.

214 Ricard J, Cornish-Bowden A. Co-operative and allosteric enzymes: 20 years on. Eur J Biochem. 1987;166(2):255–72. Available from: http://www.ncbi.nlm.nih.gov/pubmed/3301336.

215 Neet KE. Cooperativity in enzyme function: equilibrium and kinetic aspects. Methods Enzymol. 1995;249:519–67. Available from: http://www.ncbi.nlm.nih.gov/pubmed/7791626.

216 Jansen T, Daiber A. Direct Antioxidant Properties of Bilirubin and Biliverdin. Is there a Role for Biliverdin Reductase? Front Pharmacol. 2012;3:30. Available from: http://www.ncbi.nlm.nih.gov/pubmed/22438843. doi:10.3389/fphar.2012.00030.

217 Greenberg DA. The jaundice of the cell. Proc Natl Acad Sci U S A. 2002;99(25):15837–9. Available from: http://www.ncbi.nlm.nih.gov/pubmed/12461187. doi:10.1073/pnas.012685199.

218 Kadirvelraj R, Sennett NC, Custer GS, Phillips RS, Wood ZA. Hysteresis and negative cooperativity in human UDP-glucose dehydrogenase. Biochemistry. 2013;52(8):1456–65. Available from: http://www.ncbi.nlm.nih.gov/pubmed/23363239. doi:10.1021/bi301593c.

219 Sanchez JE, Gross PG, Goetze RW, Walsh J R M, Peeples WB, Wood ZA. Evidence of Kinetic Cooperativity in Dimeric Ketopantoate Reductase from Staphylococcus aureus. Biochemistry. 2015;54(21):3360–9. Available from: http://www.ncbi.nlm.nih.gov/pubmed/25946571. doi:10.1021/acs.biochem.5b00174.

220 Fu ZQ, Rose J, Wang BC. SGXPro: a parallel workflow engine enabling optimization of program performance and automation of structure determination. Acta Crystallogr D Biol Crystallogr. 2005;61(Pt 7):951–9. Available from: http://www.ncbi.nlm.nih.gov/pubmed/15983418. doi:10.1107/S0907444905010541.

221 Adams PD, Afonine PV, Bunkoczi G, Chen VB, Davis IW, Echols N, et al. PHENIX: a comprehensive Python-based system for macromolecular structure solution. Acta Crystallogr D Biol Crystallogr. 2010;66(Pt 2):213–21. Available from: http://www.ncbi.nlm.nih.gov/pubmed/20124702. doi:10.1107/S0907444909052925.

222 Emsley P, Cowtan K. Coot: model-building tools for molecular graphics. Acta Crystallogr D Biol Crystallogr. 2004;60(Pt 12 Pt 1):2126–32. Available from: http://www.ncbi.nlm.nih.gov/pubmed/15572765. doi:10.1107/S0907444904019158.

223 Laue TM, Shah BD, Ridgeway TM, Pelletier SL. Analytical ultracentrifugation in biochemistry and polymer science. Computer-aided interpretation of analytical sedimentation data for proteins.. Cambridge, U.K.: The Royal Society of Chemistry; 1992.

224 Brown PH, Schuck P. Macromolecular size-and-shape distributions by sedimentation velocity analytical ultracentrifugation. Biophys J. 2006;90(12):4651–61. Available from: http://www.ncbi.nlm.nih.gov/pubmed/16565040. doi:10.1529/biophysj.106.081372.

225 Palmier MO, Van Doren SR. Rapid determination of enzyme kinetics from fluorescence: overcoming the inner filter effect. Anal Biochem. 2007;371(1):43–51. Available from: http://www.ncbi.nlm.nih.gov/pubmed/17706587. doi:10.1016/j.ab.2007.07.008.

226 Broderick JB, Duffus BR, Duschene KS, Shepard EM. Radical S-adenosylmethionine enzymes. Chem Rev. 2014;114(8):4229–317. Available from: http://www.ncbi.nlm.nih.gov/pubmed/24476342. doi:10.1021/cr4004709.

227 Patterson WR, Poulos TL, Goodin DB. Identification of a porphyrin pi cation radical in ascorbate peroxidase compound I. Biochemistry. 1995;34(13):4342–5. Available from: http://www.ncbi.nlm.nih.gov/pubmed/7703248.

228 Toraya T. Enzymatic radical catalysis: coenzyme B12-dependent diol dehydratase. Chem Rec. 2002;2(5):352–66. Available from: http://www.ncbi.nlm.nih.gov/pubmed/12369058. doi:10.1002/tcr.10035.

229 Toraya T. [Radical-catalyzed enzymatic reactions: structure and mechanism of B12 enzymes]. Seikagaku. 2002;74(2):87–102. Available from: http://www.ncbi.nlm.nih.gov/pubmed/11925942.

230 O'Brien JR, Raynaud C, Croux C, Girbal L, Soucaille P, Lanzilotta WN. Insight into the mechanism of the B12-independent glycerol dehydratase from Clostridium butyricum: preliminary biochemical and structural characterization. Biochemistry. 2004;43(16):4635–45. Available from: http://www.ncbi.nlm.nih.gov/pubmed/15096031. doi:10.1021/bi035930k.

231 Knappe J, Wagner AF. Glycyl free radical in pyruvate formate-lyase: synthesis, structure characteristics, and involvement in catalysis. Methods Enzymol. 1995;258:343–62. Available from: http://www.ncbi.nlm.nih.gov/pubmed/8524160.

232 Knappe J, Elbert S, Frey M, Wagner AF. Pyruvate formate-lyase mechanism involving the protein-based glycyl radical. Biochem Soc Trans. 1993;21 (Pt 3)(3):731–4. Available from: http://www.ncbi.nlm.nih.gov/pubmed/8135930.

233 Frey M, Rothe M, Wagner AF, Knappe J. Adenosylmethionine-dependent synthesis of the glycyl radical in pyruvate formate-lyase by abstraction of the glycine C-2 pro-S hydrogen atom. Studies of [2H]glycine-substituted enzyme and peptides homologous to the glycine 734 site. J Biol Chem. 1994;269(17):12432–7. Available from: http://www.ncbi.nlm.nih.gov/pubmed/8175649.

234 Sun X, Eliasson R, Pontis E, Andersson J, Buist G, Sjoberg BM, et al. Generation of the glycyl radical of the anaerobic Escherichia coli ribonucleotide reductase requires a specific activating enzyme. J Biol Chem. 1995;270(6):2443–6. Available from: http://www.ncbi.nlm.nih.gov/pubmed/7852304.

235 Sun X, Ollagnier S, Schmidt PP, Atta M, Mulliez E, Lepape L, et al. The free radical of the anaerobic ribonucleotide reductase from Escherichia coli is at glycine 681. J Biol Chem. 1996;271(12):6827–31. Available from: http://www.ncbi.nlm.nih.gov/pubmed/8636106.

236 Selmer T, Pierik AJ, Heider J. New glycyl radical enzymes catalysing key metabolic steps in anaerobic bacteria. Biol Chem. 2005;386(10):981–8. Available from: http://www.ncbi.nlm.nih.gov/pubmed/16218870. doi:10.1515/BC.2005.114.

237 Shisler KA, Broderick JB. Glycyl radical activating enzymes: structure, mechanism, and substrate interactions. Arch Biochem Biophys. 2014;546:64–71. Available from: http://www.ncbi.nlm.nih.gov/pubmed/24486374. doi:10.1016/j.abb.2014.01.020.

238 Krieger CJ, Roseboom W, Albracht SP, Spormann AM. A stable organic free radical in anaerobic benzylsuccinate synthase of Azoarcus sp. strain T. J Biol Chem. 2001;276(16):12924–7. Available from: http://www.ncbi.nlm.nih.gov/pubmed/11278506. doi:10.1074/jbc.M009453200.

239 Selmer T, Andrei PI. p-Hydroxyphenylacetate decarboxylase from Clostridium difficile. A novel glycyl radical enzyme catalysing the formation of p-cresol. Eur J Biochem. 2001;268(5):1363–72. Available from: http://www.ncbi.nlm.nih.gov/pubmed/11231288.

240 Craciun S, Balskus EP. Microbial conversion of choline to trimethylamine requires a glycyl radical enzyme. Proc Natl Acad Sci U S A. 2012;109(52):21307–12. Available from: http://www.ncbi.nlm.nih.gov/pubmed/23151509. doi:10.1073/pnas.1215689109.

241 Craciun S, Marks JA, Balskus EP. Characterization of choline trimethylamine-lyase expands the chemistry of glycyl radical enzymes. ACS Chem Biol. 2014;9(7):1408–13. Available from: http://www.ncbi.nlm.nih.gov/pubmed/24854437. doi:10.1021/cb500113p.

242 Kalnins G, Kuka J, Grinberga S, Makrecka-Kuka M, Liepinsh E, Dambrova M, et al. Structure and Function of CutC Choline Lyase from Human Microbiota Bacterium Klebsiella pneumoniae. J Biol Chem. 2015;290(35):21732–40. Available from: http://www.ncbi.nlm.nih.gov/pubmed/26187464. doi:10.1074/jbc.M115.670471.

243 Scott KP, Martin JC, Campbell G, Mayer CD, Flint HJ. Whole-genome transcription profiling reveals genes up-regulated by growth on fucose in the human gut bacterium "Roseburia inulinivorans". J Bacteriol. 2006;188(12):4340–9. Available from: http://www.ncbi.nlm.nih.gov/pubmed/16740940. doi:10.1128/JB.00137-06.

244 Peng Y, Veneziano SE, Gillispie GD, Broderick JB. Pyruvate formate-lyase, evidence for an open conformation favored in the presence of its activating enzyme. J Biol Chem. 2010;285(35):27224–31. Available from: http://www.ncbi.nlm.nih.gov/pubmed/20571026. doi:10.1074/jbc.M109.096875.

245 Henshaw TF, Cheek J, Broderick JB. The [4Fe-4S]1+ Cluster of Pyruvate Formate-Lyase Activating Enzyme Generates the Glycyl Radical on Pyruvate Formate-Lyase: EPR-Detected Single Turnover. J Am Chem Soc. 2000;(122):8331–8332. doi:10.1021/ja002012q.

246 Crain AV, Broderick JB. Pyruvate formate-lyase and its activation by pyruvate formate-lyase activating enzyme. J Biol Chem. 2014;289(9):5723–9. Available from: http://www.ncbi.nlm.nih.gov/pubmed/24338017. doi:10.1074/jbc.M113.496877.

247 Funk MA, Judd ET, Marsh EN, Elliott SJ, Drennan CL. Structures of benzylsuccinate synthase elucidate roles of accessory subunits in glycyl radical enzyme activation and activity. Proc Natl Acad Sci U S A. 2014;111(28):10161–6. Available from: http://www.ncbi.nlm.nih.gov/pubmed/24982148. doi:10.1073/pnas.1405983111.

248 Logan DT, Andersson J, Sjoberg BM, Nordlund P. A glycyl radical site in the crystal structure of a class III ribonucleotide reductase. Science. 1999;283(5407):1499–504. Available from: http://www.ncbi.nlm.nih.gov/pubmed/10066165.

249 Martins BM, Blaser M, Feliks M, Ullmann GM, Buckel W, Selmer T. Structural basis for a Kolbe-type decarboxylation catalyzed by a glycyl radical enzyme. J Am Chem Soc. 2011;133(37):14666–74. Available from: http://www.ncbi.nlm.nih.gov/pubmed/21823587. doi:10.1021/ja203344x.

250 Becker A, Fritz-Wolf K, Kabsch W, Knappe J, Schultz S, Volker Wagner AF. Structure and mechanism of the glycyl radical enzyme pyruvate formate-lyase. Nat Struct Biol. 1999;6(10):969–75. doi:10.1038/13341.

251 Lehtio L, Leppanen VM, Kozarich JW, Goldman A. Structure of Escherichia coli pyruvate formate-lyase with pyruvate. Acta Crystallogr D Biol Crystallogr. 2002;58(Pt 12):2209–12. Available from: http://www.ncbi.nlm.nih.gov/pubmed/12454503.

252 Leppanen VM, Merckel MC, Ollis DL, Wong KK, Kozarich JW, Goldman A. Pyruvate formate lyase is structurally homologous to type I ribonucleotide reductase. Structure. 1999;7(7):733–44. Available from: http://www.ncbi.nlm.nih.gov/pubmed/10425676. doi:10.1016/S0969-2126(99)80098-7.

253 Leppanen VM, Parast CV, Wong KK, Kozarich JW, Goldman A. Purification and crystallization of a proteolytic fragment of Escherichia coli pyruvate formate-lyase. Acta Crystallogr D Biol Crystallogr. 1999;55(Pt 2):531–3. Available from: http://www.ncbi.nlm.nih.gov/pubmed/10089368.

254 Bharadwaj VS, Dean AM, Maupin CM. Insights into the glycyl radical enzyme active site of benzylsuccinate synthase: a computational study. J Am Chem Soc. 2013;135(33):12279–88. Available from: http://www.ncbi.nlm.nih.gov/pubmed/23865732. doi:10.1021/ja404842r.

255 Feliks M, Martins BM, Ullmann GM. Catalytic mechanism of the glycyl radical enzyme 4-hydroxyphenylacetate decarboxylase from continuum electrostatic and QC/MM calculations. J Am Chem Soc. 2013;135(39):14574–85. Available from: http://www.ncbi.nlm.nih.gov/pubmed/24028464. doi:10.1021/ja402379q.

256 Feliks M, Ullmann GM. Glycerol dehydratation by the B12-independent enzyme may not involve the migration of a hydroxyl group: a computational study. J Phys Chem B. 2012;116(24):7076–87. Available from: http://www.ncbi.nlm.nih.gov/pubmed/22626266. doi:10.1021/jp301165b.

257 Demick JM, Lanzilotta WN. Radical SAM activation of the B12-independent glycerol dehydratase results in formation of 5'-deoxy-5'-(methylthio)adenosine and not 5'-deoxyadenosine. Biochemistry. 2011;50(4):440–2. doi:10.1021/bi101255e.

258 Pontes H, Guedes de Pinho P, Casal S, Carmo H, Santos A, Magalhaes T, et al. GC determination of acetone, acetaldehyde, ethanol, and methanol in biological matrices and cell culture. J Chromatogr Sci. 2009;47(4):272–8. Available from: http://www.ncbi.nlm.nih.gov/pubmed/19406012.

259 Hioe J, Savasci G, Brand H, Zipse H. The stability of Calpha peptide radicals: why glycyl radical enzymes? Chemistry. 2011;17(13):3781–9. Available from: http://www.ncbi.nlm.nih.gov/pubmed/21341321. doi:10.1002/chem.201002620.

260 Frey PA. Radical mechanisms of enzymatic catalysis. Annu Rev Biochem. 2001;70:121–48. Available from: http://www.ncbi.nlm.nih.gov/pubmed/11395404. doi:10.1146/annurev.biochem.70.1.121.

261 Ofer A, Kreft J, Logan DT, Cohen G, Borovok I, Aharonowitz Y. Implications of the inability of Listeria monocytogenes EGD-e to grow anaerobically due to a deletion in the class III NrdD ribonucleotide reductase for its use as a model laboratory strain. J Bacteriol. 2011;193(12):2931–40. Available from: http://www.ncbi.nlm.nih.gov/pubmed/21478338. doi:10.1128/JB.01405-10.

262 Li L, Patterson DP, Fox CC, Lin B, Coschigano PW, Marsh EN. Subunit structure of benzylsuccinate synthase. Biochemistry. 2009;48(6):1284–92. Available from: http://www.ncbi.nlm.nih.gov/pubmed/19159265. doi:10.1021/bi801766g.

263 Knappe J, Sawers G. A radical-chemical route to acetyl-CoA: the anaerobically induced pyruvate formate-lyase system of Escherichia coli. FEMS Microbiol Rev. 1990;6(4):383–98. Available from: http://www.ncbi.nlm.nih.gov/pubmed/2248795.

264 Nnyepi MR, Peng Y, Broderick JB. Inactivation of E. coli pyruvate formate-lyase: role of AdhE and small molecules. Arch Biochem Biophys. 2007;459(1):1–9. Available from: http://www.ncbi.nlm.nih.gov/pubmed/17280641. doi:10.1016/j.abb.2006.12.024.

265 Yamanishi M, Kinoshita K, Fukuoka M, Saito T, Tanokuchi A, Ikeda Y, et al. Redesign of coenzyme B(12) dependent diol dehydratase to be resistant to the mechanism-based inactivation by glycerol and act on longer chain 1,2-diols. FEBS J. 2012;279(5):793–804. Available from: http://www.ncbi.nlm.nih.gov/pubmed/22221669. doi:10.1111/j.1742-4658.2012.08470.x.

266 Shibata N, Nakanishi Y, Fukuoka M, Yamanishi M, Yasuoka N, Toraya T. Structural rationalization for the lack of stereospecificity in coenzyme B12-dependent diol dehydratase. J Biol Chem. 2003;278(25):22717–25. Available from: http://www.ncbi.nlm.nih.gov/pubmed/12684496. doi:10.1074/jbc.M301513200.

267 Kulzer R, Pils T, Kappl R, Huttermann J, Knappe J. Reconstitution and characterization of the polynuclear iron-sulfur cluster in pyruvate formate-lyase-activating enzyme. Molecular properties of the holoenzyme form. J Biol Chem. 1998;273(9):4897–903. Available from: http://www.ncbi.nlm.nih.gov/pubmed/9478932.

268 Chromy V, Fischer J, Kulhanek V. Re-evaluation of EDTA-chelated biuret reagent. Clin Chem. 1974;20(10):1362–3. Available from: http://www.ncbi.nlm.nih.gov/pubmed/4213350.

269 Sottocasa GL, Stagni N, De Bernard B. A spectrophotometric method for the direct recording of dioldehydrase activity. Experientia. 1971;27(10):1247–8. Available from: http://www.ncbi.nlm.nih.gov/pubmed/4399616.

270 Brunger AT. Free R value: a novel statistical quantity for assessing the accuracy of crystal structures. Nature. 1992;355(6359):472–5. Available from: http://www.ncbi.nlm.nih.gov/pubmed/18481394.

271 Schuck P. Size-distribution analysis of macromolecules by sedimentation velocity ultracentrifugation and lamm equation modeling. Biophys J. 2000;78(3):1606–19. Available from: http://www.ncbi.nlm.nih.gov/pubmed/10692345. doi:10.1016/S0006-3495(00)76713-0.

Appendix

Appendix A

1,2-PROPANEDIOL DEHYDRATION IN *ROSEBURIA INULINIVORANS*; STRUCTURAL BASIS FOR SUBSTRATE AND ENANTIOMER SELECTIVITY[1]

[1] **Joseph W. LaMattina**, Nicholas D. Keul, Pierre Reitzer, Suraj Kapoor, Felipe Galzerani, Daniel J. Koch, Iuri E. Gouvea, and William N. Lanzilotta. 2016. *Journal of Biological Chemistry*. Ahead of Print. Reprinted here with permission of the publisher.

Abstract

Glycyl radical enzymes (GREs) represent a diverse superfamily of enzymes that utilize a radical mechanism to catalyze difficult, but often essential, chemical reactions. In this work, we present the first biochemical and structural data for a GRE-type diol dehydratase from the organism *Roseburia inulinivorans* (RiDD). Despite high sequence (48% identity) and structural similarity to the GRE-type glycerol dehydratase from *Clostridium butyricum* (CbGD), we demonstrate that the RiDD is in fact a diol dehydratase. In addition, the RiDD will utilize both (S)-1,2-propanediol and (R)-1,2-propanediol as a substrate, with an observed preference for the (S) enantiomer. Based on the new structural information we develop and successfully test a hypothesis that explains the functional differences we observe.

Introduction

In contrast to the well-characterized B_{12}-dependent dehydratases[228,229], only one glycyl radical enzyme (GRE) or GRE-type dehydratase has been characterized to date[230]. While pyruvate formate lyase (PFL) and anaerobic ribonucleotide reductase (ARNR) are among the most comprehensively studied GREs[231–236], recent work provides evidence that the catalytic diversity of GREs is considerably greater than originally anticipated[237]. It is now recognized that GREs can catalyze the formation of C-C bonds (benzyl succinate synthase)[238], C-C bond cleavage (PFL and 4-hydroxyphenylacetate decarboxylase - a.k.a. 4-HPAD)[232,239], ribonucleotide reduction (aRNR)[234], dehydration reactions (glycerol dehydratase)[230], and C-N bond cleavage (choline TMA-lyase)[240–242]. Taken together, these observations underscore a superfamily of enzymes that utilize a conserved structural core to perform vastly different radical-catalyzed reactions. Many of these reactions are important to human health or represent difficult chemical conversions that may be significant to

the development of future biocatalysts.

At the present time, the only structural information available for any GRE-type dehydratase is that of the glycerol dehydratase from *Clostridium butyricum* (CbGD)[104,230]. The presence of a homologous 1,2-propandiol dehydratase in *Roseburia inulinivorans* was proposed based on genomic and metabolic analyses of the organism[243]. However, the enzyme was never isolated, and only propanol production was observed when *R. inulinivorans* was cultured under anaerobic conditions[243]. In addition to the presence of the proposed GRE-type dehydratase gene, the operon containing the diol dehydratase (WP_007885173) also contained another gene that was consistent with that of an "activating enzyme" (ABC25540). These observations are significant because all of the GREs that have been investigated to date are expressed in an inactive form that is post-translationally activated by an "activating enzyme" (AE). The generally accepted mechanism for the activation of all GREs involves a radical SAM enzyme that is specific to the GRE partnering enzyme[237]. The activation process that is catalyzed by the AE involves a uniquely coordinated [4Fe-4S] cluster and S-adenosylmethionine (SAM) as a co-substrate. The [4Fe-4S] cluster (formerly in the 1+ oxidation state) catalyzes the reductive cleavage of SAM to generate a highly reactive 5'-deoxyadenosyl-5'-radical (5'-dA•) that is positioned to facilitate the abstraction of a hydrogen atom from a conserved glycine residue on the GRE[237]. The activation reaction, and subsequent dehydration investigated herein, are highly sensitive to molecular oxygen and must be performed under strictly anaerobic conditions. *In vitro*, the catalytic [4Fe-4S] can be reduced from the 2+ to the 1+ oxidation state using a biological reducing system, such as a NADPH flavodoxin/oxidoreductase and flavodoxin system[196]. In addition, chemical reductants such as sodium dithionite or a light-driven reducing system are also effective electron donors[244,245]. The activation process, or generation of the catalytic glycyl radical, is further complicated by recent observations that demonstrate the substrate for the GRE accelerates the activation rate[246]. Regardless

of the electron source, once the glycyl radical is generated, all GREs will catalyze their primary metabolic reaction, regenerating the radical with each turnover. Precisely how or when GREs are inactivated *in vivo* remains an outstanding question in the field.

In this work, we have expressed and purified the predicted diol dehydratase from *R. inulinivorans* (RiDD) as well as the RiDD activating enzyme (RiDD-AE) (homologously expressed in *E. coli*). In addition to assay data, we have determined the crystal structures for the ethanediol- and propanediol-bound RiDD. Structural alignment of the crystallographic models with our previously published models for the glycerol dehydratase from *C. butyricum* (CbGD) reveals a similar overall fold and a highly conserved active site structure. However, subtle variations in critical active site amino acid residues provide a viable explanation for the observed functional differences. This hypothesis is tested through site directed mutagenesis herein.

Results

Overall structure of the RiDD. All of the glycyl radical enzyme (GRE) structures published to date represent a model of the inactive enzyme. This is not surprising considering that maintaining the glycyl radical during crystal growth is simply not feasible. Despite this technical detail, the crystal structures for GREs have provided significant insight into enzyme mechanism[230,247–253]. Numerous computational predictions have also been made based on this structural information[254–256]. In this work we were able to crystallize and model the RiDD with ethanediol or 1,2-propanediol bound in the active site (Table A.1).

The overall fold of the RiDD is most similar to the CbGD. Figure A.1 (Panel A) shows an overlay comparing the model of the RiDD, reported herein, aligned with the structure previously reported for the GRE-type glycerol dehydratase from Clostridum butyricum (CbGD)[230]. Figure A.1 (Panel B) also highlights the location of the conserved glycine residues in both enzymes and the high degree of structural homology found in the C-

terminal domain. With a small exception, discussed below, we do not observe any significant changes in the overall position of the backbone atoms when the ethanediol- and propanediol-bound models are compared with each other or the CbGD structures. However, there is a 48-amino acid insert that is present in the RiDD (Figure A.1, Panel A). Specifically, when compared to the CbGD, the RiDD contains a 48 amino acid insert (residues 592-640 of the RiDD). Excluding this insertion and the first twenty N-terminal amino acids of the RiDD, the structural alignment of monomer A from the CbGD model (PDB ID 1R9D) with the A monomer of the RiDD model results in a root mean square deviation (RMSD) of 0.6 Å for the backbone alpha carbon atoms. The additional 48 amino acid insert that is found in the RiDD extends an existing helix and forms an additional helix, loop, and helix motif. This region of the RiDD structure is highlighted in dark blue in Figure A.1, Panel A, and forms an important crystallographic contact by interacting with the identical domain in a symmetry-related molecule (not shown). Interestingly, three hydrophobic amino acids (I623, I627, and L631) form a largely hydrophobic interface between the helical domains of this insert with a buried surface area of approximately 470 $Å^2$. The precise function of the additional domain is not clear, however, much of this region could not be modeled for the (S)-1,2-propanediol-bound model due to a lack of electron density. This observation is consistent with the change we observe in the space group for the propanediol-treated crystals (Table 1) suggesting that substrate binding may be communicated to this region of the enzyme. A recent report on the GRE choline lyase (CutC) also demonstrated that substrate binding can influence the overall structure of the enzyme[242].

The RiDD forms a dimer in solution. Sedimentation velocity analysis of the RiDD in solution, without substrate shows a c(s) distribution dominated by a 9.2 S species (70.5%), which is close to the predicted values of 8.8 S and 8.7 S for the dimers produced by non-crystallographic and crystallographic symmetry operations, respectively (Figure

2 Panel A). The dimer with the largest surface area is shown in Figure A.2, Panel B. The difference in the observed and expected S values suggests that the substrate-free dimer may adopt a slightly more compact conformation than that observed in the crystal lattice of substrate bound RiDD. We also observe a 5.6 S (16.7%) and 13.4 S (5.5%) species that closely match the predicted values for the monomer (5.8 S) and tetramer (13.6 S). Finally, there is a minor 3.6 S species (6.0%) in the c(s) distribution that likely corresponds to misfolded monomer. These results suggest that the RiDD may also undergo a concentration dependent association to form a dimer and a relatively unstable tetramer. The asymmetric unit we observe for the RiDD is a dimer, however, precedence in the literature for PFL

Enzyme activation and dehydratase assays. All GREs are activated by their corresponding activating enzyme (AE) in a S-adenosyl-L-methionine (SAM)-dependent manner[237]. The activation reaction is not trivial as all aspects of the procedure, including the glycyl radical itself, are sensitive to molecular oxygen. Previous work from this laboratory has demonstrated the SAM-dependent activation of the *Clostridium butyricum* glycerol dehydratase (CbGD) by the CbGD activating enzyme (CbGD-AE)[230,257], but the activation of the *Roseburia inulinivorans* diol dehydratase (RiDD) by the RiDD-AE has not been reported. The protein sequence of the RiDD-AE indicates that this activating enzyme contains only a single [4Fe-4S] cluster. Consistent with this observation and unlike what we observe for the CbGD-AE[257], iron analysis of the anaerobically expressed, purified, and reconstituted RiDD-AE used in this investigation revealed 3.73 $\pm$ 0.26 iron atoms per mole of protein. In this regard, the RiDD-AE is more similar to PFL-AE[245] in that both activating enzymes (PFL-AE and RiDD-AE) contain only the catalytic [4Fe-4S] cluster. In order to further address whether a [4Fe-4S] cluster was present in the RiDD-AE and functioned in the activation of the RiDD, we applied electron paramagnetic resonance (EPR) spectroscopy in order to probe the electronic environment of the [4Fe-4S] cluster.

The EPR spectrum of the purified RiDD-AE in the presence of 1.0 mM sodium dithionite is consistent with that of a reduced [4Fe-4S]$^{1+}$ cluster (Figure A.3, Panel A). Specifically, we observe a predominantly axial signal with $g_{||}$ of 2.016 and $g_{\perp}$ of 1.923 at 10 K. The addition of excess SAM to the purified RiDD-AE resulted in a shift in the signal to give a $g_{||}$ of 2.029 and $g_{\perp}$ of 1.863 at 10 K (Figure A.3, Panel B). These observations are typical of what has been extensively observed for the [4Fe-4S] cluster of other radical SAM AEs and has been recently reviewed elsewhere[237].

When the RiDD is added to the reduced RiDD-AE in the presence of SAM, the Fe-S cluster signal is lost and a radical signal, centered at g = 2.006, is observed. (Figure A.3, Panel C). All of the glycyl radicals that have been characterized to date are similarly centered at g = 2.00, but the precise centering varies from enzyme to enzyme. However, the lineshape and splitting is typically indicative of two-fold splitting due to the remaining proton on the glycine residue[241,245]. No substrate is present in these experiments and therefore the signal cannot be due to substrate or an intermediate species. However, sodium dithionite is a notoriously unstable reductant and we suspect that there is another radical species, most likely due to a non-physiological byproduct of dithionite oxidation, that is present in the sample at low concentrations relative to the glycyl radical. Additional results are described below that further address the signal we observed for the activiated RiDD. Specifically, side-by-side activation experiments were performed with the CbGD and a variant of the RiDD that support our conclusion that the majority of the signal is due to a protein-centered radical, most likely a radical on G817 of the RiDD. It is becoming increasingly apparent that it may be important to utilize the physiological electron donor when studying radical SAM enzymes[114]. Regardless, we do not observe any dehydration activity if this signal is not observed for the RiDD.

The complete loss of the [4Fe-4S] signal was somewhat surprising, however, spin integration of this signal against a Cu-EDTA standard indicated that sodium dithionite is

incapable of fully reducing this cluster. Specifically, while iron analysis indicates that each monomer of the RiDD-AE contains an intact [4Fe-4S] cluster, spin integration against a Cu-EDTA standard results in 0.3 spins per monomer of RiDD. This confirms that less than 30% of the [4Fe-4S] clusters are in the reduced, or 1+, oxidation state. This also explains the complete loss of the EPR signal for the cluster at 10 K, after SAM is added and the glycyl radical has been generated, as all of the spin density has been converted to the radical signal. In this initial investigation we employed the chemical electron source, sodium dithionite, in order to reduce the [4Fe-4S] cluster of the RiDD-AE. Given the difficultly working with these enzymes and the observation that the physiological electron donor is important for complete reduction of the [4Fe-4S] cluster in another radical SAM enzyme[114] future efforts will be made to isolate the physiological donor(s) from *R. inulinivorans* and optimize reduction of the catalytic cluster.

"Pre-activation" of the RiDD. Given the observations above, it was important to establish a linear range for RiDD turnover using the partially activated enzyme, prior to investigating the dehydration of 1,2-propanediol. Various concentrations of pre-activated RiDD were investigated using a previously reported coupled assay[230] with a small modification. Specifically, we pre-activated a batch of RiDD prior to adding known amounts of this activated RiDD to the dehydration assay. The decrease in the absorbance at 340 nm (Figure A.4) is due to the NADH-dependent reduction of propanal to propanol by the coupling enzyme, yeast alcohol dehydrogenase (YADH). Based on the rate of NADH consumption by the coupling enzyme at the various RiDD concentrations investigated (Figure A.4, inset), the average specific activity under these experimental conditions is calculated to be 5.5 $\pm$ 0.4 µmoles min^{-1} mg^{-1}. If the RiDD is not pre-activated, then a significant lag time is observed before the production of propanal, and subsequent NADH-dependent reduction to propanol by YADH, is observed (data not shown). However, the specific activity calculated from the maximum slope observed at the highest concentrations of

substrate (S)-1,2-propanediol is very similar to what was observed for the pre-activated enzyme (approximately 5.0 compared with 5.5 μmoles min^{-1} mg^{-1}). Notably, increasing the 1,2-propanediol concentration results in a decrease in the lag time required to achieve maximum turnover, suggesting a faster activation rate in the presence of substrate, a proposal that is consistent with recent observations for PFL[246]. Moreover, as shown in Figure A.5, the RiDD catalyzes the dehydration of (S)-1,2-propanediol considerably faster than (R)-1,2-propanediol. However, due to the degree of error and technical challenges associated with these experiments it is impossible to determine a reliable Km for the two substrates at this time. In addition, as we demonstrate below, there may be additional factors that complicate the kinetic analysis. Regardless of the significant technical challenges, what can be unequivocally gained from these data is that the RiDD is in fact a 1,2-propanediol dehydratase with a preference for the ”S” enantiomer.

Direct detection of dehydration products by gas chromatography. Gas chromatography (GC) was also employed to look directly at the products of the RiDD-catalyzed dehydration reaction. As previously reported, it was possible to obtain good separation of the compounds 1,2-propanediol, acetone, and propionaldehyde[258]. It is important to note that this experiment is performed on a significantly larger scale and at a much higher concentration of 1,2-propanediol (5% v/v). No coupling enzyme was included, thus, allowing the products of the dehydration reaction to accumulate. Samples were analyzed by GC/FID analysis to directly quantitate the production of propanal. In particular, when glycerol was used as a substrate for the RiDD, no activity was observed when up to 8 mM glycerol was tried as the substrate. Surprisingly, when 1,2-propanediol was the substrate we observed acetone production in addition to propanal production with both enantiomers of 1,2-propanediol (Figure A.6). An explanation for acetone production is not immediately apparent, however, these observations further confirm that the RiDD is in fact selective for 1,2-propanediol. These data may have mechanistic implications as we do not observe any

acetone production when 1,2-propanediol is the substrate for the CbGD.

Active site structure of the RiDD compared to the CbGD. The active site structure of the RiDD may provide an explanation for the functional observations described above. Figure A.7 shows the models for the RiDD determined in this work. Ethanediol, presumably a contaminant of the low molecular weight PEG we used to crystalize the RiDD, is observed in the active site of crystals obstained for the ”as-isolated” enzyme (Figure A.7, Panel A). Fortunately, it was possible to transfer these crystals, in a stepwise fashion, to mother liquor containing 5% 1,2-propanediol (racemic mixture). The diffraction quality did decreased to 2.4 Å (Table A.1), but the 1,2-propanediol was clearly observed in the active site (Figure A.7, Panel B). Refinement with either enantiomer, visual inspection for any difference density and slightly lower R-values indicates that (S)-1,2-propanediol is bound and therefore has been modeled as such. Notably, the hydroxyl groups of the ethanediol and 1,2-propandiol are similarly positioned in the active site of the RiDD models (Compare Panel A with Panel B in Figure A.7). The binding mode of the ethanediol further supports modeling (S)-1,2-propanediol in the active site as alignment of the backbone carbon atoms of the ”R” enantiomer for 1,2-propanediol would cause a steric clash with the side chain of F344. Furthermore, when the 1,2-propanediol-bound RiDD model is aligned with the glycerol-bound model of the CbGD, both substrates are in similar positions within the active site (Figure A.8). However, there is a very distinct difference between the active site structure of the RiDD and the CbGD. Specifically, amino acids Y339 and S642 are within hydrogen bonding distance of each other and S642 is also within hydrogen bonding distance of the third hydroxyl group of glycerol. The equivalent residues in the RiDD are F344 and V696. In fact, based on the alignment shown in Figure A.8, the side chain of V696 occupies the space that would be required to accommodate glycerol.

Site-directed mutagenesis of the RiDD and glycerol dehydration. In order to test the hypothesis that residues F344 and V696 are responsible for the preventing glycerol

binding and turnover in the wild-type RiDD, we constructed the F344Y/V696S RiDD. This variant was also useful in re-examining the radical signal we observe for the wild-type RiDD. Specifically, before performing a coupled assay using glycerol as the substrate, we first investigated the SAM-dependent activation of the F344Y/V696S RiDD by the RiDD-AE in a side-by-side activation experiment with the wild-type CbGD. These data are shown in Figure 9. Similar to what we observed for the wild-type RiDD, the center of the EPR signal we observe for the activated F344Y/V696S RiDD is somewhat shifted by comparison to the radical signal observed for the CbGD. Both the wild-type RiDD and F344Y/V696S RiDD are weaker than the radical signal observed for the activated CbGD, consistent with the partial reduction we observe for the dithionite-treated RiDD-AE. Interestingly, the lineshape for the activated F344Y/V696S RiDD is more similar to what we observe for the CbGD. In the absence of access to the physiological reduction partners for the RiDD-AE, we are hesitant to read too much into these observations and recognize that one explanation for the unusual shift and lineshape of the EPR signal we observe for the activated RiDD may simply be due to radicals associated with byproducts of the chemical reductant used. Regardless, in all cases, we do not observe any dehydration activity for any of these enzymes unless the respective EPR species are generated first.

Given that the F344Y/V696S RiDD could be activated, as judged by the EPR data above, we asked whether or not the enzyme could dehydrate glycerol. We did in fact observe NADH consumption in a coupled assay when glycerol is the substrate for either the CbGD or the F344Y/V696S RiDD variant (Figure A.10). However, the specific activity for glycerol dehydration by the F344Y/V696S RiDD variant is considerable less than what is observed for the CbGD. The F344Y/V696S RiDD did purify with slightly lower yields suggesting it might be less stable than the wild-type enzyme, but nonetheless this variant catalyzed glycerol dehydration at maximum rate of 0.81 $\pm$ 0.02 μmoles min^{-1} mg^{-1}. Although this rate is almost 5-fold slower when compared to the CbGD, these observations

suggest that these two amino acids do in fact play a role in the substrate selectivity. The slower rate of activity suggests that the conformational dynamics of the active site and dehydration mechanism are considerably more complex.

Discussion

The functional diversity of glycyl radical enzymes is impressive[236,259,260] and has important implications for many aspects of human health and general quality of life. For example, the inhibition of some of these reactions will prevent anaerobic growth by certain pathogenic microorganisms[261]. In addition, many of the reactions are industrially significant, making GREs of interest as potential biocatalysts. However, there are a number of unanswered questions regarding the activation, mechanism, and deactivation of GREs that remain to be addressed.

Overall structure and the C-terminal glycyl radical domain. The RiDD model exhibits the anticipated 10-α/β-barrel fold and aligns best with the structure reported for the CbGD. The enzyme exists predominantly as a dimer in solution. The presence of some tetrameric species in solution was unexpected and potentially interesting in light of the observation of two additional protein-protein interfaces with significant buried surface area in the unit cell of the RiDD crystals. One of these interfaces is facilitated by an additional stretch of amino acids although the function of relevance of this domain and interaction is unclear. However, all of the available GRE structures, the conserved glycyl radical domain is found in the C-terminal domain of the 10-α/β-barrel fold. Significant conformational changes are required in order to move the loop containing the glycyl radical out of the core of the GRE and into the active site of the activating enzyme. In addition to demonstrating a dimer in solution, recent work with CutC has provided evidence that the substrate may help induce some of the conformational changes required for activation[242]. Considering the structures of all GREs, and based on the alignment of backbone atoms, the overall fold of

the RiDD is also more similar to the large subunits of benzyl succinate synthase (BSS) and 4-hydroxyphenyl acetate decarboxylase (4-HPAD)[249,262], consistent with what has been reported for the CbGD. Although both BSS and 4-HPAD have additional peptide subunits, the C-terminal gly radical domain of all GREs must undergo extensive conformational changes in order to present the glycyl radical loop to the active site of the respective activating enzyme[247]. Funk *et al.* noticed that contacts between the C-terminal gly radical domain and "loop 2" of the N-terminal domain in the CbGD resulted in burying approximately an additional 100 Å[247]. They speculated that loop two would have to move in order to facilitate the opening of the gly radical domain. We observe a similar interaction in the RiDD structures reported here, however, we do see a subtle difference in the positioning of loop 2 when the RiDD structures are aligned with the CbGD model. Specifically, with the exception of backbone residues 106 to 109 in the RiDD, the N-terminal and C-terminal gly radical domain align with an RMSD of less than 0.5 Å. Interestingly, the backbone alpha carbon atoms of residues 106-109 are 2-3 Å away from the equivalent atoms in the CbGD model. This observation provides additional support for the hypothesis put forth by Funk *et al.* regarding the activation of the CbGD. This interaction is not present in the structural models of pyruvate formate-lyase (PFL). However, PFL remains somewhat unique in that it has also been shown to exhibit "half-sites" reactivity[244,245,263] and appears to have a "repair peptide", YfiD, that can be post-translationally activated by PFL-AE. The activated YfiD can replace any glycyl radical domains in PFL that have been oxygen damaged[264].

Generation of the glycyl radical. At the present time, there is no evidence to suggest there is any allosteric communication between active sites in the physiological dimer that we observed for the RiDD. In addition, there is no evidence that the glycyl radical must be generated at both active sites in order to observe activity in any GRE. However, one common feature that all of the GREs have been shown (or predicted) to contain is a catalytic dyad consisting of a conserved glycine and cysteine residue. The thiol group

of the conserved cysteine is positioned close to the alpha carbon atom of the glycine residue (typically within 3.5 Å). The location and position of the catalytic dyad facilitates radical transfer from the alpha carbon atom of the glycine residue to the sulfur atom of the cysteine residue via hydrogen atom abstraction. The latter radical is positioned to abstract a hydrogen atom from the primary metabolic substrate. For the RiDD reported here, the sulfur atom of C438 is within 3.6 Åof the C1 carbon atom of 1,2-propanediol (Figure 7, Panel B). At the present time, we have not identified or isolated the physiological electron donor for the RiDD-AE and therefore we are hesitant to speculate on the precise identity of the radical signals we observe for the wild-type and F344Y/V696S variant of the RiDD at 70 K. However, chemical reductants can lead to artifacts and the importance of the electron source for radical SAM enzymes has been clearly highlighted in recent work[114]. The significant point is that we do not observe any dehydration activity for the RiDD unless these radical species are generated. Interestingly, the lineshape of the EPR spectra we observe for the activated F344Y/V696S variant looks more similar to the radical signal we observe for the activated CbGD, suggesting that these amino acids may have some influence on the generation and environment of the glycyl radical in the RiDD. Future work will absolutely require the identification and isolation of the physiological electron donor to the RiDD-AE in *R. inulinivorans*.

Mechanism of GRE-dependent dehydration. At least two mechanisms have been proposed for the dehydration of glycerol as catalyzed by the CbGD[230,256]. Both mechanisms are also relevant to 1,2-propanediol dehydration and both begin with the radical on the catalytic cysteine residue (C433 or C438 in the CbGD or RiDD, respectively). This radical is positioned to abstract a hydrogen atom from substrate (either 1,2-propanediol or glycerol). The former mechanism, proposed by O'Brien *et al.*, involves abstraction of the pro-*S* hydrogen atom from the primary carbon atom followed by the migration of the new substrate radical and hydroxyl group in opposite directions. The substrate/intermediate radical re-

abstracts a hydrogen atom from the catalytic cysteine to produce a hydrated aldehyde that spontaneously decomposes to water and 3-hydroxy propionaldehyde. In the O'Brien proposal the migrating hydroxyl is stabilized by a pair of conserved, and appropriately protonated, histidine side chains (H164 H281 of the CbGD). In a purely computational investigation, Feliks et al. proposed that these histidine residues, H164 in particular, could facilitate the direct donation of a proton and loss of water. In such a "direct dehydration" mechanism, only the substrate/intermediate radical migrates from the primary to secondary carbon atom of glycerol before re-abstracting a hydrogen atom from C433 and resetting the enzyme for another round of turnover.

Prior to this work, there was no evidence to suggest that the mechanism of glycerol dehydration would be significantly different from 1,2-propanediol dehydration in the GRE-dependent dehydratases. In fact, as both mechanisms for the CbGD predicted, it was reasonable to predict that a proton on the C1 carbon atom of 1,2-propanediol would be abstracted first in the mechanism of the RiDD. However, the production of some acetone with either enantiomer of 1,2-propanediol by the RiDD calls this proposal into question. Although both the RiDD and the CbGD prefer the "S" enantiomer of 1,2-propanediol the CbGD will not utilize the "R" enantiomer at all and does not produce any acetone. This suggests that the two dehydratases have subtly different molecular dynamics. In particular, the RiDD may be a "sloppy" enzyme by comparison to the CbGD with a slightly more flexible active site. In theory, the F344Y/V696S RiDD should have identical interactions with glycerol and catalytic activity when compared to the CbGD or wild type RiDD, clearly this is not the case. In this light, acetone production by the RiDD may simply reflect this flexibility and may be the result of some misoriented substrate leading to hydrogen atom abstraction from the C2 atom of 1,2-propanediol and direct removal of the hydroxyl group on the C1 carbon atom of 1,2-propanediol.

Taken together, these data also indicate that both dehydration mechanisms (direct

dehydration versus hydroxyl/radical co-migration) may be valid, depending on the dynamics of the active site and precisely how the substrate is positioned. In fact, multiple binding modes for have been proposed to explain the mechanism-based inactivation by glycerol that has been observed for the B_{12}-dependent diol dehydratase[265]. Specifically, although glycerol is not a chiral compound, glycerol can bind to the active site of the B_{12}-dependent diol dehydratase in two different orientations. One orientation mimics the geometry and binding mode of S-1,2-propanediol (G_S), while the other binding mode is similar to that of R-1,2-propanediol (G_R). Because of the different geometry, the hydrogen bond strength varies between the G_S or G_R orientation. The starting orientation is important because during the dehydration reaction, and specifically the migration of the middle hydroxyl group of glycerol, there is an energetic penalty associated with stronger hydrogen bonding of the G_S orientation. Hence, it was proposed that undesirable side reactions leading to the suicide inhibition of the B_{12}-dependent diol dehydratase occur with a much higher probability for glycerol that is bound in the G_S orientation[265]. Consistent with this proposal, the B_{12}-dependent diol dehydratase will utilize both enantiomers of 1,2-propanediol but has a preference for the "R" isomer[266]. Interestingly, the results reported here are consistent with the CbGD having a more selective binding site with glycerol or S-1,2-propanediol bound in a single orientation, while the RiDD, has slightly more conformational flexibility.

Conclusions. The catalytic power of GREs is significant interest, especially in light of anaerobic metabolism in the intestinal microbiome[242,248,250] and growing demand for biocatalysts capable of performing difficult chemical rearrangements. While B_{12}-dependent glycerol and diol dehydratases have been well studied, this is the first report of a GRE- or B_{12}-independent diol dehydratase. Intestingly, a similar parallel is observed when comparing the GRE-dependent glycerol dehydratase, CbGD, with the GRE-dependent diol dehydratase, RiDD. Specifically, similar to what has been reported for the B_{12}-dependent enzymes, the diol dehydratase may be more susceptible to re-engineering[265]. In order

to address this thoroughly, as well as the mechanism of all GREs, it will be imperative to utilize the physiological donors (i.e. flavodoxin or ferredoxin) when providing reducing equivalents for the activating enzymes.

Tables and Figures

Table A.1: Data collection and refinement statistics for RiDD

	RiDD	
	ethanediol	**S-1,2-propanediol**
PDB ID code	5I2A	5I2G
Space Group	$C222_1$	$C2_1$
Wavelength	0.98	0.98
Resolution Range (Å)	50.0-2.1	50.0-2.4
Outer Shell	2.18-2.1	2.45-2.4
Unique Observations	166,139	74,266
Completeness (%)	98.9(90.3)[a]	98.8(88.9)
R_{merge} (%)[b]	0.06(0.29)	0.12(0.33)
Redundancy	6.9(3.4)	7.2(3.5)
I/σ	22.2(2.8)	22.1(4.9)
Unit Cell Dimensions (Å)	a = 138.2, b = 183.2, c = 228.3	a = 204.3, b = 83.2, c = 138.2
Protein Atoms	3087	
Solvent Atoms	306	
Resolution Limits (Å)	50.0-2.0	
R_{cryst} (%)	15.2	14.5
R_{free} (%)	19.0	20.3
rmsd bonds (Å)	0.007	0.008
rmsd angles (°)	1.01	1.04
average B factor (Å^2)	30.2	34.6

[a] Numbers in parentheses denote values for the outermost resolution shell.
[b] $R_{sym} = \sum hkl[\sum I(|I_{hkl,I} - < I_{hkl} >|)]/\sum hkl, I<\mathrm{I}_{hkl}>$, where I_{hkl} is the intensity of an individual measurement of the reflection with indeces hkl and $<\mathrm{I}_{hkl}>$ is the mean intensity of that reflection.

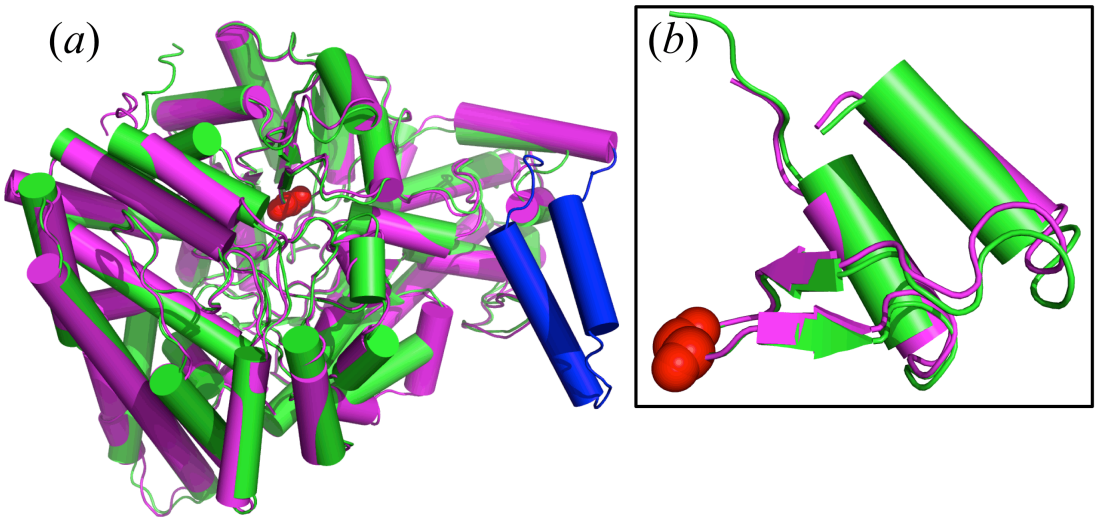

Figure A.1: Cartoon representation of the RiDD model aligned on the CbGD model *(Panel A)* and a structural alignment of the C-terminal domain for both models *(Panel B)*. The CbGD model is colored green and the RiDD model is colored magenta, with the exception of a 48-amino acid insert that is colored blue. The conserved glycine residue in both structures is represented by red space-filling atoms in Panel B.

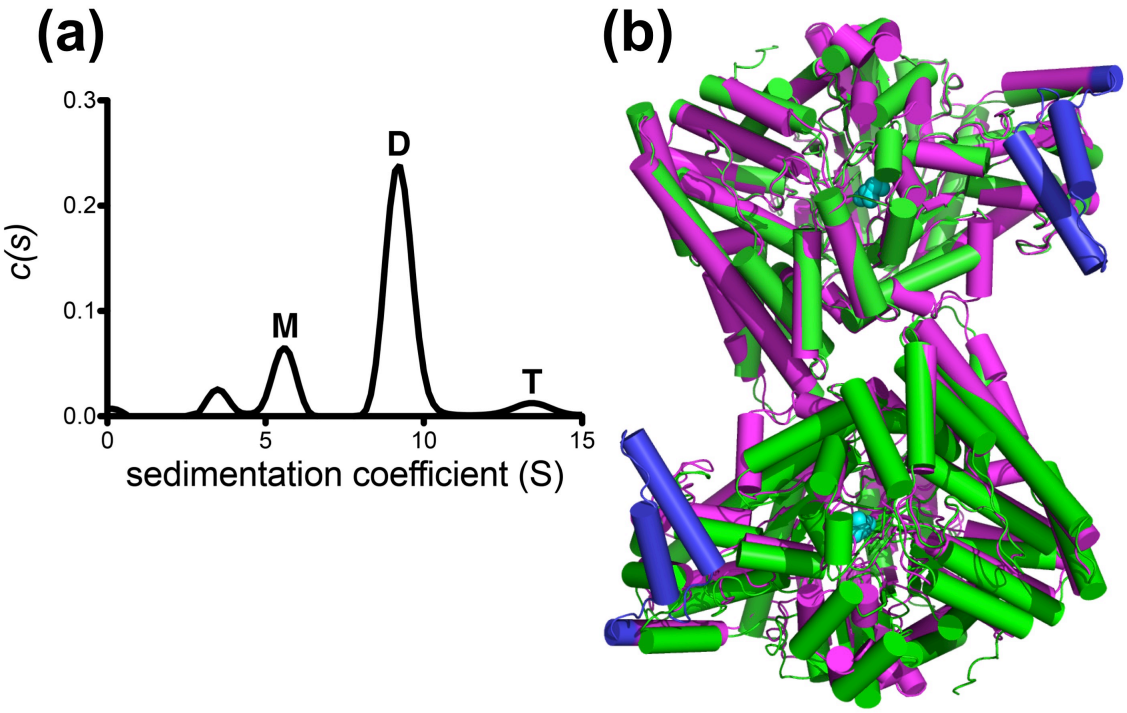

Figure A.2: Sedimentation velocity study for the RiDD *(Panel A)* and a cartoon representation *(Panel B)* of the proposed RiDD dimer overlayed on top of the asymmetric unit observed for the model of the CbGD (PDB ID 1R9D). The c(s) sedimentation distribution reveals species corresponding to monomer (M, 5.6 S), dimer (D, 9.2 S) and tetramer (T, 13.4 S). The peak at 3.6 S likely represents a small amount of misfolded monomer. The color scheme for the cartoon representation of the RiDD and CbGD models is the same as shown in Figure A.1 except that the atoms of the conserved glycine in the RiDD model are highlighted as cyan space-filling spheres.

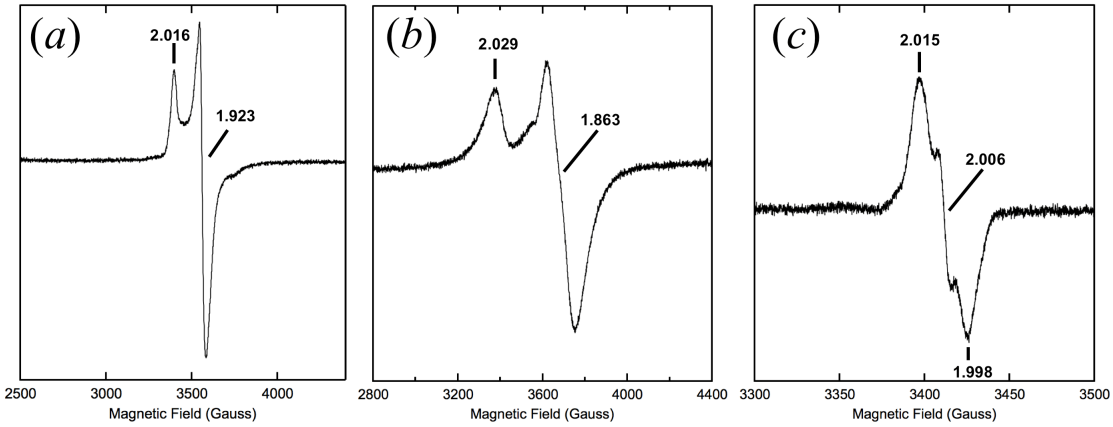

Figure A.3: EPR spectra monitoring the SAM-dependent generation of a catalytic radical on the RiDD by the RiDD-AE. EPR spectra of 0.1 mM RiDD-AE alone *(Panel A)*, in the presence of 1.25 mM SAM *(Panel B)*, and following the addition of an equimolar amount of the RiDD *(Panel C)*. The spectra presented in Panel A and Panel B were recorded at 10 K with a microwave power of 0.25 mW, while the data presented in Panel C was recorded at 70 K with a microwave power of 0.05 mW. All of the spectra represent the sum of three scans and were recorded with a microwave frequency of 9.582 GHz, a modulation amplitude of 6.477 G, and the modulation frequency was 100 kHz.

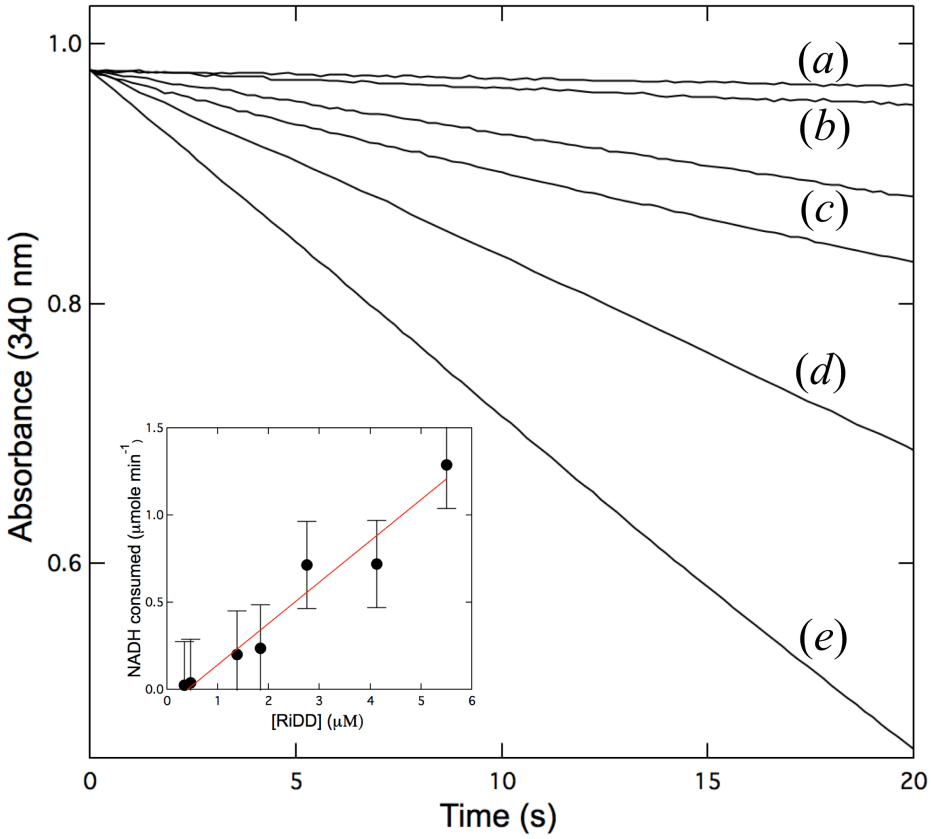

Figure A.4: Monitoring RiDD activity using pre-activated enzyme. The RiDD was pre-activated as described in the Materials and Methods and then added to a coupled assay where the NADH-dependent reduction of propanal by YADH (1 mg/mL) was monitored in real time at 340 nm using the extinction coefficient of 6220 M^{-1} cm^{-1} in order to follow the change in NADH concentration. Raw data for assays that were performed with (a) 0, (b) 0.3 μM, (c) 0.5 μM, (d) 1.4 μM, (e) 2.7 μM, and 5.5 μM concentrations of the RiDD. The inset shows a plot of the rate of NADH consumption versus the concentration of RiDD (molecular weight approximately 94 kDa) for multiple experiments. Assays were performed in triplicate and error bars represent the standard deviation across the data set.

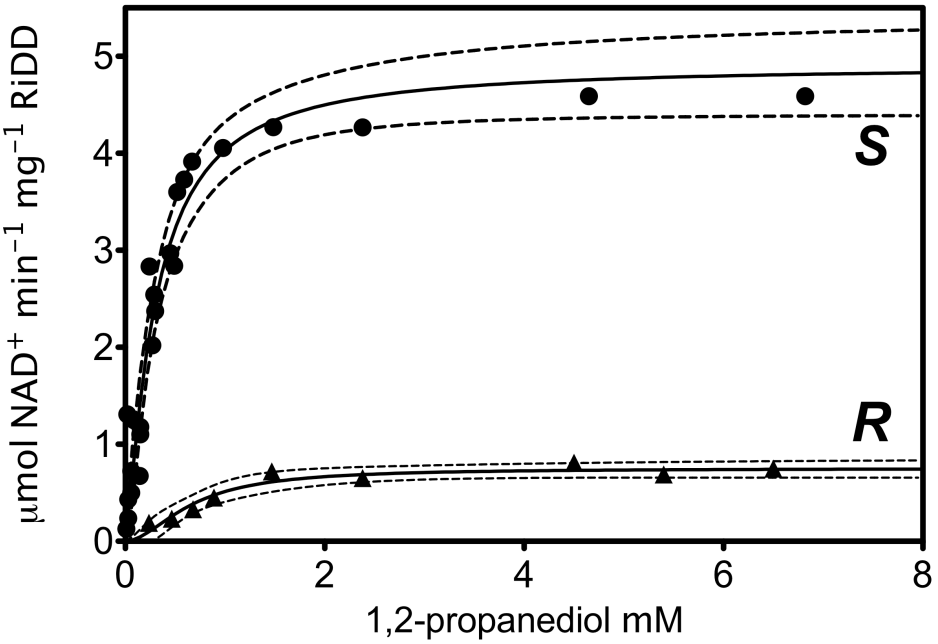

Figure A.5: Substrate saturation plot showing the specific activity, calculated from the maximum rates of NADH consumption in the coupled assay, that were observed for the RiDD at different concentrations of (S)-1,2-propanediol (Trace ”S”) or (R)-1,2-propanediol (Trace ”R”). Data points represent the average value for three experiments and were fit to the Hill equation with a 95% confidence range displayed by the dotted lines.

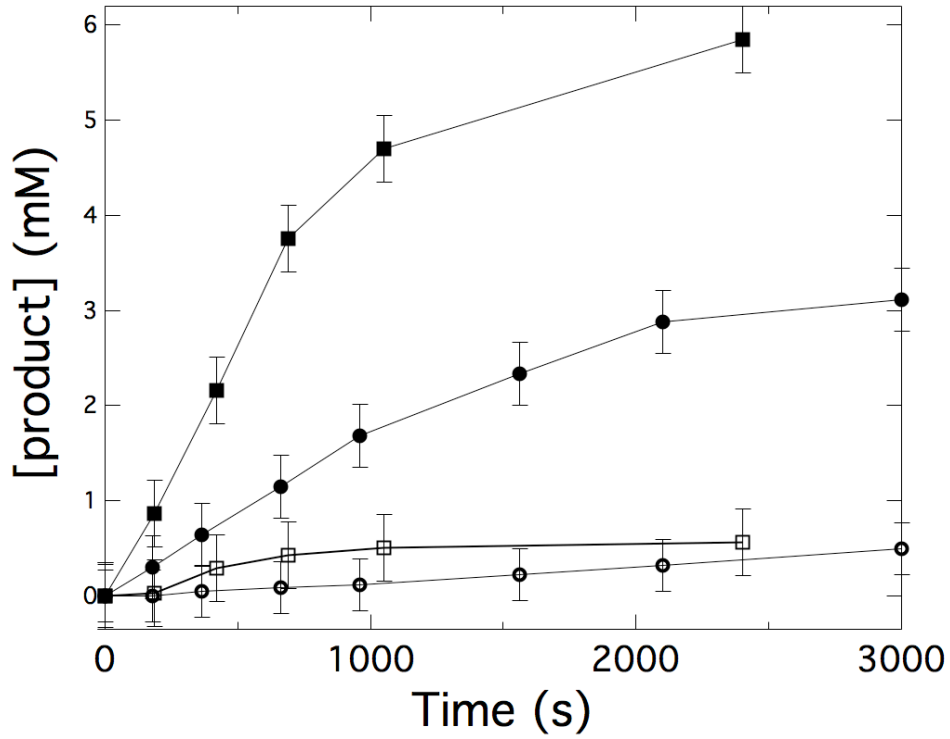

Figure A.6: Gas chromatography (GC) data following the conversion of 1,2-propanediol to propionaldehyde and acetone by the RiDD. Assays were performed and samples for GC analysis were prepared as described in the Materials and Methods. Samples were taken and analyzed at the indicted time points. The data show the amount of propionaldehyde (■) and acetone (□) produced when S-1,2-propanediol was used as substrate as well as the propionaldehyde produced (●) and acetone (○) produced when R-1,2-propanediol was used as the substrate for the RiDD in the assay. All experiments were performed in triplicate and the error bars represent the standard deviation across all data points for a given data set.

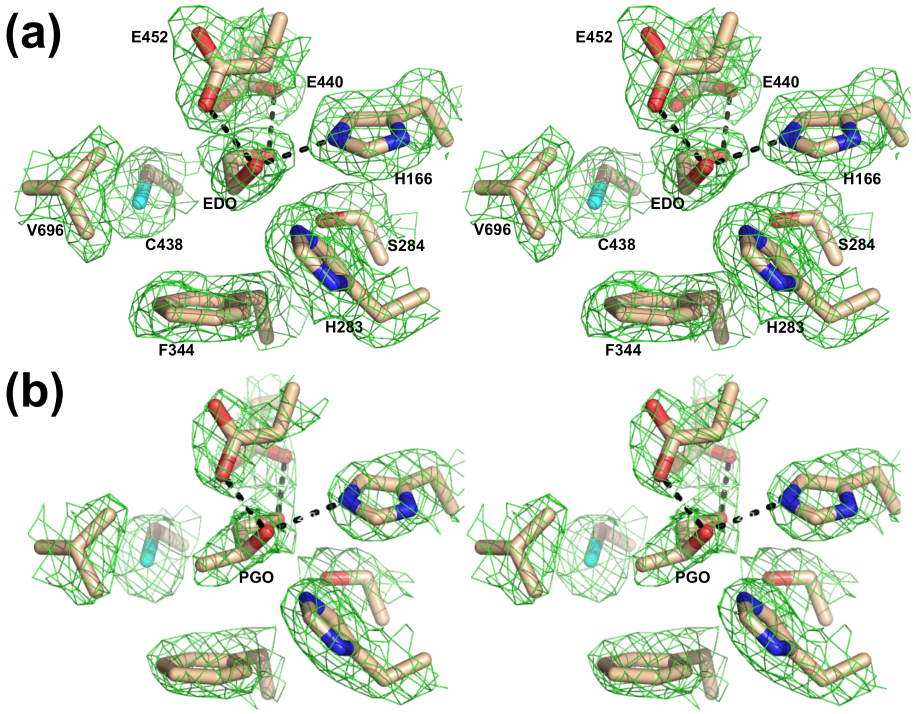

Figure A.7: Wall-eyed stereoview showing a stick representation of the active site model determined for the *R. inulinivorans* diol dehydratase (RiDD) with ethanediol *(Panel A)* or S-1,2-propanediol bound (Panel B). In both cases, the 2Fo-Fc composite omit map (Green cage) was generated using the simulated annealing protocol with 7% of the model omitted per cycle. The electron density is contoured at 1.3 σ and the carbon, oxygen, nitrogen, and sulfur atoms are colored tan, red, blue, and cyan, respectively. Ethanediol and S-1,2-propanediol are labeled EDO and PGO respectively. The dashed lines highlight atoms within hydrogen bonding distance of the hydroxyl groups of ethanediol *(Panel A)* or propanediol *(Panel B)*.

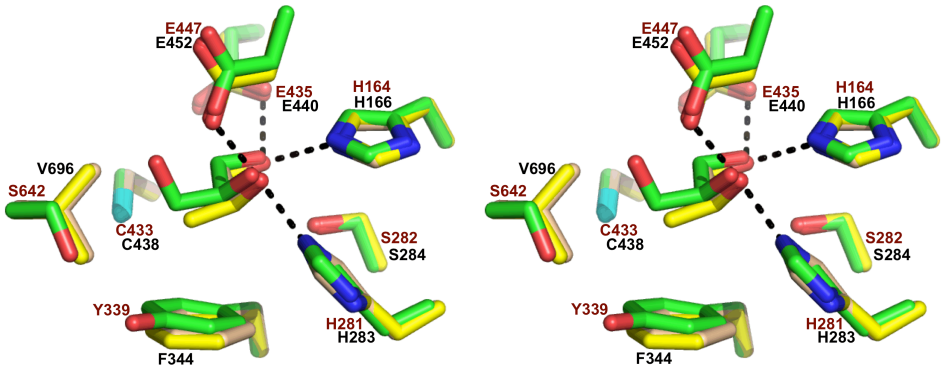

Figure A.8: Wall-eyed stereo view of a cartoon diagram showing an overlay of the RiDD model with ethanediol bound (this work, tan carbon atoms), the RiDD model with S-1,2-propanediol bound (this work, yellow carbon atoms) and the CbGD model with glycerol bound (green carbon atoms). The amino acid residues for the RiDD and CbGD models are labeled in black and brown text, respectively. The dashed lines indicate atoms that are within 3.7 Å of one another.

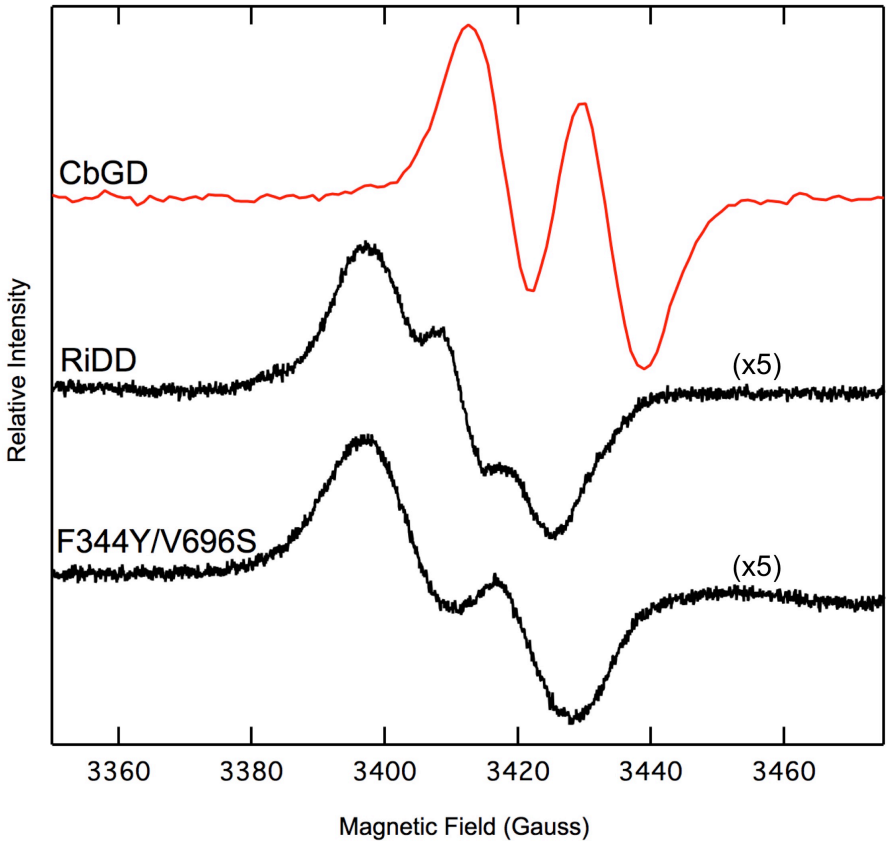

Figure A.9: EPR spectra recorded at 70 K for the activated CbGD, RiDD, and the RiDD double mutant F344Y/V696S. All of the spectra represent the sum of three scans and were recorded with a microwave power of 0.05 mW, microwave frequency of 9.582 GHz, modulation amplitude of 6.477 G, and a modulation frequency of 100 kHz. The intensity of the RiDD and the F344Y/V696S variant were considerably less that what was observed for the CbGD and have been increased five fold for a better comparison.

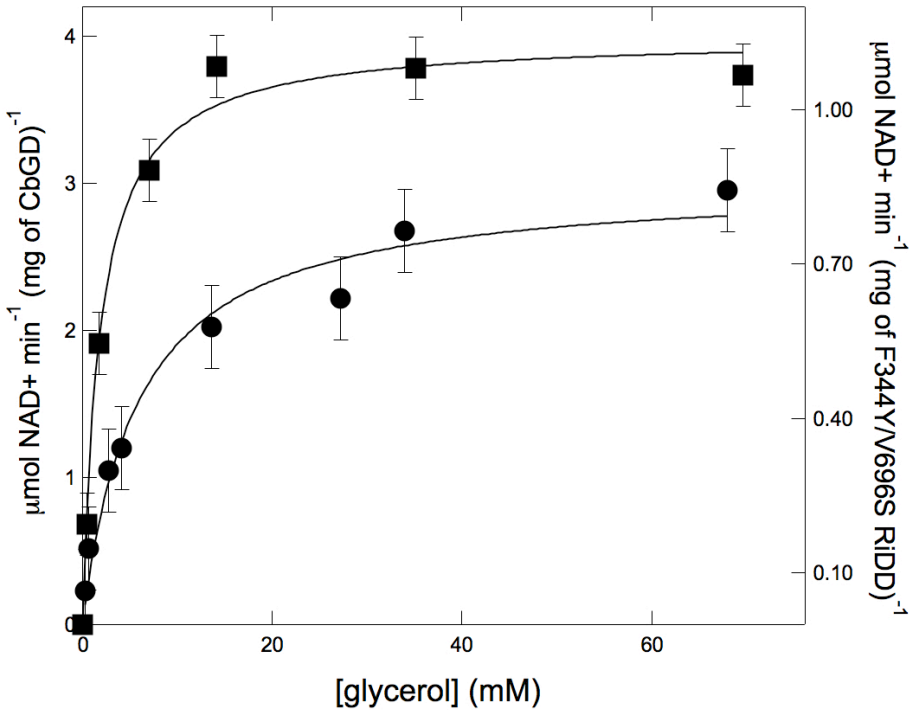

Figure A.10: Substrate saturation plot showing the specific activity, calculated from the maximum rates of NADH consumption in the coupled assay, for the CbGD (left axis) and the F344Y/V696S variant of the RiDD (right axis) when glycerol was used as the substrate. The coupled assay was performed as described in the Experimental Procedures with the notable exception that purified DhaT was used as the coupling enzyme instead of YADH. Experiments were performed in triplicate and error bars represent the standard deviation across all data points.

Materials and Methods

Enzyme expression, purification and crystallization. Unless explicitly stated, all experimental procedures were carried out under strictly anaerobic conditions and all solutions were made anaerobic by purging with oxygen-free argon on a vacuum manifold. In addition, all sample preparation for spectroscopic studies or enzyme assays was carried out in a Coy anaerobic chamber containing an atmosphere of 5% hydrogen with the balance being nitrogen and less than 1 ppm oxygen. The genes for the *Roseburia inulinivorans* diol dehydratase (RiDD), the RiDD activating enzyme (RiDD-AE), and the 3-hydroxyprionaldehyde (3-HPA) reductase (DhaT, a.k.a. 1,3-propanediol dehydrogenase) from *C. butyricum* (NCBI accession 's WP_007885173, ABC25540, and AAM54730.1 respectively) were all codon-optimized for expression in *E. coli* and cloned into the commercially available pTRCHis vector introducing a 6x polyhistidine tail at the N-terminus (specifically MSHHHHHHSGS) prior to the first amino acid of the native sequence. The diol dehydratase from *Roseburia inulinivorans* (RiDD), the RiDD activating enzyme (RiDD-AE), and DhaT were purified using the same affinity column procedures reported for the *C. butyricum* glycerol dehydratase (CbGD) and *C. butyricum* glycerol dehydratase activating enzyme (CbGD-AE)[230]. Briefly, this involves affinity purification using the cobalt-loaded Talon affinity resin followed by gel filtration using an S-200 column equilibrated with 50 mM TRIS pH 8.0 and 500 mM KCl. Identical buffer was used to further purify the RiDD using gel filtration Superdex S-200 resin (GE Healthcare Life Sciences). In the case of the RiDD-AE, a chemical reconstitution of the [4Fe-4S] cluster was performed as previously described[267] and the enzyme was subjected to further purification using anion exchange chromatography. Specifically, sodium sulfide (0.2 mM), 2-mercapoethanol (5 mM), and ferrous ammonium sulfate (0.25 mM) were added to the solution and the entire mix was gentle stirred overnight at 4 ℃. Precipitate was removed by centrifugation and the supernatant was loaded onto a 5 mL Sepharose QFF

column. The protein was then eluted from the column by applying a linear salt gradient (from 0 to 0.5 M KCl) in 20 mM TRIS pH 8.1. Elution typically occurred around 150 mM KCl. Essentially, the reconstituted activating enzymes were subjected to anion exchange chromatography in order to remove adventitiously bound iron and sulfide. The RiDD-AE was concentrated and stored in liquid nitrogen. Protein concentrations were determined using the modified Biuret method[268] and all proteins were judged homogeneous by SDS-PAGE analysis.

EPR spectroscopy. Electron paramagnetic resonance (EPR) was employed in order to monitor SAM-dependent changes in the spectrum of the [4Fe-4S]$^{1+}$ cluster in the RiDD-AE as well as the SAM-dependent generation of a catalytic radical on the RiDD. All EPR samples contained 1 mM sodium dithionite and were recorded using a microwave frequency of 9.602 GHz, modulation amplitude of 6.3 G, and a modulation frequency of 100 kHz as previously described[230]. The concentrations of enzyme or SAM added were as noted in the figure legend. Spectra were recorded at 10 K as well as 70 K for all samples unless stated otherwise.

Coupled enzyme assay for the CbGD and RiDD. The coupled enzyme assay for the CbGD and the RiDD were performed an anaerobic quartz cuvettes essentially as previously described[230] at 25 °C, except that, where indicated, the RiDD was ”pre-activated” prior to addition of the substrate as described below. Similar assays utilizing a coupling enzyme have been used before by those studying the B_{12}-dependent glycerol and diol dehydratases[269]. Essentially, an aldehyde reductase, that utilizes NADH or NADPH to reduce the aldehyde to the corresponding alcohol, is often used as a coupling enzyme. Depending on the specific dehydration reaction being investigated, several coupling enzymes have already been well characterized (16,25-29). Unless stated otherwise, the assay contained 1 mM SAM, 1 mM sodium dithionite, 100 mM KCl and 200 µM NADH in 50 mM HEPES pH 7.5. The assay also contained 28 µM of yeast alcohol dehydrogenase (YADH). The

total volume of the coupled assay was 0.5 mL and the substrate as well as the enzymes (RiDD and RiDD-AE) were all added to the concentrations indicated in the appropriate figures. Prior to initiating the assay the spectrophotometer was blanked against assay buffer. In order to ”pre-activate” the RiDD, this enzyme was incubated with the RiDD-AE (2:1 RiDD-AE:RiDD) in the presence of 2 mM SAM and 2 mM sodium dithionite for 10 minutes in order to allow for generation of the glycyl radical, a variety of enzyme concentrations were tried in these experiments and the assay was initiated by addition of the substrate. In general, the coupled assays takes advantage of a catalytic excess of the reductase YADH in order to rapidly reduce the propionaldehyde product of the dehydratase reaction. We independently investigated the specific activity of commercially available YADH (Sigma Chemical Company) by measuring the NADH-dependent reduction of propionaldehyde in the assay buffer described above and found that it was greater than 400 µmol min^{-1} mg^{-1}. In order to address glycerol dehydration by the CbGD and the F344Y/V696S variant of the RiDD, the YADH was replaced with purified DhaT in the coupled assay.

Direct monitoring of 1,2-propanediol dehydration by gas chromatography (GC). The direct detection of 1,2-propanediol, propionaldehyde, and acetone was performed using a gas chromatograph (GC) equipped with a 30 m x 0.329 mm Carbowax 20m column. Due to the sensitivity of the GC/FID measurement and the sample collection protocol, the assay had to be performed at a much larger scale. Specifically, these assays were performed in 20 mL of assay solution with a concentration of RiDD of 1 µM. Yeast alcohol dehydrogenase as well as NADH, are omitted from this assay in order to allow to allow the propionaldehyde to accumulate. A stir bar was also included in the experiment and provided stirring at rate of approximately 75 rpm. In all these experiments the reaction was initiated by the addition of RiDD-AE to 2 µM in the presence of 2 mM SAM and 2 mM sodium dithionite. Propanediol (either S-1,2-propanediol or R-1,2-propanediol) was added 5% (v/v) at the beginning of the assay. At the time points indicated, 1 mL samples

were extracted anaerobically and immediately treated with 250 µL of 1M formic acid. The acid-treated samples were all centrifuged in a microfuge at 14,000 rpm for ten minutes in order to remove any precipitated material. The supernatant was then injected into the GC and separated using a temperature gradient that ramped from 60 ℃ to 120 ℃ over a 20 minute period. The GC was equipped with a flame ionization detector and a series of standards for 1,2-propanediol, acetone, and propionaldehyde were used to calibrate the integrated peak areas.

Crystallization, data collection, and structure determination. Initial crystallization conditions for the RiDD were identified in sitting drop experiments and then optimized in a hanging-drop tray. The final conditions for diffraction quality crystals of the RiDD were 0.125 M sodium acetate, 42 % PEG 400 (w/v), and 0.025 M HEPES pH 7.5. Crystallization was performed in hanging drop experiments with 800 µL of precipitating solution in the well. Protein (40 mg/mL) and precipitation solution were mixed (2 µL each) to initiate the reaction and then the tray was placed at 4 ℃ for 12 hours before being moved to an incubator at 18 ℃. Crystals of the RiDD took approximately one week to form and no further cryoprotection was required for freezing. Ethanediol was serendipitously observed in the active site of the RiDD for the native crystals, but it was possible to soak 1,2-propanediol (racemic mixture) into the crystals by simply transferring the crystals to mother liquor containing 5% 1,2-propanediol in a stepwise manner.

Data were collected at the Advanced Photon Source through SER-CAT on beam line 22BM at 0.98 Å. The program PHENIX[221] was used to solve the initial phase problem by using a poly-alanine model of the CbGD (PDB ID 1R9D) and molecular replacement. Iterative rounds of model building and refinement using COOT[222] and PHENIX were performed with experimental phase restraints and a 5.0% R_{free} test set[270] that was generated by PHENIX and used throughout all stages of model building and refinement. A summary of the data collection and refinement statistics for the ethanediol- and 1,2-propanediol-bound

models is shown in Table A.1.

Site-directed mutagenesis. The F344Y/V696S variant of the RiDD was generated using the QuickChange II kit (Agilent Technologies) by following the manufacturers instructions. Mutagenic oligonucleotides were synthesized by Integrated DNA Technologies (Coralville Iowa) and both mutations were verified by sequencing at the Georgia Genomics Facility.

Sedimentation velocity experiments. The RiDD was dialyzed into 10 mM HEPES (pH 7.5) and 150 mM KCL and then diluted to a final concentration of 5 µM for analysis. RiDD (400 µL) or reference buffer (410 µL) was loaded into 12 mm double-sector Epon centerpieces equipped with quartz windows, and equilibrated at 20 ℃ in an AN60 Ti rotor for 1 h. Sedimentation velocity data were collected in an Optima XLA analytical ultracentrifuge, using a rotor speed of 50,000 rpm at 20 ℃. Data were recorded at a wavelength of 280 nm using a radial step size of 0.003 cm. The partial specific volume of RiDD (0.73478 mL/g) was calculated from the amino acid sequence. The program SEDNTERP was used to calculate the density (1.00609 g/mL) and viscosity (0.01009 P) of the buffer[223]. SEDFIT was used to model and analyze the sedimentation data. Modeled data were fit as a continuous sedimentation coefficient c(s) distribution using the baseline, meniscus, frictional coefficient, systematic time-invariant noise and radial-invariant noise[271]. The root-mean-square deviation (rmsd) value for the experiment was less than 0.004 OD. Theoretical sedimentation coefficients (S) values were calculated from the atomic coordinates of RiDD using HYDROPRO[211].